Ministry of Education and Science of the Russian Federation
Saint Petersburg National Research University of Information
Technologies, Mechanics, and Optics

NANOSYSTEMS:

PHYSICS, CHEMISTRY, MATHEMATICS

2016, volume 7(4)

Наносистемы: физика, химия, математика

2016, том 7, № 4

NANOSYSTEMS:

PHYSICS, CHEMISTRY, MATHEMATICS

ADVISORY BOARD MEMBERS

Chairman: V.N. Vasiliev *(St. Petersburg, Russia)*,
V.M. Buznik *(Moscow, Russia)*; V.M. Ievlev *(Voronezh, Russia)*, P.S. Kop'ev*(St. Petersburg, Russia)*, N.F. Morozov *(St. Petersburg, Russia)*, V.N. Parmon *(Novosibirsk, Russia)*, A.I. Rusanov *(St. Petersburg, Russia)*,

EDITORIAL BOARD

Editor-in-Chief: I.Yu. Popov *(St. Petersburg, Russia)*

Section Co-Editors:
Physics – V.M. Uzdin *(St. Petersburg, Russia)*,
Chemistry, material science –V.V. Gusarov *(St. Petersburg, Russia)*,
Mathematics – I.Yu. Popov *(St. Petersburg, Russia)*.

Editorial Board Members:
V.M. Adamyan *(Odessa, Ukraine)*; O.V. Al'myasheva *(St. Petersburg, Russia)*; A.P. Alodjants *(Vladimir, Russia)*; S. Bechta *(Stockholm, Sweden)*; J. Behrndt *(Graz, Austria)*; M.B. Belonenko *(Volgograd, Russia)*; V.G. Bespalov *(St. Petersburg, Russia)*; J. Brasche *(Clausthal, Germany)*; A. Chatterjee (*Hyderabad, India)*; S.A. Chivilikhin *(St. Petersburg, Russia)*; A.V. Chizhov *(Dubna, Russia)*; A.N. Enyashin *(Ekaterinburg, Russia)*, P.P. Fedorov *(Moscow, Russia)*; E.A. Gudilin *(Moscow, Russia)*; V.K. Ivanov *(Moscow, Russia)*, H. Jónsson *(Reykjavik, Iceland)*; A.A. Kiselev *(Madison, USA)*; Yu.S. Kivshar *(Canberra, Australia)*; S.A. Kozlov *(St. Petersburg, Russia)*; P.A. Kurasov *(Stockholm, Sweden)*; A.V. Lukashin *(Moscow, Russia)*; V.A. Margulis *(Saransk, Russia)*; I.V. Melikhov *(Moscow, Russia)*; G.P. Miroshnichenko *(St. Petersburg, Russia)*; I.Ya. Mittova *(Voronezh, Russia)*; H. Neidhardt *(Berlin, Germany)*; K. Pankrashkin *(Orsay, France)*; A.V. Ragulya *(Kiev, Ukraine)*; V. Rajendran *(Tamil Nadu, India)*; A.A. Rempel *(Ekaterinburg, Russia)*; V.Ya. Rudyak *(Novosibirsk, Russia)*; D Shoikhet *(Karmiel, Israel)*; P Stovicek *(Prague, Czech Republic)*; V.M. Talanov *(Novocherkassk, Russia)*; A.Ya. Vul' *(St. Petersburg, Russia)*; V.A. Zagrebnov *(Marseille, France)*.

Editors:
I.V. Blinova; A.I. Popov; A.I. Trifanov; E.S. Trifanova *(St. Petersburg, Russia)*,
R. Simoneaux *(Philadelphia, Pennsylvania, USA)*.

Address: University ITMO, Kronverkskiy pr., 49, St. Petersburg 197101, Russia.
Phone: +7(812)232-67-65, **Journal site:** http://nanojournal.ifmo.ru/,
E-mail: popov1955@gmail.com

AIM AND SCOPE

The scope of the journal includes all areas of nano-sciences. Papers devoted to basic problems of physics, chemistry, material science and mathematics inspired by nanosystems investigations are welcomed. Both theoretical and experimental works concerning the properties and behavior of nanosystems, problems of its creation and application, mathematical methods of nanosystem studies are considered.

The journal publishes scientific reviews (up to 30 journal pages), research papers (up to 15 pages) and letters (up to 5 pages). All manuscripts are peer-reviewed. Authors are informed about the referee opinion and the Editorial decision.

CONTENT

Papers, presented at NANO-2015 In this issue we continue to publish works presented at International Conference on Nanomaterials and Nanotechnology (NANO 2015), 7-10 December 2015, Tamil Nadu, India.

NANOSYSTEMS: PHYSICS, CHEMISTRY, MATHEMATICS, 2016, 7 (4), P. 583–591

Optical properties of sodium niobate thin films

V. Lingwal[1], A. S. Kandari[2], N. S. Panwar[2]

[1]Pt. L.M.S. Govt. PG College Rishikesh, Uttarakhand, 249 201, India
[2]USIC, HNB Garhwal University, Srinagar (Garhwal), Uttarakhand, 246 174, India
lingwalv@yahoo.co.in, kandarialok@gmail.com, nspusic@gmail.com

PACS 77.55.fj, 78.20.Ci **DOI 10.17586/2220-8054-2016-7-4-583-591**

$NaNbO_3$ thin films were deposited under different conditions by rf magnetron sputtering of ceramic target. Spectral transmission of the deposited films was measured in the UV-Visible-near IR range. Films deposited at 300 °C showed more absorption, and films annealed at 300 °C showed less absorption than those deposited at room temperature (RT), which was found to be consistent with their X-ray diffraction (XRD) patterns. From the observed transmission spectra, refractive index, optical band gap, absorption coefficient, extinction coefficient and film thickness were calculated for the deposited films. Refractive index at 550 nm wavelength was found to be 2.11, 2.01 and 2.34 for the films deposited at RT, 300 °C and annealed at 300 °C, respectively. The refractive index was found to be almost constant with respect to frequency for the films annealed at 300 °C. Optical band gap was found 3.82, 3.7 and 3.81 eV for the films deposited at RT, 300 °C, and annealed at 300 °C, respectively. Film thickness was shown to decrease with annealing. Absorption and extinction coefficients decreased with increasing wavelength, in all the samples. Band gaps associated with different interactions have been calculated for the deposited films. Phonon assisted indirect forbidden transition was most favorable in the deposited films.

Keywords: Ferroelectrics, antiferroelectrics, thin films, sputtering, transmission.

Received: 27 January 2016

Revised: 21 June 2016

1. Introduction

The physical properties of thin film material depend on its thickness, surface to volume ratio, microstructure and microchemistry; which strongly depend on its growth process. The most conspicuous phenomena associated with thin films are optical ones. The studies on electric properties as well as the emission of electrons from thin films have made extraordinarily rapid advances in recent years, due to their wide tailor-made applications.

Dielectric materials employed in optical coatings include fluorides (e.g., MgF_2, CeF_3), oxides (e.g., Al_2O_3, TiO_2, SiO_2, Ta_2O_5), sulfides (e.g., ZnS, CdS), assorted compounds (e.g., ZnSe, ZnTe), etc. An essential common feature of dielectric optical materials is their low absorption coefficients ($\alpha < 10^3$/cm) in some relevant portion of the spectrum, where they are essentially transparent. Ferroelectric materials, such as $LiNbO_3$, $KNbO_3$, K(Ta, Nb)O_3, $PbTiO_3$ based materials, etc., are useful in optical applications, e,g., in infrared detectors, optical waveguide devices, optical memories and displays, spatial light modulators, frequency doublers for diode lasers, etc. [1–11]. Application of ferroelectric films in these devices hinges on successful integration of ferroelectric films into semiconductors or other useful substrates.

Nonmetallic materials may be opaque or transparent to visible light, and if transparent, they often appear colored. In principle, light radiation is absorbed in this group of materials by three basic mechanisms; viz., electronic polarization, electronic transitions across the band gap and electronic excitations to impurity or defect levels, which also influence their transmission characteristics. Absorption by electronic polarization is important only at light frequencies in the vicinity of the relaxation frequency of the constituent atoms. The other two mechanisms involve electron transitions, which depend on the electronic energy band structure of the materials; one of these absorption mechanisms involves the absorption as a consequence of electron excitations across the band-gap; the other is related to electron excitations to impurity or defect levels that lie within the band gap. Absorption of a photon may promote or excite an electron, across the band gap, from the nearly filled valence band to an empty state within the conduction band, thus creating a free electron in the conduction band and a hole in the valence band. The excitation energy E is related to the absorbed photon frequency (ν); i.e., $E = h\nu$. These excitations with the accompanying absorption can take place only if the photon's energy is greater than that of the band gap E_g, i.e., if $h\nu > E_g$. At the minimum wavelength for visible light, $E = 3.1$ eV, means no visible light is absorbed by nonmetallic materials having band gap energy (Eg) greater than about 3.1 eV; these materials, if of high purity, will appear transparent and colorless. Optical measurements constitute the most important means of determining the inter-band structure of the materials. Photon induced inter-band electronic transitions can occur between different bands. Also optical measurements can be used to study lattice vibrations.

In the present study, $NaNbO_3$ films were deposited on the quartz substrate using the rf magnetron sputtering method. Films were deposited at room temperature and at varying substrate temperatures. The room temperature deposited films were annealed at different temperatures. Optical parameters were measured for $NaNbO_3$ films deposited at room temperature, at 300 °C, and post deposition annealed at 300 °C. Deposited films were characterized using XRD method.

2. Preparation

Thin films of $NaNbO_3$ were deposited by the rf magnetron sputtering of bulk $NaNbO_3$ pellet targets. Films were deposited on to clean Quartz (Qz) and monocrystalline silicon surfaces. Ceramic pellets of $NaNbO_3$ of 36 mm diameter and 2.5 mm thickness were used as sputtering targets. The targets were prepared by the conventional solid-state reaction method. The pumping system used was a combination of 300 l/sec diffusion pump and a 200 l/min rotary pump. The system gives an ultimate vacuum of 3×10^{-5} mbar. The pressure was monitored using a Pirani and a Penning gauge combination. The vacuum chamber was a 300 mm diameter stainless steel cylinder. The target disk was mechanically clamped to a water-cooled assembly with magnetic arrangement. The system was arranged in sputter down configuration with a substrate-target distance of 30 mm. Separate feed-troughs were fitted for heater connections, and for the thermocouple that is used in contact with the substrate to estimate its temperature. Argon (99.999 %) was used as sputtering gas. An rf system from CVC Scientific Products Ltd, Wakingham, England, was used for sputtering. Films were deposited at a working pressure of 1×10^{-3} mbar, for 30 minutes, at different substrate temperatures. All the films were deposited at a forward power of 30 W, whereas reverse power was zero. The cleanliness of the substrate's surface exerts a decisive influence on film growth and adhesion. A thoroughly cleaned substrate is a prerequisite for the preparation of films with reproducible properties. Quartz substrates were rinsed with a laboratory detergent and then rinsed with distilled water and lastly wiped with soft dry cloth with little trace of acetone. The temperature of the substrate was monitored using a cromel-alumel thermocouple. The deposited films were left in the chamber for 2 hrs and then removed for experimental investigations. The films deposited at room temperature were annealed post-deposition, in a furnace at different temperatures, in the presence of ambient oxygen.

3. Characterization

3.1. X-ray diffraction patterns

The structures of the deposited $NaNbO_3$ films, at room temperature (RT) and at substrate temperature 225, 270, 300 and 375 °C, were studied by x-ray diffraction with the help of Philips Analytical X-ray Diffractometer (PW 3710), using $CuK\alpha_1$ radiation of wavelength 1.54056 Å. Peak indexing was done by using the Joint Committee on Powder Diffraction Standards (JCPDS) data cards. The XRD patterns obtained are shown in Fig. 1. The RT deposited films exhibited crystalline structure with different orientations. However, it has been reported earlier that oxide films deposited at RT, generally, show amorphous nature and crystalline structure is set at higher temperatures [12–15].

The experimental investigations have shown that the properties of oxides depend on its growth process and post annealing process [15]. To study the effect of annealing, films deposited at RT were annealed at 400, 500 and 600 °C. The XRD patterns of annealed films are depicted in Fig. 2.

From the XRD patterns of $NaNbO_3$ films deposited at different substrate temperatures (at 225, 270, 300 and 375 °C) (Fig. 1), it has been observed that films deposited at 225 and 270 °C show crystalline structure with single face orientation while films deposited at substrate temperatures of 300 and 375 °C showed amorphous nature.

From the XRD patterns of the annealed films (Fig. 2), it has been observed that annealing up to 500 °C changes the orientation of the deposited films, and annealing at higher temperature (600 °C) shows amorphous films. The observed amorphous nature of the films annealed at higher temperatures ($\geq$ 600 °C) may be due to a deficiency of volatile sodium ions. The films deposited at RT were oriented in (101) and (221) directions. Films deposited at substrate temperatures of 225 and 270 °C and the films annealed at 400 and 500 °C showed orientation towards the (002) plane. This orientation is due to the coalescing islands, which proceed until the film reaches continuity.

3.2. Transmission spectra

The spectral transmissions (at 6 ° angle of incidence) of the $NaNbO_3$ films were measured using a UV-visible-near infrared double beam spectrophotometer (Hitachi, model 330). The observed transmission spectra of the $NaNbO_3$ films deposited at different conditions are shown in Figs. 3 – 5. It has been observed that the films deposited at 300 °C substrate temperature show more absorption while those films annealed at 300 °C shows less

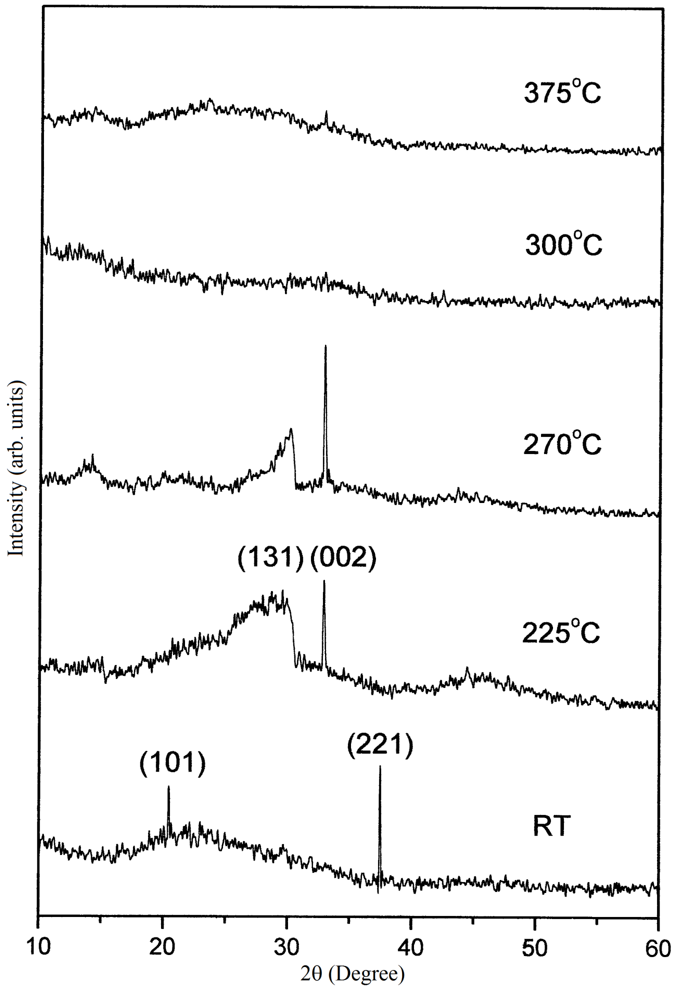

FIG. 1. X-ray diffraction patterns of $NaNbO_3$ films, deposited at different substrate temperatures

absorption than the films deposited at RT. The observed high absorption of the films also suggests an amorphous nature for the deposited films at higher substrate temperature, as has been observed in the XRD study. The lower absorption of the annealed films, at 300 °C, suggests a reorientation of the film crystallites in single face and also to the decrease in oxygen vacancies in the deposited films when annealed in the presence of ambient oxygen, as has been observed from the XRD patterns. The increase in absorption in the films, deposited at 300 °C, may be due to the higher oxygen deficiency and some amount of sodium deficiency, so the deposited films may not be in stoichiometric composition [16]. These deficiencies, in the films, may also be caused by the preferential sputtering, which removes atoms from the film leaving the deposited film sub-stoichiometric [17].

The preferential sputtering in oxide thin films can be explained on the basis of Winter and Sigmund model [16], according to which, the energy transfer coefficient in a head on collision process between an ion of mass m and a target of mass M is given by $E_T = 4mM/(m+M)^2$. Applying this equation to the collision of oxygen with oxygen and niobium atoms of the growing film, with oxygen, yields value of E_T as 1.0 for oxygen-oxygen and 0.5 for oxygen-niobium collision. This means that only 50 % of the energy is transferred in the case of oxygen-niobium collisions. Hence, more energy is delivered to the oxygen atoms than to the niobium atoms, leading to higher re-sputtering of oxygen atoms from the film. Compounds made up of elements with smaller difference in masses have fewer tendencies to be sputtered out from the film. The sub-stoichiometry causes degradation in the refractive index of the film.

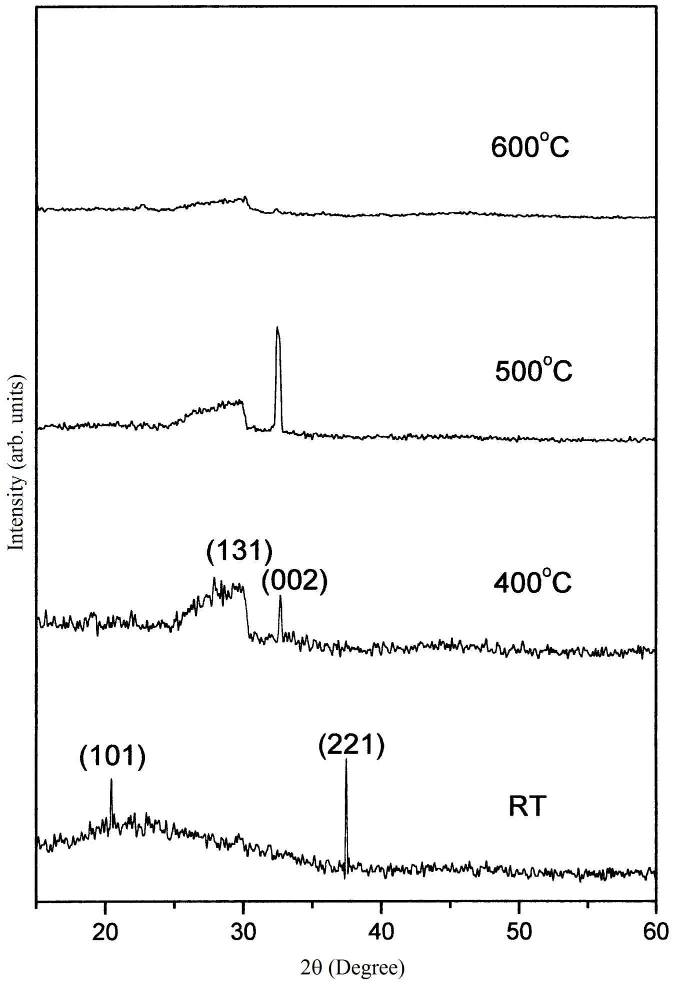

FIG. 2. X-ray diffraction patterns of $NaNbO_3$ films, deposited at room temperature (RT) and annealed at different temperatures

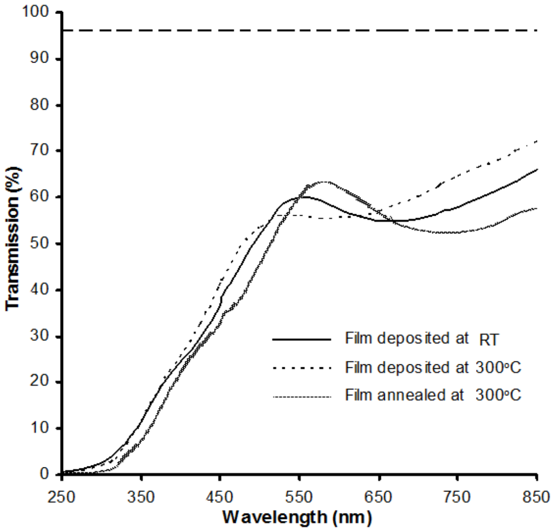

FIG. 3. Transmission spectra of $NaNbO_3$ films prepared at different conditions

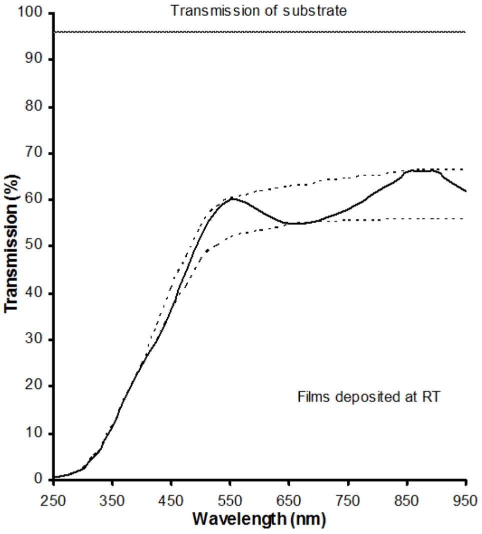

FIG. 4. Envelope of the transmission spectra of the $NaNbO_3$ films, deposited at RT

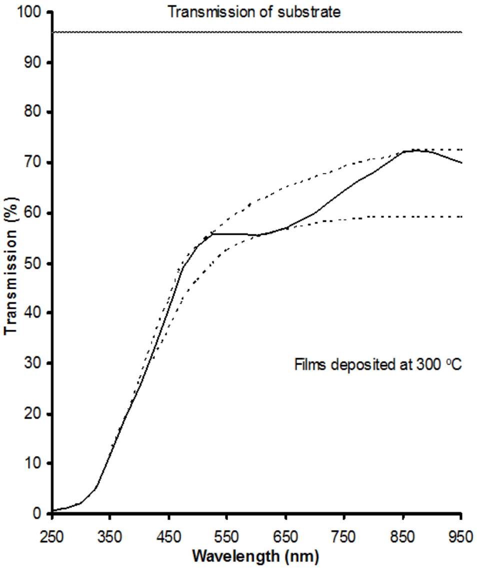

FIG. 5. Envelope of the transmission spectra of the NaNbO$_3$ films, deposited at 300 °C

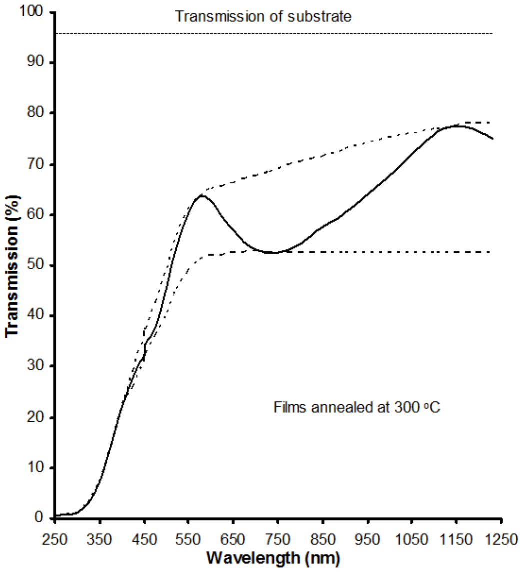

FIG. 6. Envelope of the transmission spectra of the NaNbO$_3$ films, annealed at 300 °C

4. Optical properties

Optical constants, such as, refractive index (n), optical band gap (E_g), absorption coefficient (α), extinction coefficient (k), and thickness of the films have been calculated, for NaNbO$_3$ films deposited on quartz (Qz) substrate ($n = 1.55$, transmittance $= 0.96$), using Swanepoel's envelope technique [18].

It is clear from Figs. 4 – 6 that the transmission in the film samples, deposited at the substrate temperature 300 °C, is lower than that the samples deposited at RT. It shows high absorption in the samples deposited at 300 °C substrate temperature, and thereby showing amorphous nature, which is in conformity with the results obtained from XRD patterns, Fig. 1. The film absorption has been reported to increase with high-level substrate temperature [12]. The absorption is low in the samples annealed at 300 °C, indicating good quality of NaNbO$_3$ films, Fig. 5. The low absorption in the films deposited at RT in comparison to that in the films annealed at 300 °C (as confirmed by XRD patterns, Fig. 2) may be attributed to the variation in the rate of re-crystallization, in these samples. Meanwhile, the peak transmission of all the films deposited in the present study is very much lower than that of the quartz substrate used, indicating very high absorption in these films. No many maxima and minima were observed in the transmission spectra of the present samples, which may be due to non-uniformity in the film thickness.

4.1. Refractive index (n)

According to Swanepoel's envelope technique [18], the refractive index (n), at wavelength λ, is given by

$$n(\lambda) = \left(N + \left(N^2 - n_s^2\right)^{1/2}\right)^{1/2},$$

where n_s is the refractive index of the substrate, at wavelength λ, and

$$N = \frac{2n_s\left[T_M(\lambda) - T_m(\lambda)\right]}{T_M(\lambda)\,T_m(\lambda)} + \frac{n_s^2 + 1}{2},$$

where $T_M(\lambda)$ and $T_m(\lambda)$ are the transmission maxima and minima, respectively, corresponding to wavelength λ obtained from the envelope, as shown in Figs. 3 – 5.

Figure 6 shows the calculated values of n with λ for the films deposited at different conditions. At 550 nm wavelength, the refractive index (n) values for films deposited at RT and 300 °C were 2.11 and 2.01, respectively; and 2.34 for the samples annealed at 300 °C. The degradation of n in the samples deposited at higher substrate temperature is due to sub-stoichiometry in the films due to preferential sputtering in the deposited films. Fig. 7 shows that n decreases with increasing wavelength for the films deposited at RT, and at 300 °C; while n remains almost constant for the samples annealed at 300 °C. The low value of packing density in the samples may be one of the reasons for the decrease in n with increasing wavelength, in the samples deposited at RT and at 300 °C, since these samples may be oxygen deficient. In the samples annealed at 300 °C, in the ambient oxygen atmosphere, the oxygen stoichiometry and hence the packing density improves, and n remains constant with varying wavelength. Value of n has been reported 2.21 for the single crystal of $NaNbO_3$ [19], at 550 nm.

4.2. Optical band gap

The excellent transmission of dielectric materials in the visible region of the spectrum is found to terminate at shorter wavelengths with the onset of the UV absorption edge. The critical radiation wavelength, λ_c, at which this occurs, is given by $\lambda_c(\mu m) = 1.24/E_g$ (eV). These values physically correspond to electronic transitions from the filled valence band levels, across the energy gap E_g, to the unfilled conduction band states. Multiple peaks near the UV absorption edge indicate the complexity of these processes. At long wavelengths, the high optical transmission is limited by absorption due to the vibration of lattice ions in resonance with the incident radiation. The frequency of maximum absorption is related to the force constant and masses of vibrating anions and cations. The optical band gaps for the films deposited at RT and at 300 °C has been calculated to be 3.82 and 3.7 eV, respectively; and for the films annealed, at 300 °C, this value was found to be 3.81 eV. The band gap for single $NaNbO_3$ crystal has been reported 3.4 eV [20].

4.3. Film thickness

The thickness (d) of the film is given by [18]:

$$d = \frac{\lambda_1 \lambda_2}{4\left(n_1 \lambda_2 - n_2 \lambda_1\right)},$$

where λ_1 and λ_2 are the wavelengths of two successive maxima and minima; n_1 and n_2 are the refractive indices at λ_1 and λ_2, respectively.

The calculated thicknesses of the films deposited at RT and 300 °C were obtained as 3455 and 5182 Å, respectively, while a value of 3132 Å was obtained for the films annealed at 300 °C after depositing at RT. The lowering of the thickness in the annealed samples may be explained on the basis of reduction of voids between islands during the process. The voids are filled up by coalescence process, recrystallization and reorientation of the film crystallites.

4.4. Absorption and inter-band transitions

Absorption coefficient (α) of the film is given by [18]:

$$\alpha = -\frac{\log(x)}{d},$$

where,

$$x = \frac{E_m - \left[E_m^2 - \left(n^2 - 1\right)^3 \left(n^2 - n_s^4\right)\right]^{1/2}}{\left(n - 1\right)^3 \left(n - n_s^2\right)},$$

with

$$E_m = \frac{8n^2 n_s}{T_M} + \left(n^2 - 1\right)\left(n^2 - n_s^2\right),$$

n is the refractive index of the film; T_m is the maximum transmission of the film, and d is the film thickness.

The absorption coefficient (α) was found to decrease with increased wavelength for all the $NaNbO_3$ films, deposited under different conditions. The calculated value of α was determined to be 4.67×10^3 /cm for the samples deposited at RT, at 550 nm wavelength. In the region of strong absorption, the interference fringes disappear. Values for n in strong absorption region were estimated by extrapolating the values calculated in the other parts of the spectrum [18].

The extinction coefficient (k), at wavelength λ, is given by:

$$k = \frac{\alpha \lambda}{4\pi}.$$

Observations, shown in Fig. 8, indicate that k decreases with increasing wavelength, for all the $NaNbO_3$ film samples, prepared under different conditions. Also, Absorption coefficient may be expressed as a function of the incident photon energy, $h\nu$, as [21]:

$$\alpha(h\nu) = A\left(h\nu - E_g\right)^m, \quad (1)$$

where A and m are constants, and the value of m decides the nature of transition. These observations may be analyzed according to this relation. The value of E_g has been calculated at and beyond the absorption edge. The variations of the absorption coefficient with the incident photon energy have been plotted for the estimation

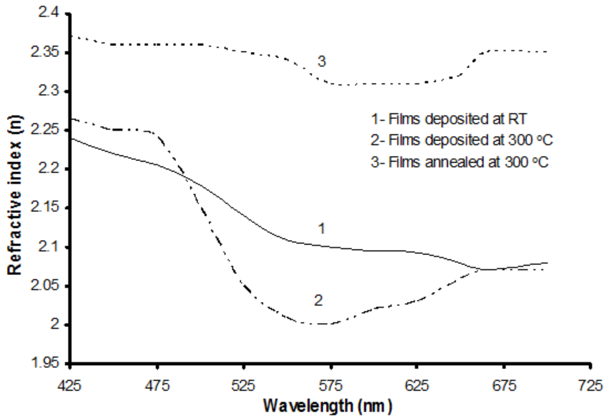

FIG. 7. Variation of refractive index with wavelength, of the $NaNbO_3$ films prepared at different conditions

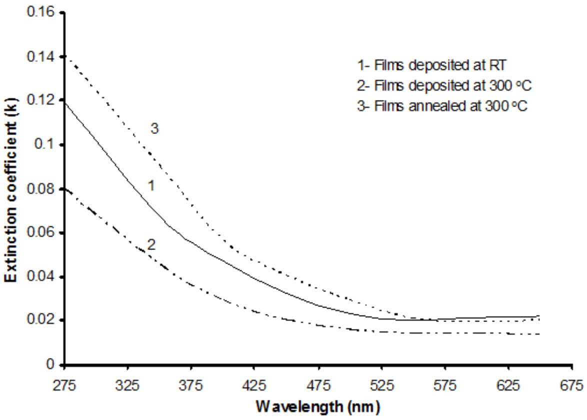

FIG. 8. Wavelength dependence of extinction coefficient of $NaNbO_3$ films, prepared at different conditions

of energy gap. The band gap was found to be composition dependent for dielectric films [22–25]. The radiation absorbed by a solid can be converted into elastic vibrations in it, and it may initiate photon-electron, photon-phonon and other interactions.

The photon-electron interaction leads to direct transition probability and this interaction satisfies Eq. (1) with $m = 1/2$. Figs. 9(a), 10(a) and 11(a) show α^2 *vs.* $h\nu$ curves, for the films deposited at RT, at 300 °C, and for the films annealed at 300 °C, respectively. Extrapolation of the straight portion of the curve, α^2 *vs.* $h\nu$, gives the direct allowed energy band gap of the film samples. The value for the direct allowed energy band gap was estimated from the intersection of the tangent, drawn near the absorption edge, in the α^2 *vs.* $h\nu$ plot (the straight line portion), with the energy axis. The direct allowed energy band gap values were obtained as 3.4 eV for the films deposited at room temperature and 300 °C, and 3.2 eV for the films annealed at 300 °C.

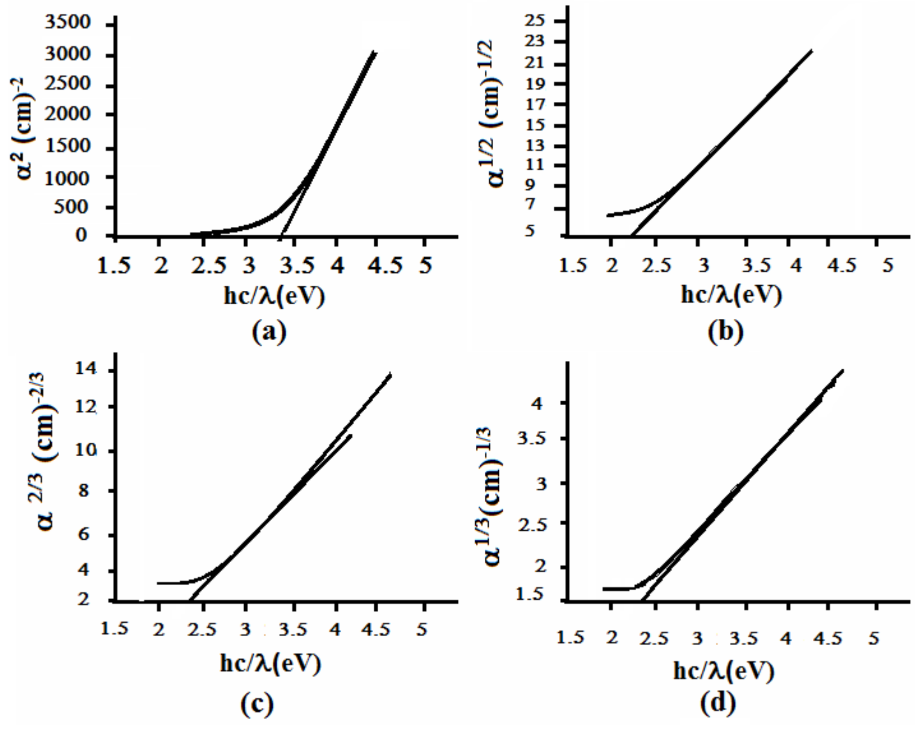

FIG. 9. α^m as a function of hc/λ, for different m values, in the samples deposited at RT

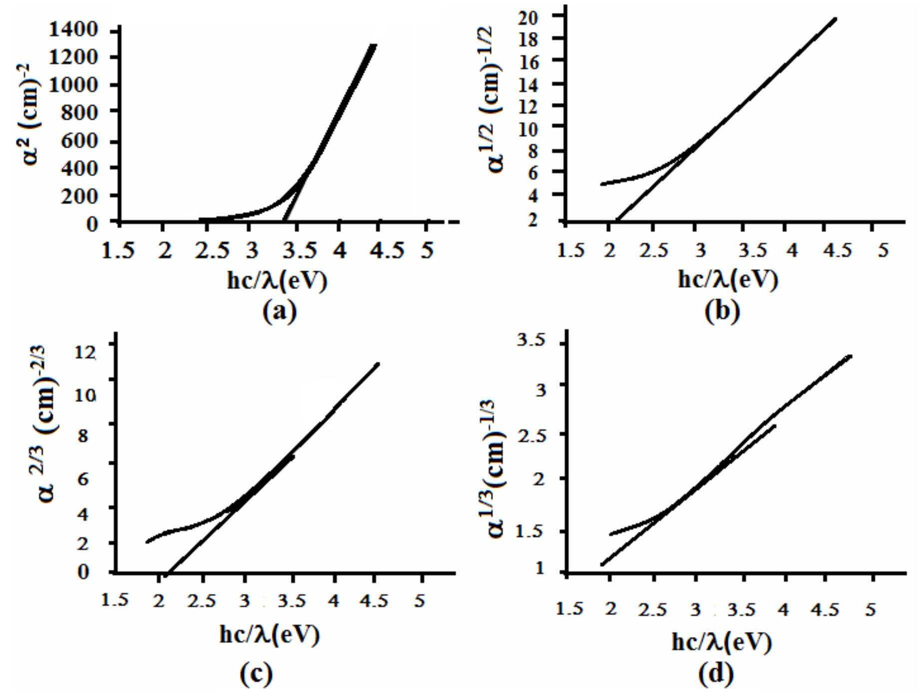

FIG. 10. α^m as a function of hc/λ, for different m values, in the samples deposited at 300 °C

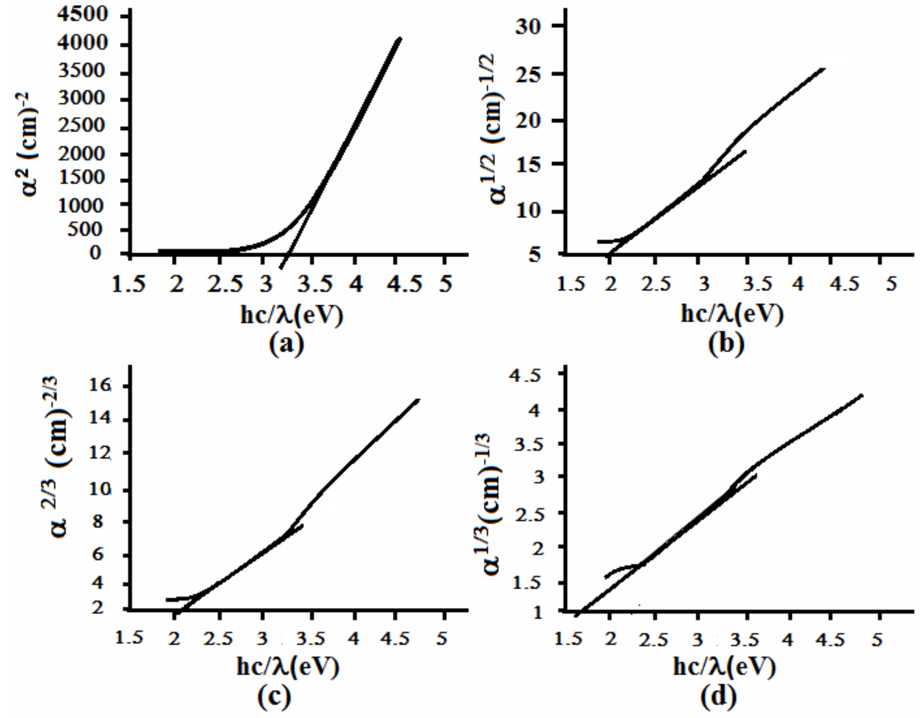

FIG. 11. α^m as a function of hc/λ, for different m values, in the samples annealed at 300 °C

The photon-phonon interaction leads to indirect allowed transition probability and is given by Eq. (1) with $m = 2$; and E_g is indirect allowed energy band gap. Figs. 9(b), 10(b) and 11(b) show the variation of $\alpha^{1/2}$ with $h\nu$. The indirect allowed energy band gap from the $\alpha^{1/2}$ *vs.* $h\nu$ plots is found to be 2.2, 2.09 and 2.0 eV; for the films deposited at RT, 300 °C, and for the films annealed at 300 °C, respectively.

In addition to the photon assisted electronic transitions there are phonon assisted interaction probabilities that give rise to the inter-band absorptions in the films corresponding to the energy levels in forbidden band. Excitons may be formed by direct photons only or by photon-phonon assistance. This direct absorption probability in the forbidden gap is given by Eq. (1) with $m = 3/2$; and the $\alpha^{2/3}$ *vs.* $h\nu$ plots are shown in Figs. 9(c), 10(c) and 11(c), for films prepared at different conditions. The values of direct forbidden gap energy (associated with this mechanism) were found to be 2.3, 2.06, and 2.12 eV, for the samples deposited at RT, at 300 $^\circ$C substrate temperature, and for the samples annealed at 300 $^\circ$C, respectively. Excitons may also be formed by photon-phonon interactions. The phonon assisted probabilities or indirect absorption probability in the forbidden gap is given by Eq. (1) with $m = 3$. Figs. 9(d), 10(d) and 11(d) shows $\alpha^{1/3}$ *vs.* $h\nu$ plot to obtain the indirect forbidden energy gap E_g, associated with this mechanism. The values of indirect forbidden energy gap E_g were found to be 2.24, 1.86, and 1.63 eV, for the samples deposited at RT, at 300 $^\circ$C and for the samples annealed at 300 $^\circ$C, respectively.

From these measurements, the most satisfactory representation is obtained for $\alpha^{1/3}$ *vs.* $h\nu$ plot, which suggests phonon assisted indirect forbidden transitions in the deposited $NaNbO_3$ films.

References

[1] Gunther P. Nonlinear optical crystals for optical frequency doubling with laser diodes. *Proc. SPIE*, 1981, **236**, P. 8–19.

[2] Okuyama M., Matsui Y., Nakano H., Hamakawa Y. $PbTiO_3$ ferroelectric thin film gate fet for infrared detection. *Ferrelectrctrics*, 1981, **33** (1), P. 235–241.

[3] Hewig G.H., Jain K. Frequency doubling in a $LiNbO_3$ thin film deposited on sapphire. *J. Appl. Phys.*, 1983, **54** (1), P. 57–61.

[4] Baumert J.C., Hoffnagle J., Gunther P. Nonlinear optical effects in $KNbO_3$ crystals at $Al_xGa_{1-x}As$, dye, ruby and Nd:YAG laser. *Proc. SPIE*, 1984, **492**, P. 374–386.

[5] Iijimo K., Tomita Y., Takayama R., Ueda I. Preparation of C-axis orientated $PbTiO_3$ thin films and their crystallographic, dielectric, and pyroelectric properties. *J. Appl. Phys.*, 1986, **60** (1), P. 361–367.

[6] Martin S.J., Butler M.A., Land C.E. Ferroelectric optical image comparator using PLZT thin films. *Electron. Lett.*, 1988, **24** (24), P. 1486–1487.

[7] Krishnakumar S., Oguz V.H., et al. Deposition and characterization of thin ferroelectric lead lanthanum zirconate titanate (PLZT) films on sapphire for spatial light modulators applications. *IEEE Trans. Ultrason. Ferrelec. Freq. Contr.*, 1991, **38** (6), P. 585–590.

[8] Ivey M., Mancha S., Carter R. Optical information storage and charge traps in PZT thin films. *IEEE Trans. Ultrson. Ferroelec. Freq. Contr.*, 1991, **38** (4), P. 337–343.

[9] Tamada H., Yamada A., Saitoh M. $LiNbO_3$ thin film optical waveguide grown by liquid phase epitaxy and its application to second-harmonic generation. *J. Appl. Phys.*, 1991, **70** (5), P. 2536–2541.

[10] Gutmann R., Hullinger J., Hauert R., Mosser E.M. Auger electron and x-ray photoelectrons spectroscopy of monocrystalline layers of $KTa_{1-x}Nb_xO_3$ grown by liquid-phase epitaxy. *J. Appl. Phys.*, 1991, **70** (5), P. 2648–2653.

[11] Polla D.I., Ye C., Tamagawa T. Surface-micromachined $PbTiO_3$ pyroelectric detectors. *Appl. Phys. Lett.*, 1991, **59** (1), P. 3539–3544.

[12] Sreenivas K., Mansingh A., Sayer M. Structural and electrical properties of rf-sputtered amorphous barium titanate thin films. *J. Appl. Phys.*, 1987, **62** (11), P. 4475–4481.

[13] Rabson T.A., Baumann R.C., Rost T.A. Thin film lithium niobate on silicon. *Ferroelectrics*, 1990, **112** (1), P. 265–271.

[14] Krupanidhi S.B., Mohan Rao G. Pulsed laser deposition of strontium titanate thin films for dynamic random access memory applications. *Thin Solid Films*, 1994, **249** (1), P. 100–108.

[15] Pignolet A., Mohan Rao G., Krupanidhi S.B. Rapid thermal processed thin films of reactively sputtered Ta_2O_5. *Thin Solid Films*, 1995, **258** (1–2), P. 230–235.

[16] Smith R.A. *Wave Mechanics of Crystalline Solids*. North Holland publication, Amsterdam, 1972.

[17] Rubio J.D., Albella J.M., Martinez-Duart J.M. Sputtered Ta_2O_5 antireflecting coating for silicon solar cells. *Thin Solid Films*, 1982, **90** (4), P. 405–408.

[18] Swanepoel S. Determination of the thickness and optical constants of amorphous silicon. *J. Phys. E: Sci. Inst.*, 1983, **16** (12), P. 1214–1222.

[19] Landolt H., Börnstein R. et al. *Numerical Data and Functional Relationships in Science and technology*, **16**, Group III, *Crystal and Solid State Physics*. Springer Verlag Berlin, Heidelberg-New York, 1981.

[20] Raevskii I.P., Reznichenko L. Phase transitions and electrical properties of ferroelectric solid solution based on $NaNbO_3$. *Izestiva Akademii Nauk SSSR, Neorganicheskie Mater.,* 1979, **15** (5), P. 872–875.

[21] Sze S.M. *Physics of Semiconductor Devices*. Wiley publication, New York, 2000.

[22] Pankove J.J. *Optical Processes in Semiconductors*. Prentice Hall, New Jersey, 1956.

[23] Sze S.M. Current transport and maximum dielectric strength of silicon nitride films. *J. Appl. Phys.*, 1967, **38** (7), P. 2951–2955.

[24] Kittel C. *Solid State Physics*. John Wiley and Sons, New York, 1970.

[25] Michael S. *Physics of Semiconductor Devices*. Prentice Hall of India Pvt. Ltd., New Delhi, 1995.

NANOSYSTEMS: PHYSICS, CHEMISTRY, MATHEMATICS, 2016, 7 (4), P. 592–594

$\mathbf{In_4Mg_3}$ in $\mathbf{In_xMg_3}$ $(x = 1 - 6)$ series: a magic unit for future smart materials

Debesh R. Roy*, Majid Shaikh, Vipin Kumar
Department of Applied Physics, S. V. National Institute of Technology, Surat 395007, India
drr@ashd.svnit.ac.in

PACS 36.40.-c, 81.05.Dz, 61.46.Bc, 31.15.E **DOI 10.17586/2220-8054-2016-7-4-592-594**

Systematic investigation on the stability and electronic properties of a series of bimetallic (semiconductor-alkaline earth) clusters, viz., $\mathrm{In}_x\mathrm{Mg}_3$ $(x = 1-6)$ is performed, in the search for exceptionally and/or unusually stable motifs. A very popular hybrid exchange-correlation functional, B3LYP as proposed by A. D. Becke is employed for this purpose under the density functional formalism. The magic stability among the concerned clusters is explained using the jellium model. It is evident from the present study that the magic stability of $\mathrm{In}_4\mathrm{Mg}_3$ cluster arises due to the jellium shell closure and found as a potential building block for future novel semiconductor materials.

Keywords: Magic clusters, jellium model, density functional theory, smart materials.

Received: 27 January 2016. Revised: 16 May 2016.

1. Introduction

As a consequence of the discovery of fullerene [1], atomic and molecular clusters have gained immense attention as the potential candidates for designing novel nanomaterials [2–4]. The most important fact is that atomic clusters of sub-nano or nano-scale dimensions exhibits drastic differences in the physicochemical properties compared to their bulk counterparts, due to the effect of quantum confinement. This important behavior of nano-scale materials are found to be very useful in various technical applications over the last two decades or so [1–7].

In order to overcome the usual meta-stable nature of many clusters, one main focus of researchers is to search for the clusters with unusual or exceptional stability and/or useful physicochemical properties. The jellium is a quantum mechanical model of interacting electrons within an infinite volume of space and neutralized with an artificially assumed uniformly distributed background positive charge [8]. The jellium is usually treated within the density functional theory (DFT) [9, 10], since at zeroth temperature the properties of a jellium depend solely on electron density (ρ) [8]. Through an experimental mass spectra of a series of sodium clusters, W. D. Night et al. [11] have noticed that sodium clusters with a certain total number of valence electrons, viz., 2, 8, 18, 20, 34, 40, 52, …etc. shows exceptional stability compared to their neighbors. Such exceptionally stable clusters are named as magic clusters, and based on the jellium model as mentioned above and similar to the electronic shell structure of atom, they have proposed a new cluster valence shell structure in terms of the total valence electrons of the magic clusters as $1S^2 1P^6 1D^{10} 2S^2 1F^{14} 2P^6 \ldots$. Such cluster shell structure essentially represents the total valence electrons as observed for magic clusters with shell closure as $2(1S^2)$, $8(1S^2 1P^6)$, $18(1S^2 1P^6 1D^{10})$, $20(1S^2 1P^6 1D^{10} 2S^2)$, $34(1S^2 1P^6 1D^{10} 2S^2 1F^{14})$ etc. The exceptionally stable cluster motifs may have potency for utilizing them as the building blocks for designing novel cluster assembled materials.

The purpose of the present work is to perform a detailed study on the geometries, electronic properties as well as to search for any unusual and/or exceptionally stable cluster building motifs from the $\mathrm{In}_x\mathrm{Mg}_3$ $(x = 1-6)$ cluster series. The electronic properties include energy gain in adding an indium atom (ΔE_{In}) to the previous sizes, HOMO-LUMO energy gap (*HLG*), ionization potential (*I.P.*), chemical hardness (η) etc.

2. Theory and computation

The energy gain (ΔE_{In}) in forming $\mathrm{In}_x\mathrm{Mg}_3$ clusters by adding an indium atom to the previous $\mathrm{In}_{x-1}\mathrm{Mg}_3$ $(x = 1-6)$ size is given as:

$$\Delta E_{\mathrm{In}} = E\left(\mathrm{In}\right) + E\left(\mathrm{In}_{x-1}\mathrm{Mg}_3\right) - E\left(\mathrm{In}_x\mathrm{Mg}_3\right), \tag{1}$$

where $E(\mathrm{In}_x\mathrm{Mg}_3)$, $E(\mathrm{In}_{x-1}\mathrm{Mg}_3)$ and $E(\mathrm{In})$ are the total energies of the $\mathrm{In}_x\mathrm{Mg}_3$, $\mathrm{In}_{x-1}\mathrm{Mg}_3$ clusters and of the In atom, respectively.

Using Koopmans' finite difference approximation, the ionization potential (*IP*) and electron affinity (*EA*) can be expressed in terms of the highest occupied (ϵ_{HOMO}) and the lowest unoccupied (ϵ_{LUMO}) molecular orbital energies as:

$$IP \approx -\epsilon_{HOMO}; \qquad EA \approx -\epsilon_{LUMO}. \tag{2}$$

The chemical hardness can be expressed in terms of ϵ_{HOMO} and ϵ_{LUMO} as follows:

$$\eta \approx \frac{IP - EA}{2} \approx \frac{\epsilon_{LUMO} - \epsilon_{HOMO}}{2}. \tag{3}$$

The theoretical investigations are carried out within the density functional theory (DFT) framework [9, 10]. A molecular orbital approach, using a linear combination of atomic orbitals, is applied to probe the electronic structure. The actual DFT based calculations are performed using GAUSSIAN 09 [12] program. We have used B3LYP exchange-correlation functional [13] and LANL2DZ basis sets [14] for our calculations. A large number of initial guesses in every possible way is considered for each of the $\mathrm{In}_x\mathrm{Mg}_3$ $(x = 1 - 6)$ clusters to predict their ground state structures. The geometries of optimized clusters are drawn with CHEMCRAFT [15] visualization software.

3. Results and discussion

The ground state structures of $\mathrm{In}_x\mathrm{Mg}_3$ $(x = 1 - 6)$ clusters along with the geometrical bond lengths and point groups is represented in Fig. 1. The point group of various structures is considered within the tolerance limit of 0.1 Å. The profile of energy gain (ΔE_{In}) in forming each clusters by adding one indium atom to an existing $\mathrm{In}_{x-1}\mathrm{Mg}_3$ $(x = 1 - 6)$ cluster is provided in Fig. 2.

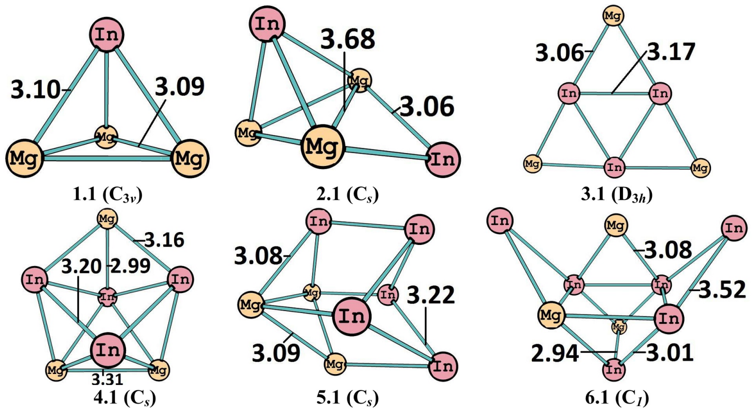

1.1 (C_{3v}) 2.1 (C_s) 3.1 (D_{3h})

4.1 (C_s) 5.1 (C_s) 6.1 (C_1)

FIG. 1. Ground state structures and associated point groups of $\mathrm{In}_x\mathrm{Mg}_3$ $(x = 1 - 6)$ clusters. Isomer $x.n$ $(x = 1 - 6)$ represents the clusters with x boron atoms in its lowest energy state $(n = 1)$. The bold numbers on the cluster images show a few representative bond distances between In–In, Mg–Mg and In–Mg atoms in Angstroms (Å)

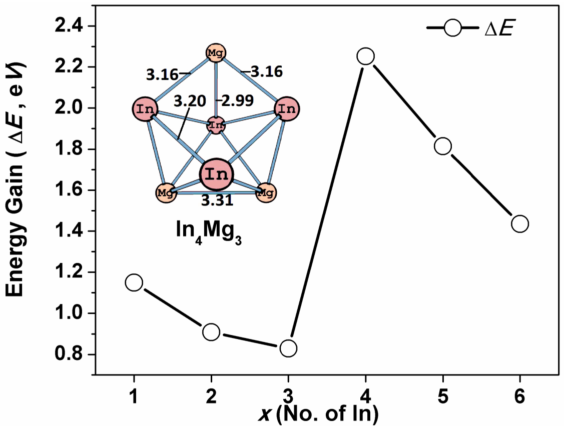

FIG. 2. Energy gain (ΔE) of $\mathrm{In}_x\mathrm{Mg}_3$ clusters, in adding an indium atom to an existing $\mathrm{In}_{x-1}\mathrm{Mg}_3$ $(x = 1{-}6)$ cluster. The bold numbers on the cluster image show few representative bond distances between In–In, Mg–Mg and In–Mg atoms in Angstroms (Å)

It can be noticed that, In_4Mg_3 cluster has very high energy gain (2.25 eV) compared to its neighboring clusters, implying its exceptional stability in the considered series. The stability of In_4Mg_3 is expected from the jellium framework since the number of valence electrons of the system is 18, which is a magic number with cluster electronic shell closure as $1S^2 1P^6 1D^{10}$. Table 1 provides the energy gain (ΔE_{In}), HOMO-LUMO energy gap (HLG), ionization potential (IP), electron affinity (EA) and chemical hardness (η) of the In_xMg_3 ($x = 1-6$) clusters. The maximum values of ΔE_{In} (2.25 eV) for In_4Mg_3 cluster justifies itself as the most stable motif in the series. The stability of the In_4Mg_3 cluster is further confirmed by its large I.P. (4.31 eV) value.

TABLE 1. Energy gain in adding an In atom (ΔE) to an existing $In_{x-1}Mg_3$ ($x = 1-6$), HOMO-LUMO energy gap (*HLG*), ionization potential (*IP*), electron affinity (*EA*) and chemical hardness (η) of the In_xMg_3 ($x = 1-6$) clusters

X	ΔE *(eV)*	*HLG (eV)*	*IP (eV)*	*EA (eV)*	η *(eV)*
1	1.15	2.20	4.36	2.16	1.10
2	0.91	1.23	3.58	2.35	0.62
3	0.82	0.85	3.71	2.86	0.42
4	2.25	1.19	4.31	3.12	0.60
5	1.82	1.95	4.34	2.39	0.98
6	1.44	1.55	4.26	2.71	0.77

In summary, In_4Mg_3 cluster is identified as a new magic cluster in the family of bimetallic magic clusters [16–18]. The possibility of utilizing In_4Mg_3 cluster as a potential building block for future cluster assembled materials by linking them with suitable inorganic/organic linkers is currently being investigated in our laboratory.

4. Conclusions

A detail theoretical study was performed in the search for exceptionally stable or magic clusters in the In_xMg_3 ($x = 1-6$) series. In_4Mg_3 shows magic stability with the effect of jellium shell closure. The significant energy gain, HOMO-LUMO energy gap (*HLG*), ionization potential, chemical hardness and electron affinity explain the origin of the extraordinary stability of In_4Mg_3 motif and imply its suitability to be considered as a building motif for novel inorganic nanomaterials. Also, the HLG value for In_4Mg_3 as 1.19 eV implies an initial classification for its suitability for application towards the design of novel semiconductor materials.

Acknowledgements

DRR is thankful to the SERB, New Delhi, Govt. of India, for financial support.

References

[1] Kroto H.W., Heath J.R., et al. C_{60}: buckminsterfullerene. *Nature*, 1985, **318** (6042), P. 162–163.

[2] *Handbook of nanotechnology* (3rd Ed.), Ed. Bhushan B., Springer, NY, 2010.

[3] Jena P., Castleman Jr A.W. *Nanoclusters: A Bridge Across Disciplines. A bridge across disciplines*, 2010, (Vol. 1), Elsevier.

[4] Song Y., Fu F., et al. The Magic Au_{60} Nanocluster: A New Cluster?Assembled Material with Five Au13 Building Blocks. *Angew. Chem. Int. Ed.*, 2015, **127** (29), P. 8550–8554.

[5] Chattaraj P.K., Roy D.R. Aromaticity in polyacene analogues of inorganic ring compounds. *J. Phys. Chem. A*, 2007, **111** (21), P. 4684-4696.

[6] Roy D.R. A DFT study on group III and V combined hexagonal clusters as potential building motifs for inorganic nanomaterials. *J. Mol. Struct.*, 2012, **1007**, P. 203–207.

[7] Lim S.Y., Shena W., Gao Z. Carbon quantum dots and their applications. *Chem. Soc. Rev.*, 2015, **44** (1), P. 362–381.

[8] Hughes R.I.G. Theoretical practice: the Bohm-Pines quartet. *Perspectives on science*, 2006, **14** (4), P. 457–524.

[9] Hohenberg P., Kohn W. Inhomogeneous electron gas. *Phys. Rev. B*, 1964, **136** (3), P. 864.

[10] Kohn W., Sham L.J. Self-consistent equations including exchange and correlation effects. *Phys. Rev. A*, 1965, **140** (4), P. 1133.

[11] Knight W.D., et al. Electronic shell structure and abundances of sodium clusters. *Phys. Rev. Lett.*, 1984, **52** (24), P. 2141.

[12] Frisch M.J., et. al. Gaussian 09, R-D.01. Gaussian, Inc., Pittsburgh PA, 2013.

[13] Becke A.D. Density-functional thermochemistry. III. The role of exact exchange. *The J. Chem. Phys.*, 1993, **98** (7), P. 5648–5652.

[14] Hay P.J., Wadt W.R. Ab initio effective core potentials for molecular calculations. Potentials for the transition metal atoms Sc to Hg. *J. Chem. Phys.*, 1985, **82** (1), P. 270–283.

[15] Chemcraft. Zhurko, G.A., Zhurko, D.A. `http://www.chemcraftprog.com`.

[16] Claridge S.A., Castleman A.W. Jr., et. al. Cluster-assembled materials. *ACS Nano*, 2009, **3**, P. 244–255.

[17] Castleman Jr.A.W., Khanna S.N. Clusters, Superatoms, and Building Blocks of New Materials. *J. Phys. Chem. C*, 2009, **113**, P. 2664–2675.

[18] Roy D.R., Singh P.K. Magic Stability of Ga_4Mg_3 Cluster in Ga_xMg_3 ($x = 1-6$) Series: A Density Functional Study. *Chem. Phys.*, 2013, **411**, P. 6–10.

NANOSYSTEMS: PHYSICS, CHEMISTRY, MATHEMATICS, 2016, 7 (4), P. 595–598

Structural and magnetic properties of $BaCo_{2-x}Ni_xFe_{16}O_{27}$ hexagonal ferrite prepared by a simple heat treatment method

Chetna C. Chauhan[1a], Rajshree B. Jotania[2b]

[1]Institute of Technology, Nirma University, Ahmedabad – 382 481, Gujarat, India
[2]Department of Physics, University School of Sciences, Gujarat University, Ahmedabad – 380 009, Gujarat, India
[a]chetna.chauhan@nirmauni.ac.in, [b]rbjotania@gmail.com

PACS 61.05.cp, 75.50.Vs, 75.60.Ej, 81.05.-t, 81.07.Wx **DOI 10.17586/2220-8054-2016-7-4-595-598**

A series of nickel-doped barium cobalt hexagonal ferrite samples with chemical composition $BaCo_{2-x}Ni_xFe_{16}O_{27}$ (x = 0.4, 0.8, 1.2, 1.6 and 2.0) were prepared using a simple heat treatment method. The dried precursor was calcined at 650 °C for 3 hours in a muffle furnace and slowly cooled to room temperature in order to obtain nickel-doped barium cobalt hexagonal ferrite powder. The prepared hexagonal ferrite powder samples were characterized using X-ray diffraction (XRD) and Vibrating Sample Magnetometer (VSM) techniques in order to study the effect of nickel substitution on structural and magnetic properties of barium cobalt hexagonal ferrites. The XRD analysis confirms the formation of mixed phases of W, M and spinel (S). The prepared powders exhibited single and multi-domain structures.

Keywords: Nickel doped barium cobalt hexagonal ferrites, heat treatment method, structural and magnetic measurements.

Received: 28 January 2016

Revised: 25 May 2016

1. Introduction

Barium hexaferrites possess magnetoplumbite crystal structure and have been extensively studied because of their large intrinsic uniaxial anisotropy and high Curie temperature, which make them widely used as permanent magnets, microwave devices and high density magnetic recording media, microwave absorbers, components and shielding [1–3]. Hexagonal ferrites are used in various components at high frequency range due to their high magnetic anisotropy, high Curie temperature, mechanical hardness, very low electrical conductivity, low dielectric loss, excellent chemical stability and corrosion resistance; their magnetic properties arise from the interactions between metallic ions occupying particular positions relative to the oxygen ions in its hexagonal crystalline structure [4, 5]. It is well known that structural and magnetic properties of barium hexaferrites strongly depend upon preparation method, substitution of Fe with other kind of ions and amount [6]. W-type hexagonal ferrites possess seven different sites ($4f_{IV}$, 2d, 12k, 6g, 4f, $4f_{VI}$ and 4e) in hexagonal crystal lattice, out of them five are magnetic sites. Iron ions are distributed among these sites of hexagonal crystal lattice [7]. Substitution of divalent or trivalent ions among various sublattices of hexagonal lattice can be used to improve intrinsic magnetic properties of barium hexaferrites [7]. During last decade various efforts have been made to improve structural and magnetic properties of barium hexaferrites by divalent and trivalent substitutions [8–10].

In the present investigation, a simple heat tratment method is adopted to prepare nickel substituted barium cobalt hexaferrite powder. The main objective of present investigation is to study the effect of nickel substitution on structural and magnetic properties of $BaCo_{2-x}Ni_xFe_{16}O_{27}$ (x = 0.4, 0.8, 1.2, 1.6 and 2.0) hexaferrite powder prepared by a simple heat treatment method and calcined at 650 °C for 3 hours.

2. Experimental

A series of $BaCo_{2-x}Ni_xFe_{16}O_{27}$ (x = 0.4, 0.8, 1.2, 1.6 and 2.0) hexaferrite is synthesized using high purity metal nitrate reagent as precursors, polyvinyl pyrrolidone (PVP) $[(C_6H_9NO)_n]$ as a capping agent to reduce the agglomeration of the magnetic particles and deionized water was used as the solvent. The aqueous PVP solution is prepared by dissolving 3 g of polymer in 100 ml of deionized water and kept at 70 °C. Next, 1.6 mmol of iron nitrate $[(Fe(NO_3)_2)]$, 0.1 mmol of barium nitrate $[Ba(No_3)_2]$, 0.2 mmole of cobalt nitrate $[(CoN_2O_6 \cdot 6H_2O)]$ and 0.4 mmole nickel nitrate $[Ni(NO_3)_2]$ solution was added into PVP solution and then kept on a magnetic stirrer for 2 hours. The mixed solution was heated at 80 °C and the resulting orange thick slurry was recovered. The obtained slurry was heated at 650 °C for 3 hours to obtain nickel-doped barium cobalt hexaferrite powder, which was crushed in to fine powder using a mortar and pastel. The same procedure is repeated for x = 0.8, 1.2, 1.6 and 2.0 samples.

3. Results and discussion

3.1. Crystal Structure

A Bruker D. Z. Phaser diffractometer (PW 1830) revealed X-ray powder diffraction (XRD) pattern when using Cu-Kα radiation (λ = 1.5405 Å) with a step scan of 0.02 °C/min to determine the crystal structure of ferrite powder. Fig. 1 shows the XRD patterns of $BaCo_{2-x}Ni_xFe_{16}O_{27}$ (x = 0.4, 0.8, 1.2, 1.6, 2.0) powder samples. The XRD analysis reveals presence of W-ferrites (JCPDS No. 78-0135), M-ferrites (JCPDS No. 43-0002) and S-ferrites Fe_3O_4 (JCPDS file – PDF # 790417) in final product; both W and M possess hexagonal while S possesses spinel crystal structure. No traces of α-Fe_2O_3 was noted, as was observed in Ba-Ca hexaferrite [11, 12] prepared by the sol gel technique. It is reported [13] that the unit cell of W phase is closely related to the M-phase, the only difference is that the successive R blocks are inter placed by two S-blocks instead of one as in the M-phase. It has also been reported by other researcher [14] that W-type hexagonal ferrite is chemically unstable and some of W-phase decomposed with the M-phase.

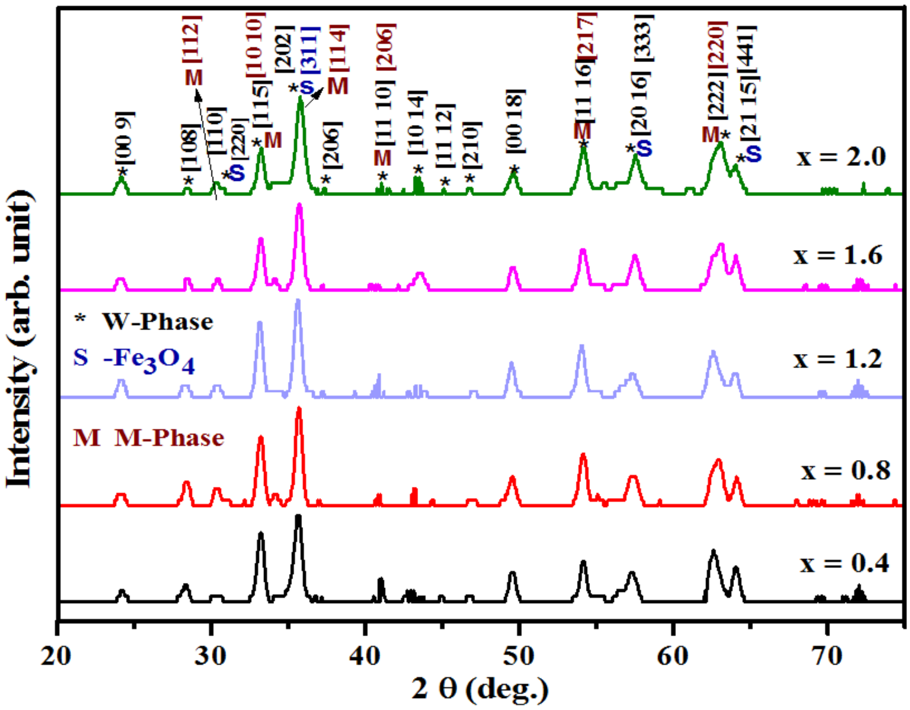

FIG. 1. X-ray diffraction patterns of $BaCo_{2-x}Ni_xFe_{16}O_{27}$ (x = 0.4, 0.8, 1.2, 1.6, 2.0) powder samples prepared using a simple heat treatment method and calcinated at 650 °C for 3 hours

The variation of lattice parameters a, c their ratio (c/a) and cell volume with the substitution of nickel are listed in Table 1. It is clear from Table 1 that value of (c/a) for all the samples remains constant. This behavior can be explained on the basis of ionic radii of the substituted ions. The ionic radius of Co^{+2} is 0.65 Å, which is nearly of the same order of that of Ni^{+2} ions (0.69 Å). This confirms that Ni^{+2} ions replaces Co^{+2} ions in the structure without disturbing the hexagonal symmetry. The average crystalline size (D_{xrd}) of the prepared $BaCo_{2-x}Ni_xFe_{16}O_{27}$ (x = 0.4, 0.8, 1.2, 1.6, 2.0) powder samples is calculated from the strongest Bragg peak [202] based on the Debye-Scherrer formula [15] shown in Table 2.

3.2. Magnetic Properties

The magnetic properties of the hexagonal ferrite powders are recorded at room temperature on a vibrating sample magnetometer (VSM) (Lake Shore, Model 7404). Fig. 2(a) shows the field dependence of the magnetization curves for $BaCo_{2-x}Ni_xFe_{16}O_{27}$ (x = 0.4, 0.8, 1.2, 1.6, 2.0) samples measured at room temperature under an applied field of 12.5 KOe. Saturation Magnetization (Ms), Coercivity (Hc), retaintivity (Mr) and squareness ratio (Mr/Ms) have been calculated from obtained hysteresis loops and listed in Table 2. The variation of Ms, Mr and Mr/Ms with nickel content (x) is shown in Fig. 2(b). The saturation magnetization and remanence values are found higher in $x = 0.8$ sample. The saturation magnetization and coercive field values were found

TABLE 1. Lattice constant a, c, ratio (c/a), volume of unit cell (V) and crystallite size (D_{xrd}) of $BaCo_{2-x}Ni_xFe_{16}O_{27}$ hexaferrite samples

Nickel Concentration (x)	**Lattice Parameter** a [Å]	**Lattice Parameter** c [Å]	(c/a)	**Cell Volume** V **[Å]^3**	**Crystalline size** D_{xrd} **[nm]**
0.4	5.885	33.100	5.624	992.747	15.55 ± 0.78
0.8	5.885	33.105	5.625	992.898	15.58 ± 0.78
1.2	5.885	33.109	5.626	993.018	15.09 ± 0.75
1.6	5.810	32.846	5.653	960.180	14.38 ± 0.72
2.0	5.819	32.995	5.670	967.526	13.19 ± 0.66

TABLE 2. Room temperature Magnetic parameters of $BaCo_{2-x}Ni_xFe_{16}O_{27}$ samples prepared by a simple heat treatment method and calcined at 650 °C for 3 hours

Ni concent (x)	***Ms*** **[emu/g]**	***Mr*** **[emu/g]**	***Hc*** **[KOe]**	***R=(Mr/Ms)***
0.4	22.67	8.42	1.20	0.37
0.8	37.77	18.00	1.00	0.47
1.2	20.29	7.75	0.99	0.38
1.6	27.04	12.25	0.85	0.45
2.0	22.62	6.01	0.21	0.27

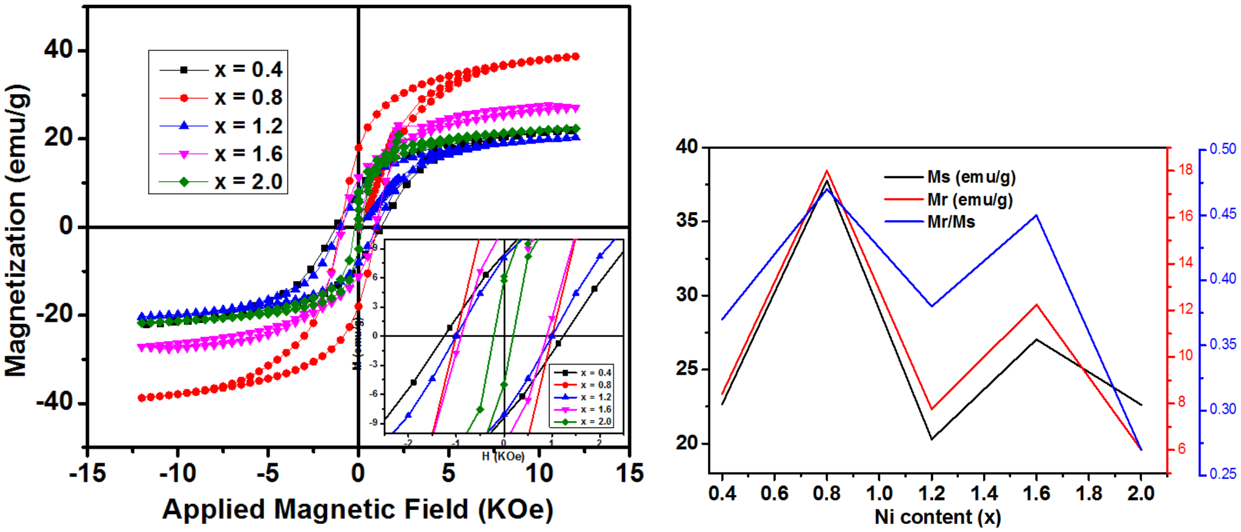

(a) (b)

FIG. 2. (a) Field Dependent magnetic properties and (b) variation of Mr, Ms and Mr/Ms for of $BaCo_{2-x}Ni_xFe_{16}O_{27}$ ($x = 0.4, 0.8, 1.2, 1.6, 2.0$) hexaferrite samples, prepared using a simple heat treatment method and calcinated at 650 °C for 3 hours

to be low in prepared samples compared to other doped barium hexagonal ferrites [8, 16]. The lower values of saturation magnetization and coercivity may be due to many reasons; surface effects, particle size and morphology, crystallographic defects, site occupancy of substituted ions in hexagonal lattice, phase impurity [17].

The ratio R of the remanence to the saturation magnetization (Mr/Ms) indicates the domain structure of prepared samples. A Mr/Ms value of ~ 0.5 is indicative of single domain and the lower value is associated with a multidomain structure [18]. In the present case, samples $x = 0.4$, 1.2, 2.0 show $R < 0.5$, indicating the formation of a multidomain structure, while samples $x = 0.8$ and 1.6 exhibited $R \cong 0.5$ confirming the formation of crystalline single domain structure. The hysteresis loops of $x = 0.4$ to 1.8 samples possessed hard magnetic character while the $x = 2.0$ sample showed soft ferrite behavior.

4. Conclusions

Nickel-doped barium cobalt hexagonal ferrites-$BaCo_{2-x}Ni_xFe_{16}O_{27}$ (x = 0.4, 0.8, 1.2, 1.6 and 2.0) were synthesized using a simple heat treatment method. X-ray diffraction analysis confirmed the formation of mixed phases of M, W (both hexaganal) and S (spinel). There was little change in the values of the lattice constants- a and c with addition of nickel in prepared barium cobalt hexaferrite powder. $BaNi_2Fe_{16}O_{27}$ hexaferrite exhibits soft ferrite nature, while other nickel substitutes barium cobalt ferrites show hard ferrite behavior.

Acknowledgements

One of the authors (Chetna C. Chauhan) acknowledge the funding support from Gujarat Council of Science and Technology (GUJCOST/MRP/2014-15/432, dated 30/06/2014) Gandhinagar. The work is also supported by DRS-SAP-Phase-I program of UGC (F.530/10/DRS/2010 (SAP-I)), New Delhi, India.

References

[1] Pullar R.C. Hexagonal Ferrites: A review of the synthesis, properties and applications of hexaferrite ceramics. *Prog. Mater Sci.*, 2012, **57**, P. 1191–1334.

[2] Vincent H., Sugg B., et al. Crystal growth, X-ray and magnetic studies of planar anisotropy M hexaferrites $BaFe_{12-2x}Ir_xMe_xO_{19}$ (Me=Zn, Co). *J. Mag. Mag. Mat.*, 1991, **101** (1-3), P. 170–172.

[3] Mendoza-Suarez G., Rivas-Vazquez L.P., et al. Magnetic properties and microstructure of $BaFe_{116-2x}Ti_xM_xO_{19}$ (M=Co, Zn, Sn) compounds. *Physica B: Cond. Mat.*, 2003, **339** (2), P. 110–118.

[4] El-Saadawy M. Thermal conductivity and thermoelectric power of the $Zn_{2-x}Co_xBaFe_{16}O_{27}$ hexagonal ferrites system. *Mater. Lett.*, 1999, **39**, P. 149–152.

[5] Campbell P. *Permanent Magnet Materials and Their Application*. Cambridge University Press, Cambridge, 1994.

[6] Ong C.K., Fang H.C., Yang Z., Li Y. Magnetic relaxation in Zn-Sn-doped barium ferrite nanoparticles for recording. *J. Mag. Mag. Mat.*, 2000, **213**, P. 413–417.

[7] Wang L.X., Song J., et al. The microwave magnetic performance of Sm^{3+} doped $BaCo_2Fe_{16}O_{27}$. *J. Alloys Compd.*, 2009, **481**, P. 863–866.

[8] Huang K., Liu X., et al. Structural and magnetic properties of Ca-substituted barium W-type hexagonal hexaferrites. *J. Mag. Mag. Mat.*, 2015, **379**, P. 16–21.

[9] Pawar R.A., Desai S.S., et al. Ce^{3+} incorporated structural and magnetic properties of M type barium hexaferrites. *J. Mag. Mag. Mat.*, 2015, **378**, P. 59–63.

[10] Iqbal M.J., Khan R.A. Enhancement of electrical and dielectric properties of Cr doped $BaZn_2$ W-type hexaferrite for potential applications in high frequency devices. *J. Alloys Compd.*, 2009, **478**, P. 847–852.

[11] Jotania R.B., Chauhan C.C., Menon S.K., Kulkarni B.D. Synthesis and magnetic properties of barium?calcium hexaferrite particles prepared by sol-gel and microemulsion techniques. *J. Mag. Mag. Mat.*, 2008, **320**, P. 1095–1101.

[12] Chauhan C.C., Jotania R.B. Microstructual, Thermal and Magnetic proeprties of cobalt doped barium calcium hexaferrite prepared by a sol gle route. *Int. J. Adv. Eng. Tech (IJAET)*, 2012, **3** (2), P. 135–139.

[13] Smith J., Wijn H.P.J. *Ferrites.* Philips, Technical Library, Eindhoven, 1959.

[14] Lotgering F.K., Vromans P.H.G. Chemical instability of metal deficient hexagonal ferrite with W structure. *J. Am. Ceram. Soc.*, 1977, **40**, P. 416–418.

[15] Mandal K., Mandal S.P., Agudo P., Pal M. A study of nanocrystalline (Mn?Zn) ferrite in SiO_2 matrix. *Appl. Surf. Sci.*, 2002, **182**, P. 386–389.

[16] Castro S., Gayoso M., et al. Structural and Magnetic properties of barium hexaferrite nanostructured materials prepared by the combustion method. *J. Magn. Magn. Mater*, 1996, **152**, P. 61–69.

[17] Battle X., Obradors X., et al. Surface spin canting in $BaFe_{12}O_{19}$ fine particles. *J. Magn. Magn. Mater.*, 1993, **124**, P. 228.

[18] Jiles J.C. Recent advances and future direction in magnetic materials. *Acta Materiala*, 2003, **51** (19), P. 5907–5939.

NANOSYSTEMS: PHYSICS, CHEMISTRY, MATHEMATICS, 2016, 7 (4), P. 599–603

Dielectric studies of nanocrystalline calcium tungstate

N. Aloysius[1]*, M. S. Rintu[2], E. M. Muhammed[2], T. Varghese[1,3]

[1]Department of Physics, Newman College Thodupuzha-685 585, Kerala, India
(Affiliated to M. G. University, Kottayam)
[2]Department of Physics, Maharajas College, Ernakulam-682 011, Kerala, India
[3]Nanoscience Research Centre (NSRC), Department of Physics, Nirmala College,
Muvattupuzha – 686 661, Kerala, India

*nanoncm@gmail.com

PACS 78.67.Bf, 81.16.Be, 73.63.-b **DOI 10.17586/2220-8054-2016-7-4-599-603**

Nanocrystalline samples of $CaWO_4$ were prepared at room temperature by simple chemical precipitation. The samples were characterized by X-ray diffraction and scanning electron microscopy. Energy dispersive X-ray analysis confirmed the elements present in the sample. The frequency and temperature dependence of the dielectric constant and ac electrical conductivity of the nanomaterial were investigated. Very low dielectric loss in nanocrystalline $CaWO_4$ powder was observed at high frequencies. The values of ac electrical conductivity calculated from the permittivity studies were found to increase as frequency increased, conforming to small polaron hopping.

Keywords: Chemical precipitation, dielectric constant, ac electrical conductivity, polaron hopping.

Received: 29 January 2016

Revised: 21 May 2016

1. Introduction

Nanocrystalline $CaWO_4$ has attracted particular interest because of its practical applications, such as laser host materials in quantum electronics and scintillators in medical devices [1–6]. It has been reported that $CaWO_4$ of scheelite-like structures is an excellent blue-emitting phosphor by their radiation of ultraviolet (UV) light [7]. Also, $CaWO_4$ has shown considerable promise as a fiber-matrix interlayer in oxide ceramic composites [8]. The lower dielectric constant and low loss make nanostructured $CaWO_4$ a promising candidate for applications as a low temperature co-fired ceramic (LTCC), substrate, and electronic packaging material [9]. Pullar et al. explained the microwave dielectric properties of AWO_4 (A = Mg, Zn, Ni and Co) compounds with extrinsic parameter, such as density [10]. Sreedevi et al. reported that Ag_2WO_4 nanoparticles can be a promising material for the high dielectric constant gate in Si-based complementary metal oxide semiconducting devices [11]. The influence of processing methods on the characteristics of $CdWO_4$ powders and the related microwave dielectric properties were reported by Bao-Chun Guo et al. [12]. The study of dielectric properties of samples as a function of temperature and frequency may help in identifying their potential applications [13]. The characterization of dielectric behavior is very important not only to the theory of the polarization mechanism but also from an application point of view, where knowledge of the temperature and the frequency dependence of dielectric constant are very important. The relative dielectric constant of the material determines its ability to store electrostatic energy.

Dielectric studies of $CaWO_4$ nanoparticles are incomplete and need further investigation. In the present work, we synthesized $CaWO_4$ nanoparticles by chemical precipitation followed by calcination. The samples were then characterized by X-ray diffraction (XRD) and scanning electron microscopy (SEM). The frequency and temperature dependence of dielectric properties of sintered pellets made out of the products were then investigated.

2. Materials and methods

Calcium nitrate $Ca(NO_3)_2{\cdot}4H_2O$ (99.8 %, Sigma Aldrich) and sodium tungstate $Na_2WO_4{\cdot}2H_2O$) (99.9 %, Alfa Aesar) analytical grade reagents were used for the preparation of $CaWO_4$ nanocrystals. The samples were prepared by reacting aqueous solutions of calcium nitrate and sodium tungstate (0.1 M each) at room temperature. The precipitate formed was centrifuged, filtered, washed with distilled water a number of times, and dried in an oven to get fine powders of calcium tungstate. S_1 and S_2 are samples of nanocrystalline $CaWO_4$ were calcined at 650 and 750 °C, respectively. XRD studies of these samples were conducted using Bruker D8 Advance X-ray diffractometer ($\lambda = 1.5406$ Å) with CuKα radiation in 2θ range from 20 to 80 °. The morphological analysis of $CaWO_4$ nanoparticles was carried out with a scanning electron microscope JEOL MODEL JSM-6390LV, operating at 20 kV measurements.

The calcined powder sample was cold pressed in the form of cylindrical pellets of diameter 13 mm and thickness $d \sim 1.5$ mm by applying a pressure of $\sim$ 10 GPa using a hand operated hydraulic press. The pellets were then sintered at 500 °C. The density of the pellet was determined to be 4.88 g/cm^3. The circular faces of the pellets were made electrically conducting by coating with silver paste. Dielectric measurements as a function of frequency in the range of 100 Hz – 1 MHz were measured at various selected temperatures from 303 – 423 K using an LCR meter (Wayne Kerr H-6500 model) in conjunction with a portable furnace and temperature controller ($\pm$1 K).

3. Results and discussion

The powder XRD spectra of $CaWO_4$ nanoparticle samples are shown in Fig. 1. Both the samples showed characteristic peaks of scheelite structure with tetragonal unit cell. The 'd' values taken from the JCPDS file No. 77-2235 for $CaWO_4$ are in close agreement with the observed 'd' values.

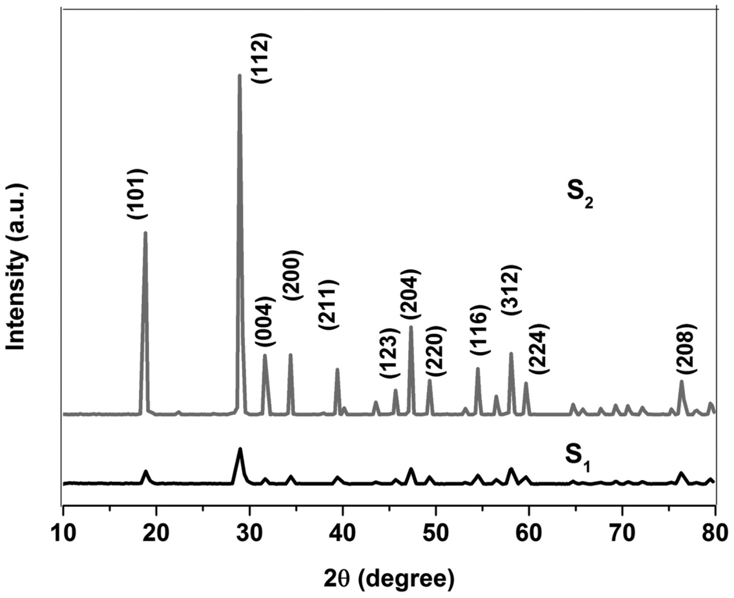

FIG. 1. XRD spectra of $CaWO_4$ samples

In general, the nanocrystallite size can be estimated from the Scherrer's formula: $D_{hkl} = K\lambda/(\beta\cos\theta)$, where λ is the x-ray wavelength (0.15405 nm), β the full-width at half maximum, θ the diffraction angle, K is a constant (0.89) and D_{hkl} the size along the (hkl) direction. From the analysis, the average crystallite size obtained was 39 nm for S_1 and 44 nm for S_2.

The SEM image of $CaWO_4$ nanoparticles calcined at 650 °C is shown in Fig. 2(a). They are clusters shaped like dumb-bells. The elemental analysis of the sample S_1 was done by energy dispersive X-ray (EDX) spectroscopy. Fig. 2(b) shows typical EDX spectrum of synthesized $CaWO_4$ nanoparticles. The peaks of the spectrum confirmed that the product contains Ca, W and O. The intense signal near at 1.774 keV indicates that W is the major element.

The dielectric constant and ac conductivity (σ_{ac}) were calculated by using equations $\varepsilon' = Cd/\varepsilon_0 A$ and $\sigma_{ac} = \varepsilon'\varepsilon_0\omega\tan\delta$, respectively, where A is the face area, C the measured capacitance of the pellet, ε_0 the permittivity of vacuum, ω the angular frequency and tan δ the loss tangent. Fig. 3(a) shows the variation of dielectric constant with frequency for temperatures from 303 to 423 K of sample S_1. It is seen that the dielectric constant for all temperatures are high at low frequencies which decreased rapidly as frequency increased, attaining a constant value at higher frequencies. For 303 K, the value of ε was 24.74 at 100 Hz, which decreased to 7.11 at 1 MHz. At 393 K, the values were 30.08 (100 Hz) and 7.15 (1.0 MHz). The corresponding values for 423 K were 39.54 at 100 Hz and 7.20 at 1.0 MHz. Fig. 3(b) shows a similar variation for samples S_1 and S_2, at 393 K. At lower frequencies the dielectric constant is found to be higher for the sample having smaller grain size (S_1), but approaches a constant value beyond 0.1 MHz. When temperature is increased, more and more dipoles are oriented, resulting in an increase in the dielectric constant for a given value of frequency [14]. At very high frequencies (MHz), the charge carriers would have started to move before the field reversal occurs and ε' falls to a small value at higher frequencies.

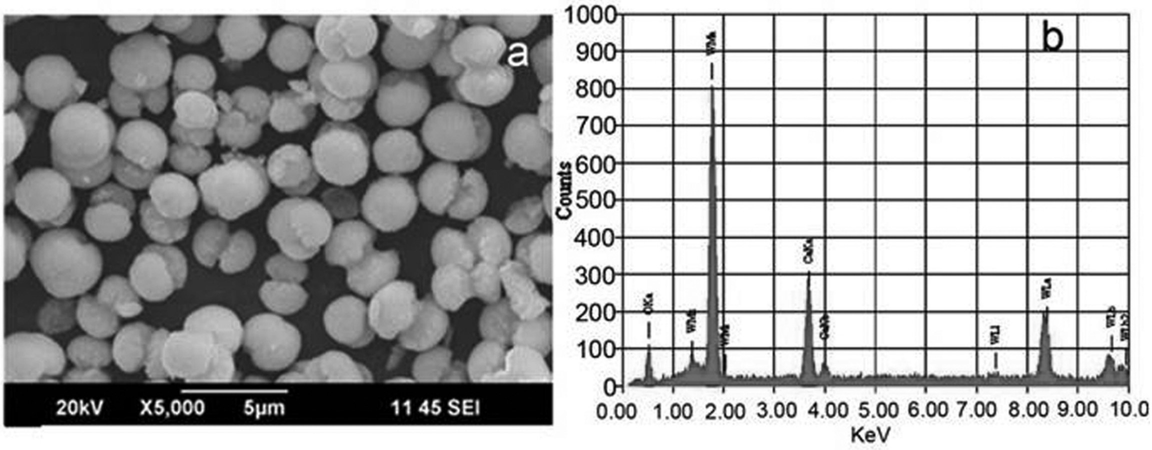

FIG. 2. (a) SEM image of $CaWO_4$ (S_1) and (b) EDX spectrum of $CaWO_4$

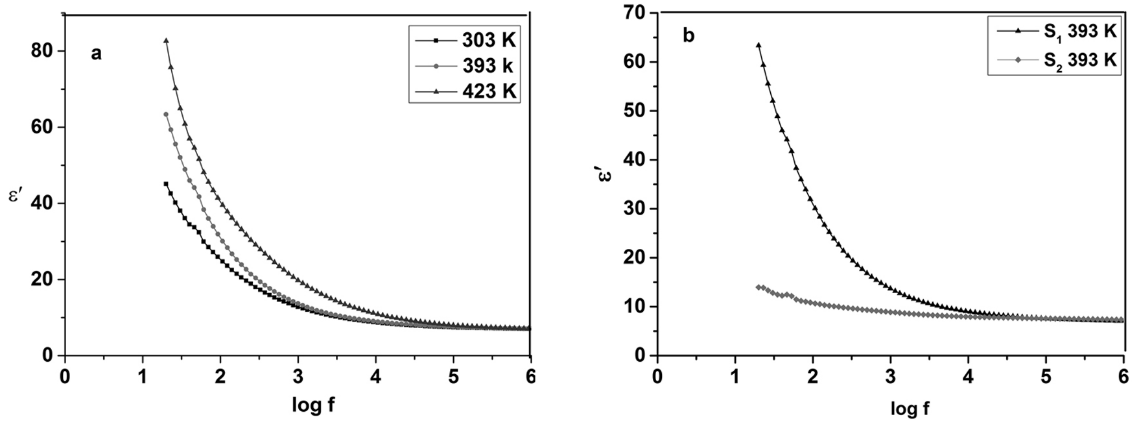

FIG. 3. The variation of dielectric constant with frequency of (a) sample S_1 at temperatures 303, 393 and 423 K and (b) samples S_1 and S_2 at 393 K

Space charge polarization and reversal of the polarization direction contributes much to the ε' [15]. With the increase in volume of the particle, the volume of the interfaces decreases. When volume increases, the contribution to ε' by electronic relaxation polarization inside the particles increases.

The frequency dependence of dielectric loss of sample S_1 is shown in Fig. 4(a). The loss factor represented by $\tan\delta$ has a value of 3.26 at 100 Hz which decreases slowly to zero at higher frequencies. At 393 K, the corresponding variation is not very different. For 423 K, $\tan\delta$ has a value of 9.53 at 100 Hz which gradually decreases almost to 0 at frequencies beyond 0.10 MHz. At 393 K the corresponding variation is not very different. The decrease in $\tan\delta$ takes place when the jumping rate of charge carriers lags behind the alternating electric field beyond a certain critical frequency.The inhomogeneities present in the interface layers in $CaWO_4$ nanocrystals produce an absorption current resulting in dielectric loss. This absorption current decreases with increase in frequency of the applied field. The hopping probability per unit time increases with increase in temperature. Correspondingly, the loss tangent also increases with increase of temperature [16]. The variation of $\tan\delta$ with frequency at 393 K for samples S_1 and S_2 with different grain sizes is shown in Fig. 4(b). At 100 Hz, the value is 3.4 for S_1 which decreases to 0.9 for S_2. This variation of $\tan\delta$ for different grain sizes is due to size effect [17]. The low value of $\tan\delta$ indicates its potential for microwave applications.

The loss in $CaWO_4$ can be explained using the electronic hopping model, which considers the frequency dependence of the localized charge carriers hopping in a random array. This model is applicable for materials in which the polarization responds rapidly to the appearance of an electron on any one site so that the transition may be said to occur effectively into the final state [17]. In the high frequency region $\tan\delta$ becomes almost zero because the electron exchange interaction (hopping) cannot follow the alternatives of the applied ac electric field beyond a critical frequency.

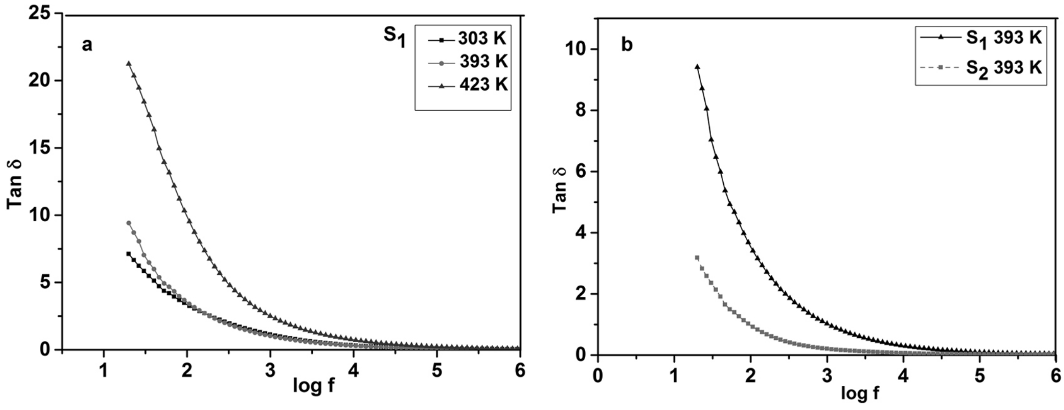

FIG. 4. The variation of loss tangent with frequency of (a) sample S_1 at temperatures 303, 393 and 423 K and (b) samples S_1 and S_2 at 393 K

Figure 5(a) shows the variation of ac conductivity (σ_{ac}) of sample S1with frequency. Initially, it has a small value which increased at higher frequencies. The nature of variation is similar for other temperatures, but the values are shifted upwards as the temperature is raised. For 303 K, σ_{ac} has a value of 5.001×10^{-7} S/m at 100 Hz which increased slowly at higher frequencies to 1.4×10^{-3} S/m at 0.10 MHz. At 393 K, the corresponding variation was not very different. For 423 K, the values were 2.236×10^{-6} S/m at 100 Hz and 2.781×10^{-5} S/m at 1.0 MHz. The variation of σ_{ac} with frequency at 393K for different grain sizes is shown in Fig. 5(b). At 100 Hz, σ_{ac} is found to be 5.002×10^{-7} S/m for S_1 which increased to 6.88×10^{-5} S/m at 1.0 MHz. For S_2, the corresponding values were 5.823×10^{-8} S/m and 7.671×10^{-6} S/m. It is clear from the figure that the conductivity increased as frequency increased conforming to small polaron hopping [18]. Also, there is a possibility of conduction due to impurities at low temperature. It is found that at given temperature and frequency, σ_{ac} is higher for particle having smaller size. According to Elliot's barrier hopping model, ac conductivity increases with hopping distance [19]. Therefore, it may be concluded that in $CaWO_4$ hopping distance increased with reduction in particle size.

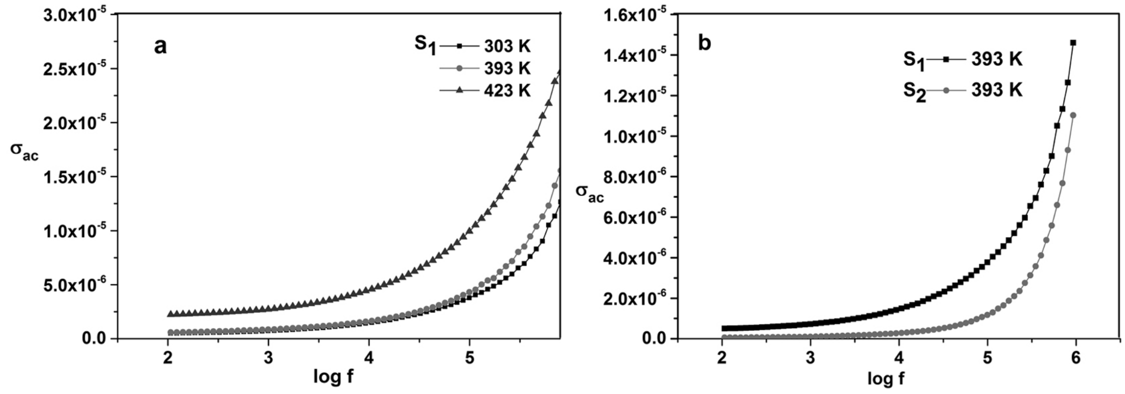

FIG. 5. The variation of ac electrical conductivity with frequency of (a) sample S_1 at temperatures 303, 393 and 423 K; (b) samples S_1 and S_2 at 393 K

4. Conclusion

The $CaWO_4$ nanoparticles were prepared at room temperature by simple chemical precipitation reaction without any catalyst, surfactant, or templates. The dielectric properties of $CaWO_4$ were determined as a function of frequency from 100 Hz to 1.0 MHz for temperatures ranging from 303 to 423 K. At lower frequencies, ε' and $\tan\delta$ have higher values while at higher frequencies the values reached steady lower values. Similar variation was observed when the temperature was raised but the values of ε' and $\tan\delta$ were elevated. The ac conductivity increased as frequency was increased conforming to small polaron hopping. The values of ε', $\tan\delta$ and σ_{ac} showed considerable increase as the particle size was reduced. The very low value of loss tangent obtained for

$CaWO_4$ nanocrystals suggests that it is potentially useful for microwave applications. It was found that the applied frequency, temperature and particles size affect the dielectric properties of the $CaWO_4$ nanocrystals.

Acknowledgements

The authors are indebted to NSRC, Nirmala College, Muvattupuzha and Newman College, Thodupuzha for the support to undertake this study. The financial support from the University Grants Commission, New Delhi, India (FIP/12th Plan/KLMG020 TF03) is greatly acknowledged.

References

[1] Kobayashi M., Ishii M., Usuki Y., Yahagi H. Scintillation characteristics of PbWO4 single crystals at room temperature. *Nuclear Instruments and Methods in Physics Research A*, 1993, **333** (2-3), P. 429–433.

[2] Katelnikovas A., Grigorjeva L., et al. Sol-Gel Preparation of Nanocrystalline $CaWO_4$. *Lithuanian J. of Physics*, 2007, **47** (1), P. 63–68.

[3] Phuruangrat A., Thongtem T., Thongtem S. Synthesis, characterization and photoluminescence of nanocrystalline calcium tungstate. *J. Exp. Nanosci.*, 2009, **5**, P. 263–267.

[4] Lou Z., Cocivera M. Cathodoluminescence of $CaWO_4$ and SrWO4 thin films prepared by spray pyrolysis. *Mater. Res. Bull.*, 2002, **37**, P. 1573–1582.

[5] Nagirnyi V., Feldbach E., et al. Excitonic and recombination processes in $CaWO_4$ and $CdWO_4$ scintillators under synchrotron irradiation. *Radiat. Meas.*, 1998, **29**, P. 247–250.

[6] Oishi S., Hirao M. Growth of $CaWO_4$ whiskers from KCl flux. *J.Mater.Sci., Lett.*, 1989, **8** (12), P. 1397–1398.

[7] Liping L., Yiguo S., Guangshe L. Size-induced symmetric enhancement and its relevance to scheelite $CaWO_4$ nanocrystals. *J. Appl. Phys. Lett.*, 2007, **90**, P. 054105–054107.

[8] Mogilevsky P., Parthasarathy T.A., Petry M.D. Anisotropy in room temperature microhardness and fracture of $CaWO_4$ scheelite. *Acta Materialia*, 2004, **52**, P. 5529–5537.

[9] Vidya S., Sam Solomon., Thomas J.K. Synthesis of Nanocrystalline $CaWO_4$ as Low-Temperature Co-Fired Ceramic Material: Processing, Structural and Physical Properties. *Journal of Electronic Materials*, 2012, **42**, P. 129–137.

[10] Pullar R.C., Farrah S., Alford N.M. $MgWO_4$, $ZnWO_4$, $NiWO_4$ and $CoWO_4$ microwave dielectric ceramics. *Journal of the European Ceramic Society*, 2007, **27**, P. 1059–1063.

[11] Sreedevi A., Priyanka K.P., et al. Nanophase α-Silver Tungstate for Potential Applications in Light Emitting Diodes and Gate Dielectrics. *Advanced Science, Engineering and Medicine*, 2015, **7**, P. 498–505.

[12] Bao-Chun Guo, Peng Liu, et al. Effect of Preparation Methods on Microstructures and Microwave Dielectric Properties of $CdWO_4$ ceramics. *Integrated Ferroelectrics*, 2015, **167**, P. 107–114.

[13] Chi Kao K. *Dielectric phenomena in Solids*. Elsevier, New York, 2004.

[14] Kar T., Choudhary R.N., Sharma S., Singh K.S. Structural and electrical properties of $Ba_2Na_3RNb_{10}O_{30}$ Ceramics. *Indian J. Phys. A*, 1999, **73** (4), P. 453-459.

[15] Ravinder D., Vijayakumar K. Dielectric behaviour of erbium substituted Mn–Zn ferrites. *Bull. Mater. Sci.*, 2001, **24** (5), P. 505–509.

[16] Potty S.N., Khader M.A. Dielectric Properties of nanophase Ag_2HgI_4 and Ag_2HgI_4–Al_2O_3 nanocomposites. *Bull. Mater. Sci.*, 2000, **23** (5), P. 361–367.

[17] Murthy V., Sobhanadri J. Dielectric properties of some nickel-zinc ferrites at radio frequency. *Phys Status Solidi (a)*, 1976, **36** (2), K133–K135.

[18] Priyanka K.P., Sunny J., et al. Dielectric properties and a. c. conductivity of nanocrystalline titania. *J. Basic Appl. Phys.*, 2013, **2**, P. 105–108.

[19] Elliot S.R. Temperature dependence of a.c. conductivity of chalcogenide glasses. *Phil. Mag. Part B*, 1978, **37** (5), P. 553.

NANOSYSTEMS: PHYSICS, CHEMISTRY, MATHEMATICS, 2016, 7 (4), P. 604–608

Dynamic study of bismuth telluride quantum dot assisted titanium oxide for efficient photoelectrochemical performance

Pallavi B. Patil, Vijay V. Kondalkar, Kishorkumar V. Khot, Chaitali S. Bagade, Rahul M. Mane, P. N. Bhosale*

Materials Research Laboratory, Department of Chemistry, Shivaji University, Kolhapur–416004, India

*p_n_bhosale@rediffmail.com

PACS 82.45 Mp **DOI 10.17586/2220-8054-2016-7-4-604-608**

The 3D TiO_2 microflowers, sensitized by Bi_2Te_3 nanoparticles, having novel architecture were generated employing a two-step synthetic strategy, including a hydrothermal process and a potentiostatic electrodeposition technique. The design and synthesis of quantum dots (QDs) for achieving high photoelectrochemical performance is an urgent need for high technology fields

Keywords: Bi_2Te_3 QDs assisted TiO_2, 1D nanorods, PEC.

Received: 30 January 2016

Revised: 6 May 2016

1. Introduction

Quantum dot-sensitized solar cells (QDSCs) have received much attention because they are promising candidates for low cost and large area photovoltaic applications. Semiconductor quantum dot-sensitized solar cells (QDSSCs) have the advantages of being low cost and a simple fabrication process. The most attractive property of a semiconductor quantum dot is its ability to promote the photoconversion efficiency above Shockley-Queisser limit. The low efficiency of QDSSCs is attributed to the relatively low photovoltage in the cell compared to DSSCs and to the recombination paths induced by the electronic properties of the interfaces formed at TiO_2-QD-electrolyte triple junction [1]. Secondly, it is difficult to incorporate QDs into a TiO_2 mesoporous matrix to obtain a well-covered QD monolayer on the inner surface of the TiO_2 electrode. Other possible reasons include QD-electrolyte interfaces [2], electron loss occurring through charge recombination at the TiO_2-electrolyte interface [3]. To achieve higher performance photovoltaic solar cells, morphologies and structures of anode materials are also widely investigated [4]. In general, mesoporous TiO_2 nanoparticles are the most frequently used photoanodes in DSSCs and QDSSCs, due to their high internal surface area for sufficient sensitizer anchoring [5]. Unfortunately, mesoporous TiO_2 nanoparticles have some disadvantages, such as charge collection rate due to surface states and grain boundaries existing in the pathway of nanoparticles, which can lead to many unexpected trapping and de-trapping, and thus, inferior light scattering [6]. In this study, we successfully synthesized vertically aligned TiO_2 nanorods sensitized by Bi_2Te_3 nanoparticles. The photoelectrochemical performance of TiO_2 is greatly improved by sensitization of TiO_2 by Bi_2Te_3 nanoparticles [7]. The sensitization of TiO_2 by Bi_2Te_3 nanoparticles leads to a separation of the charge carriers. The charge separation leads to a reduction in the overall recombination in the solar cells and the enhancement of photogenerated carrier collection.

2. Method

First, TiO_2 can be prepared by our previously-reported hydrothermal method [7]. In detail 0.04 M TTIP was added in the solution containing 3M HCl and ethylene glycol stirred for some time. The clear transparent solution then poured into a Teflon-lined stainless steel autoclave maintained at 160°C for 2 h. The electrodeposition of Bi_2Te_3 nanoparticles on TiO_2 thin films was accomplished in a three electrode cell configuration containing aqueous solutions of 7 mM Bi $(NO_3)_3$ and 10 mM Te in 1M HNO_3. The deposition was carried out at -0.8 V vs Ag/AgCl. In this, TiO_2 nanorods act as working electrode, platinum as counter electrode and Ag/AgCl as reference electrode. The deposition time was fixed at 30 min. and the depositions were carried out at room temperature. In order to control the size of Bi_2Te_3 nanoparticles and prevent large particle formation, PVA was used as structure directing agent.

3. Results and discussion

3.1. Optical absorption spectra of Bi_2T_3 loaded TiO_2

The light absorption properties of Bi_2Te_3-loaded TiO_2 thin was evaluated using the UV-visible spectrophotometer (Shimadzu UV-1800 Japan). Figure 1 shows the Tauc plot of Bi_2Te_3 loaded TiO_2 thin films. The band gap energy of composite can be expressed by the Tauc relation. It is well known that there are fundamental optical transitions, namely directly-allowed (n=1/2) and indirectly-allowed (n=2) transition. It is also noteworthy that the band gap energy of Bi_2Te_3 loaded TiO_2 heterostructures was found to be 2.1 eV, indicating the optical absorption of the hybrid nanostructure has been extended from the UV region to the visible region.

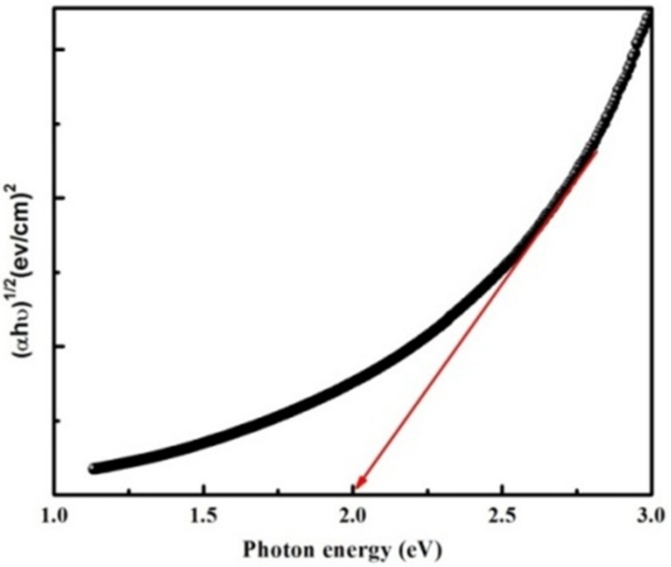

FIG. 1. Optical absorption spectra of Bi_2Te_3 loaded TiO_2 thin film

3.2. X-ray diffraction (XRD) pattern of Bi_2T_3 loaded TiO_2 thin film

The strong characteristic diffraction peak appeared at around 27.70° corresponds to (110) peak associated with rutile phase of TiO_2 (Space Group: P42/ mnm, JCPDS: 00-001-0562) (Rigaku, D/MAX Ultima III XRD spectrometer (Japan)). Furthermore, it should be noted that diffraction peak appearing at 27.67° corresponds to the (015) plane of Rhombohedral Bi_2Te_3 (JCPDS: 15-0863 space group R-3m) shown in Fig. 2. Due to overlap between (110) plane of TiO_2 and (015) plane of Bi_2Te_3, it is difficult to distinguish these two peaks in the XRD pattern. While the other peaks appeared at 2θ 27.70°, 36.22°, 41.35°, 54.58°, 56.97° and 65.54°, corresponding to the (110), (101), (111), (211), (220) and (221) crystal plane of tetragonal TiO_2 and 27.67°, 37.86°, 62.91° and 69.91° corresponding to the (015), (1010), (0213) and (0216) crystal planes of rhombohedral Bi_2Te_3.

It was found that the diffraction peak of the resulting deposit confirms the successful loading of Bi_2Te_3 nanoparticles on TiO_2. The crystallite size of the material was calculated by using Debye Scherrer formula, given in equation 1:

$$D = \frac{0.94\lambda}{\beta\cos\theta}, \tag{1}$$

where D is crystallite size, θ is Peak position of X-ray diffraction, β is Full Width at Half Maxima (FWHM) in radian, λ is Wavelength of X-ray used (0.154 nm). The XRD parameters are summarized in Table 1.

TABLE 1. XRD parameters.

Sample	Crystallite Size (D) (nm)	Microstrain(ε) 10^{-3} (lines m^{-2})	Dislocation density (δ)$\times10^{-3}$ (lines^{-2} m^{-4})
Bi_2Te_3 loaded TiO_2	16.78	20156	3.5515

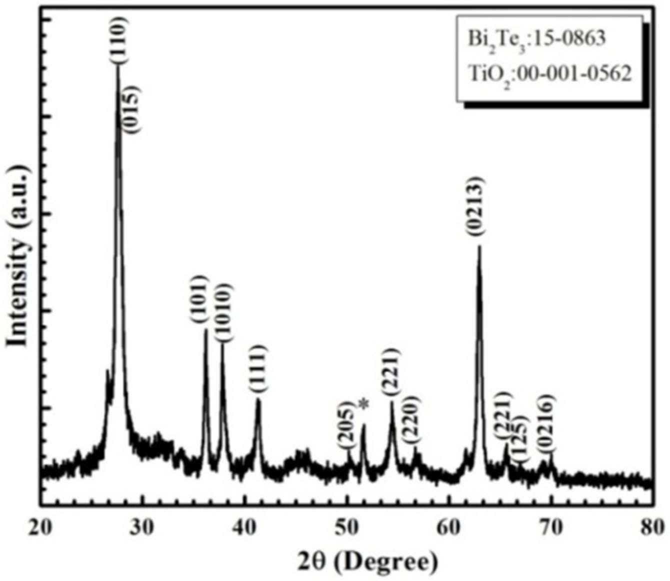

FIG. 2. X-ray diffraction pattern of Bi_2Te_3 loaded TiO_2 thin film

3.3. Field Emission Scanning Electron Microscopy (FESEM) of Bi_2T_3 loaded TiO_2 thin film

The morphological analysis of the synthesized material was carried out using field emission scanning electron microscopy (FESEM) (Hitachi, S-4700). Fig. 3 shows the low and high magnification field emission scanning electron microscopy (FESEM) images. The FESEM image shows that entire surface of FTO substrate is covered with well-aligned TiO_2 nanorods coated with Bi_2Te_3 nanoparticles. From the higher magnification of such nanorod arrays, the average diameter of the TiO_2 nanorod is 95–110 nm.

After Bi_2Te_3 quantum dot loading, the TiO_2 nanorods become rough, which means that the QDs have been successfully deposited on the surface of the TiO_2 nanorods after potentiostatic electrodeposition. The vertical alignment of the TiO_2 nanorods is beneficial for the improvement in the charge transfer of the solar cells. Such deep penetration of Bi_2Te_3 nanoparticles into the TiO_2 nanorods improves the charge separation and reduces recombination rate, which is beneficial for the photoelectrochemical performance of the solar cell.

3.4. Compositional analysis Bi_2Te_3 loaded TiO_2 thin film

Qualitative and quantitative analysis of the prepared Bi_2Te_3 loaded TiO_2 was carried out using energy dispersive X-ray spectroscopy (EDS).

The EDS spectrum confirms the presence of titanium, oxygen, bismuth and tellurium in prepared Bi_2Te_3 loaded TiO_2 thin film. From Figure 4, it is readily seen that the peaks at 4.5, 0.5, 2.4 and 3.7 keV confirm the presence of Ti, O, Bi and Te respectively in the Bi_2Te_3-loaded TiO_2 film.

3.5. Photoelectrochemical performance (PEC)

The typical J-V characteristic curve of Bi_2Te_3-loaded TiO_2 thin film was determined. The photoelectrochemical performance of the Bi_2Te_3-loaded TiO_2 thin film was carried out using a two electrode cell configuration (AUTOLAB PGSTAT100 FRA 32 potentiostat). In order to evaluate the photoelectrochemical performance, the Bi_2Te_3-loaded TiO_2 thin film acts as a photoanode, graphite as counter electrode with 0.5 polysulfide electrolyte. The cell configuration is as follows: Glass/ FTO/ Bi_2Te_3 loaded TiO_2/ 0.5M Polysulphide/G .

The photoelectrochemical performance i.e. fill factor (FF) and overall light to electric energy conversion efficiency (%) was calculated by equation (2) and (3):

$$FF = \frac{V_{max}J_{max}}{V_{oc}J_{sc}} \tag{2}$$

$$\eta\% = \frac{V_{oc}J_{sc}}{P_{in} \times FF \times 100,} \tag{3}$$

where V_{oc} is open circuit voltage, J_{sc} is short circuit current, V_{max} is maximum voltage, J_{max} is maximum current, FF is the fill factor and P_{in} is the intensity of the incident light.

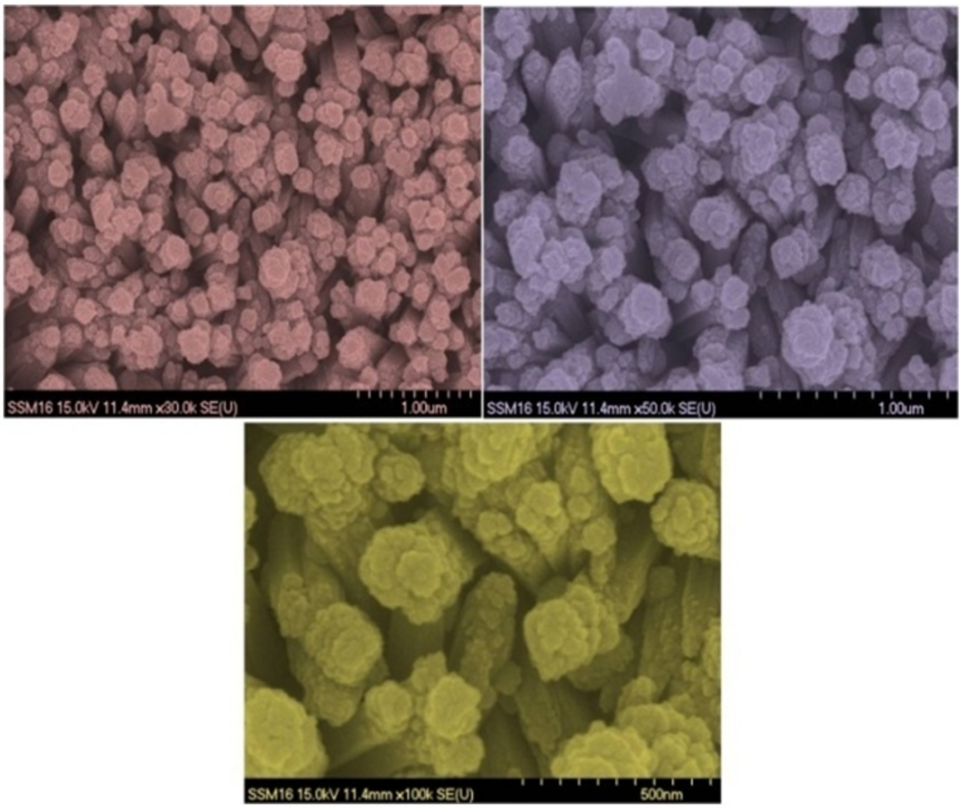

FIG. 3. Field emission scanning electron microscopy images of Bi_2Te_3 loaded TiO_2 thin film

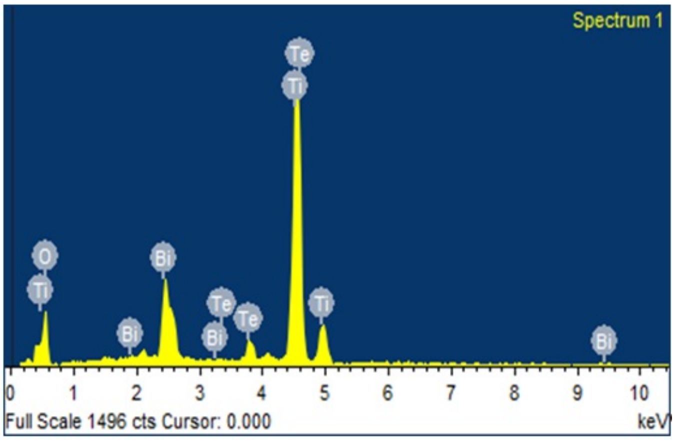

FIG. 4. EDS spectrum of Bi_2Te_3 loaded TiO_2 thin film

The detailed photovoltaic parameters are summarized in Table 2. The Bi_2Te_3-loaded TiO_2 thin film shows 0.026% photoconversion efficiency.

TABLE 2. Photoelectrochemical solar cell parameters of Bi_2Te_3 loaded TiO_2 thin film

Electrode	V_{oc} (mV)	J_{sc} (μA/cm^2)	R_s (Ω)	R_{sh} (Ω)	η%
Bi_2Te_3 loaded TiO_2	397.03	61	2660	4762	0.026

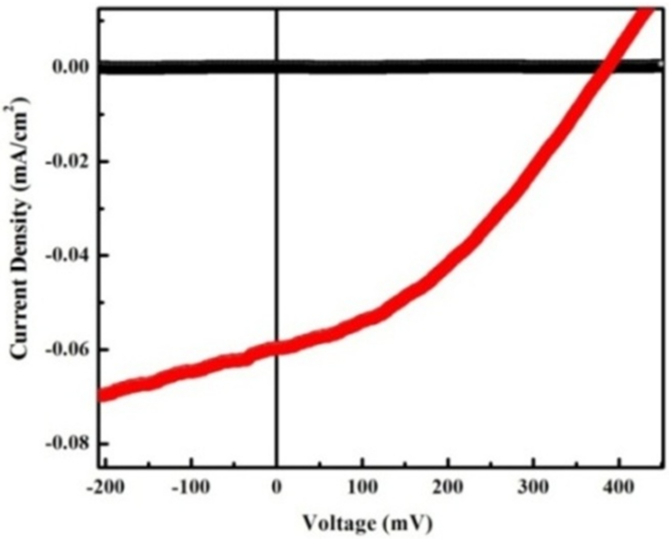

FIG. 5. J-V characteristic curve of Bi_2Te_3 loaded TiO_2 thin film

4. Conclusion

In summary, a Bi_2Te_3-loaded TiO_2 thin film was successfully prepared by a two-step synthetic strategy. 1D nanorods provided a unidirectional transport path for efficient charge, leading to high photoelectrochemical performance. Therefore, this novel combinatorial Bi_2Te_3 loaded TiO_2 thin film shows 0.026% photoconversion efficiency.

References

[1] Sero I., Gimenez S., Santiago F., Gomez R, Shen Q., Toyoda T., Bisquert J. Recombination in Quantum Dot Sensitized Solar Cells, *Acc. Chem. Res.*, 2009, **42**, P. 1848–1857.

[2] Diguna L., Murakami M., Sato A., Kumagai Y., Ishihara T., Kobayashi N., Shen Q., Toyoda T. Highly efficient CdS/CdSe-sensitized solar cells controlled by the structural properties of compact porous TiO_2 photoelectrodes. *J. Appl. Phys.*, 2008, **103**, P. 084304–084308.

[3] Lee Y., Chang C. Efficient polysulfide electrolyte for CdS quantum dot-sensitized solar cells. *J. Power Sources*, 2008, **185**, P. 584–588.

[4] Wu W., Xu Y., Su C., Kuang D. Ultra-long anatase TiO_2 nanowire arrays with multi-layered configuration on FTO glass for high-efficiency dye-sensitized solar cells. *Energy Environ. Sci.*, 2014, **7**, P. 644–649.

[5] Shiu J., Lan C., Chang Y., Wu H., Huang W., Diau Eric W. Size-Controlled Anatase Titania Single Crystals with Octahedron-like Morphology for Dye-Sensitized Solar Cells. *ACS Nano*, 2012, **6**, P. 10862–10873.

[6] Du J., Qi J., Wang D., Tang Z., Facile synthesis of Au@TiO_2 core-shell hollow spheres for dye-sensitized solar cells with remarkably improved efficiency. *Energy Environ. Sci.*, 2012, **5**, P. 6914–6918.

[7] Patil P., Mali S., Kondalkar V., Mane R., Patil P., Hong C., Bhosale P. Bismuth Telluride quantum dot assisted Titanium Oxide microflowers for efficient photoelectrochemical performance. *Mater. Lett.*, 2015, **159**, P. 177–181.

[8] Patil P., Mali S., Kondalkar V., Pawar N., Khot K., Hong C., Patil P., Bhosale P. Single step hydrothermal synthesis of hierarchical TiO_2 microflowers with radially assembled nanorods for enhanced photovoltaic performance. *RSC Adv.*, 2014, **4**, P. 47278–47286.

NANOSYSTEMS: PHYSICS, CHEMISTRY, MATHEMATICS, 2016, 7 (4), P. 609–612

Investigations on cycle time reduction, dynamic mechanical properties and creep for rotationally moldable nano composites of linear low density polyethylene and fumed silica

V. G. Chandran, S. D. Waigaonkar

BITS Pilani K.K. Birla Goa Campus, Department of Mechanical Engineering, NH-17B, Zuari Nagar, Goa, India, 403726

p2011407@goa.bits-pilani.ac.in, sdw@goa.bits-pilani.ac.in

PACS 81.05.Lg **DOI 10.17586/2220-8054-2016-7-4-609-612**

Composites of rotationally-moldable linear low density polyethylene (LLDPE) are becoming increasingly popular for rotational molding. In this study, the influence of fumed silica (FS) in pulling force requirement for demolding of rotationally moldable LLDPE is investigated. The dynamic mechanical analysis and creep studies were also performed to ascertain the reinforcement effects of FS in LLDPE matrix.

Keywords: LLDPE, FS, rotational molding.

Received: 31 January 2016

Revised: 9 June 2016

1. Introduction

The use of nanoparticles in rotational molding to enhance the melt characteristics and mechanical properties are increasing due to the limited choices of currently-available polymeric materials [1, 2]. Linear low density polyethylene (LLDPE) is the most commonly-used polymer for rotational molding. Normally, micro scale additives like anti oxidants, fillers, UV stabilisers, etc., are blended with LLDPE and pulverized to fine powder before molding to obtain the desired products. These additives are generally not nano-scale particles, and hence, do not provide reinforcement to polymer chains. Even though these additives provide desired properties, like UV resistance, reduced product cost, thermal stability, etc, they may adversely affect the mechanical properties [3]. The improvements in mechanical properties, such as tensile strength, impact toughness, creep, stress relaxation, etc. were reported with addition of nano fillers like, organo clays [4], metal nanoparticles [5], titanium oxide [6], zinc oxide [7], calcium carbonate [8] and silica nanoparticles in a polymer matrix [9]. Along with the improvements in mechanical properties, cycle time reduction for the molding process is also highly desired.

From our previous studies, it was observed that the nano-composites of LLDPE-FS up to 4 wt% FS provided acceptable melt flow characteristics for rotational molding [10]. In this study, nanoparticles of silica up to 4 wt% in the form of fumed silica (FS) having primary particle size in the range of 5–50 nm was dry mixed with LLDPE using a high speed mixer and was melt blended and pulverized in a commercial melt extruder and pulverizer. These blends (LLDPE-4%FS) were rotationally molded in a bi-axial rotational molding machine for studying the dynamic mechanical properties and cycle time. A unique fixture was made to study the mold release force at various temperatures and rates of pulling. The effect on maximum pulling force on commonly used mold materials, aluminum (grade 2024) and mild steel (grade S275), were studied with various LLDPE-FS blends. The PIAT (Peak internal air temperature) during rotational molding was studied using a Templogger, which records and transmits temperature readings wirelessly. The dynamic mechanical properties and viscoelastic creep was studied using DMA Q800 from TA instruments.

2. Results and discussion

The influence of FS nano particles, on the dynamic mechanical properties (DMA) viz. storage modulus (E’), loss modulus (E”) and tan delta are given in Fig. 1. With the addition of FS (4%), an increase of 20% in storage modulus is observed at room temperature (30°C), while the loss modulus recorded an increase of 15%. The increasing trend of storage modulus and loss modulus is observed at all temperatures. Two distinct peaks are observed in the loss modulus curve, representing the glass transition temperatures (T_g). The first peak at -127°C represents the 'γ' T_g, which corresponds to small scale movements in polymer chains usually associated with inter- and intramolecular motions. The second peak at 46°C represents 'α' T_g , which corresponds to the onset of melting of low molecular weight polymer chains. The peak at -17°C in the loss modulus is analogus to the 'β' T_g observed in low density polyethylene (LDPE). Generally, the β transition is not observed in LLDPE. However, due to the presence of fumed silica, the amorphous nature is increased in LLDPE, leading to entanglement of polymer chains [11]. The relaxation in polymer chains due to bending and twisting with the presence of FS, analogous to long side branches of LDPE, may be responsible for the presence of this β glass transition. At 4% FS, the concentration the shifts for 'α', 'β' and 'γ' T_g were not significant as compared to natural LLDPE.

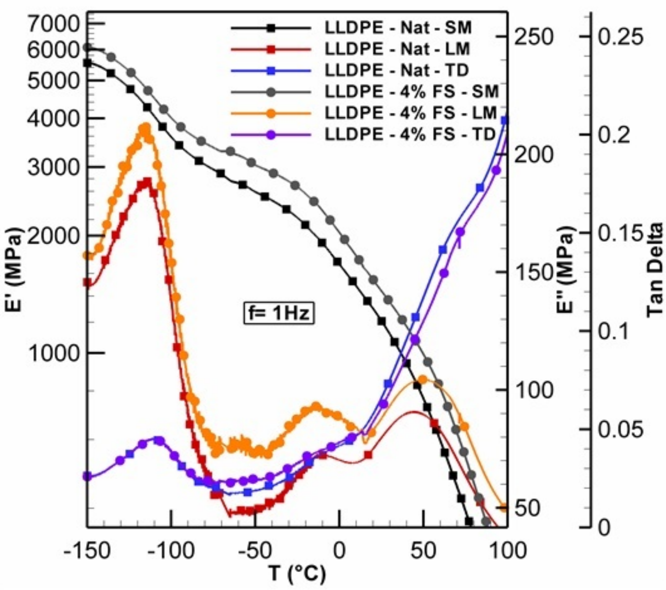

FIG. 1. Visco-elastic properties of LLDPE and LLDPE-4% FS blends

The proper dispersion of FS in LLDPE is required to achieve good mechanical properties. From our earlier studies, good dispersion was observed by both dry mixing and melt mixing until 2% FS concentration. Melt mixing is preferred for FS concentrations above 2% in LLDPE. The SEM micrograph of LLDPE −4% FS, as depicted in Fig. 2, shows good dispersion of FS for the samples tested. With the addition of FS, an increase in melt viscosity due to entanglement of polymer chains was observed, along with improvements in mechanical properties. The improvements in mechanical properties of LLDPE with the addition of FS can be attributed to the restricted movement of polymer chains due to partial entanglement and adhesion of FS to polymer chains. This provides higher resistance to shear in the polymer melt, thus increasing viscosity and polymer chain reinforcement, enhancing the product's mechanical properties. There also exists a structure, consisting of a hydrogen bonding network between the LLDPE chains and silica groups, which leads to improved mechanical properties [12].

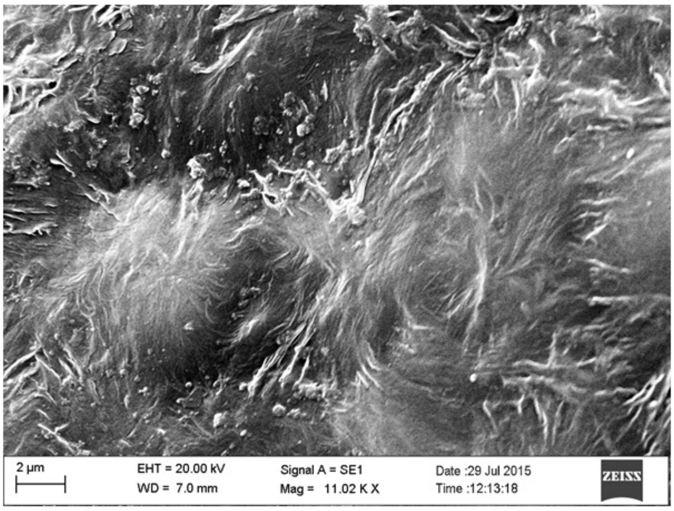

FIG. 2. Dispersion of FS in LLDPE - 4% FS blend

For stepped isothermal method (SIM), all the creep tests were done in single cantilever orientation at a constant stress of 0.5 MPa. The tests were done at increments of 10°C started from room temperature (30°C) to a maximum of 100°C providing a soak time of 5 minutes between every temperature step. The samples were loaded for 180 minutes at each temperature step (a dwell time of 10,000s is recommended by ASTM-D6992) for recording the creep strains. The SIM data were adjusted for thermal expansion and previous history of specimen by the change in temperature. The vertical shifting, rescaling and horizontal shifting were carried out to generate the creep master curves [13]. Creep master curves were generated for 40°C and 50°C and are shown in Fig. 3. As is readily seen from the graphs, the creep strains tend to decrease with the addition of FS. After an estimated loading of sample for one year (5.26×10^5 minutes) at 50°C nanocomposites with 4 wt% FS, exhibited 13% reduction in creep strains compared with natural LLDPE. Furthermore, the creep strains were reduced by as much as 13.5% for 4 wt% FS, which was predicted to be 5.26×10^7 minutes (around 100 years). The blends did not show significant variation in percentage of strain reduction with temperature. It was observed that, blends with 4 wt% FS showed 14% creep strain reduction at 40°C for an estimated loading of 1 year. The measurement of PIAT during rotational molding suggested a possible reduction of PIAT for LLDPE-FS blends. At 4% concentration, a PIAT of 175°C afforded products with good mechanical properties and minimum inner surface blow holes. This represents a reduction in cycle times and energy costs, as a PIAT of 210°C is preferred for natural LLDPE.

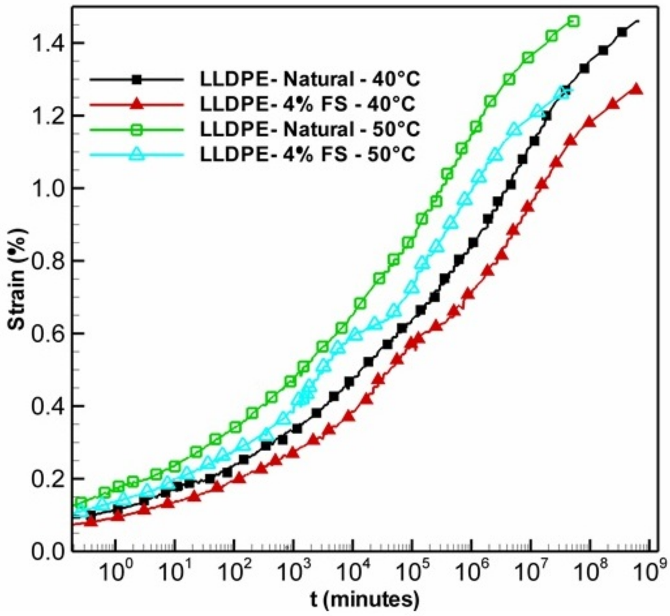

FIG. 3. Creep master curves of LLDPE and LLDPE-4% FS blends

Another important factor for cycle time reduction is mold release time. The adhesion of polymer to the mold and frictional resistance causes difficulty in the removal of products from a mold. Applying surface coatings and mold release agents reduces frictional resistance, however, applying mold release agents is time consuming and coating will deteriorate over time. Our investigations on pulling force required for removing the product from mold, as measured by a standard UTM using a unique fixture with mold cavity and internal heating is summarized in Fig. 4. It can be observed that the pulling force needed to remove the product from mold reduces with the addition of FS for both mild steel and aluminium molds. The minimum pulling force was observed at 80°C and thus it can be considered the ideal temperature to remove the product from the mold. The results show that the use of aluminium mold reduced the pulling force in comparison with that of steel molds at all temperatures. The reduction of pulling force ensures easy removal of the formed product, thereby reducing the cycle time.

3. Conclusion

In this study, rotationally moldable grade natural LLDPE and LLDPE-4%FS blends were used to study the dynamic mechanical characteristics of the parts produced by rotational molding. The improved viscoelastic behavior of LLDPE-4%FS blends ensures better rigidity and strength for rotomolded products. The reduced creep rates observed in LLDPE-4%FS blends ensure better product life. It was also observed that enhanced mold

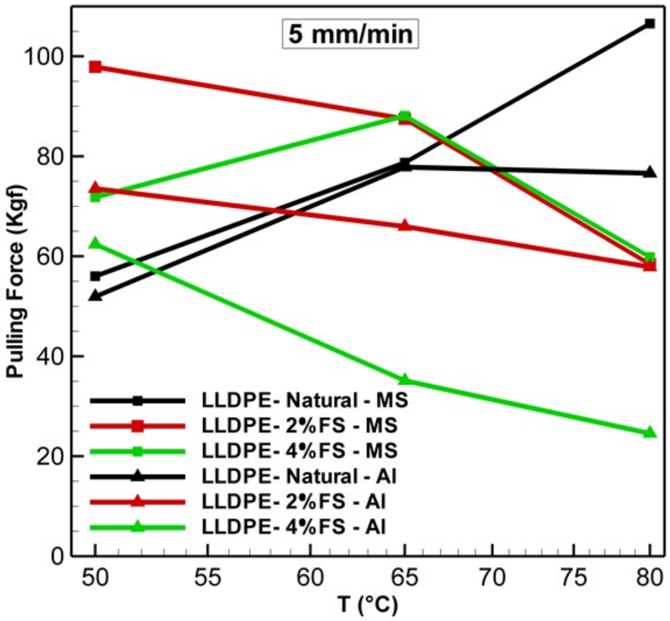

FIG. 4. Variation of pulling force

release and suggested reduction in PIAT considerably reduces the cycle time of the rotational molding process. In conclusion, LLDPE-4%FS blends make a better substitute for natural LLDPE in rotational molding applications.

References

[1] Therese L., Harkin-Jones E. An investigation into the relationship between the impact performance of rotationally molded polyethylene products and their dynamic mechanical properties. *Polymer Engineering & Science*, 2003, **43**, P. 905–918.

[2] Bellehumeur C.T., Tiang J.S. Simulation of Non-Isothermal Melt Densification of Polyethylene in Rotational Molding. *Polymer Engineering & Science*, 2002, **42**, P. 215–229.

[3] Jancar J., Douglas J.F., Starr F.W., Kumar S.K., Cassagnau P., et al. Current issues in research on structure-property relationships in polymer nano composites. *Polymer*, 2010, **51**, P. 3321–3343.

[4] Cassagnau P. Melt rheology of organoclay and fumed silica nanocomposites. *Polymer*, 2008, **49**, P. 2183–2196.

[5] Molefi J.A., Luyt A.S., Krupa I. Comparison of the influence of copper micro and nano particles on the mechanical properties of polyethylene/copper composites. *Journal of Material Science*, 2009, **45**, P. 82–88.

[6] Esthappan S.K., Kuttappan S.K., Joseph R. Thermal and mechanical properties of polypropylene/titanium dioxide nanocomposite fibers. *Materials & Design*, 2012, **37**, P. 537–542.

[7] Philippova O., Barabanova A., Molchanov V., Khokhlov A. Magnetic polymer beads: Recent trends and developments in synthetic design and applications. *European. Polymer. Journal*, 2011, **47**, P. 542–559.

[8] Karamipour S., Ebadi-Dehaghani H., Ashouri D., Mousavian S. Effect of nano-$CaCO_3$ on rheological and dynamic mechanical properties of polypropylene: Experiments and models. *Polymer. Testing*, 2011, **30**, P. 110–117.

[9] Cassagnau P., Mélis F. Non-linear viscoelastic behavior and modulus recovery in silica filled polymers. *Polymer*, 2003, **44**, P. 6607–6615.

[10] Chandran V.G., Waigaonkar S.D. Rheological and dynamic mechanical characteristics of rotationally moldable linear low-density polyethylene fumed silica nano composites. *Polymer. Composites*. In press, DOI: 10.1002/pc.23496.

[11] Nielsen L.E. Transitions in ethylene polymers. *Journal of Polymer Science*, 1960, **42**(140), P. 357–366.

[12] Dorigato A. Linear low density polyethylene/cycloolefin copolymer blends. *Express Polymer Letters*, 2010, **5**(1), P. 23–37.

[13] Achereiner F., Engelsing K., Bastian M., Heidemeyer P. Accelerated creep testing of polymers using the stepped isothermal method. *Polymer. Testing*, 2013, **32**, P. 447–454.

NANOSYSTEMS: PHYSICS, CHEMISTRY, MATHEMATICS, 2016, 7 (4), P. 613–617

Dielectric relaxation and charge transport process in $PrCrO_3$ nano-ceramic

Sujoy Saha[1], Alo Dutta[2*], P. K. Mukhopadhyay[2] and T. P. Sinha[1]

[1]Department of Physics, Bose Institute, 93/1, Acharya Prafulla Chandra Road, Kolkata-700009, India
[2]Department of Condensed Matter Physics and Material Sciences, S. N. Bose National Centre for Basic Sciences, Block-JD, Sector-III, Salt Lake, Kolkata-7000106, India

*alo_dutta@yahoo.com

PACS 61.05.cp, 77.22.Gm **DOI 10.17586/2220-8054-2016-7-4-613-617**

In this work we have investigated the frequency dependent dielectric properties of $PrCrO_3$ nano-ceramics using alternating current impedance spectroscopy. The material was synthesized by the sol–gel process. The Rietveld refinement of the X-ray diffraction data suggests single phase formation of the material with Pnma space group. The observed structure is substantiated by Raman spectrum of the sample. The ac conductivity follows the power law. The most probable relaxation frequencies at different temperatures were found to obey Arrhenius' law.

Keywords: Dielectric properties, sol-gel process, X-ray diffraction.

Received: 31 January 2016

1. Introduction

The rare-earth (R) transition-metal (M) oxides of perovskite structure with general formula RMO_3 have been the subject of investigation in recent years as they possess various interesting phenomena such as high temperature superconductivity, colossal magnetoresistance, and multiferroicity. Among these materials, rare–earth based orthochromites with general formula $RCrO_3$ have been investigated for their usefulness in several devices such as solid–oxide fuel cells and catalytic converters [1]. One of these orthochromites, $PrCrO_3$ (PCO), is an anti-ferromagnetic material with a Neel temperature of 237 K [2]. The Cr^{3+} spin structure is predominately G_x-type and a weak ferromagnetic moment lies along c-crystallographic axis at 4.2 K in PCO [2]. Prasad et al. [3] have investigated the relaxor ferroelectric like permittivity of bulk PCO ceramic having 30 nm grain size. Zhang et al. [4] have synthesized the cubic particle of orthorhombic PCO by hydrothermal process. Their results have showed that the molar ratio 1:1 of Pr and Cr can be obtained when the material is synthesized at 280 °C for 7 days using 8 M KOH solution.

The magnetic property of PCO is extensively studied, but to the best of our knowledge there is no report on the dielectric properties of PCO nano-ceramic till date. In the present work we have investigated the dielectric relaxation and ac conductivity of PCO nanoparticles synthesized by the sol-gel process.

2. Experimental

To prepare the PCO nano-ceramic, the metal nitrates with 1:1 molar ratio were dissolved in deionized water separately. Citric acid and ethylene glycol solution was added dropwise to the metal nitrates solution and stirred at 353 K for 6 h to form the gelled mass by auto combustion process. The dried gel was then calcined at 973 K in air for 4 h. The calcined sample was compressed into disc and sintered at 1023 K for 6 h. Scanning electron micrograph and energy dispersive X-ray spectrum were taken by a FEI QUANTA 200 scanning electron microscope. Transmission electron micrograph (TEM) was taken by TECNAI 200 kV transmission electron microscope. The X-ray diffraction (XRD) pattern of calcined PCO was taken by Rigaku Miniflex-II X-ray diffractometer. Raman spectrum was collected by Jobin-Yvon LABRAM-HR spectrometer using 488 nm line of an Ar-ion laser line. The frequency dependence capacitance and conductance of sintered pellet were measured by an LCR meter (Hioki) at frequencies ranging from 42 Hz to 1 MHz in temperature range from 303 – 673 K.

3. Results and disscussion

3.1. Structural Analysis

The Rietveld refinement of the room temperature XRD pattern of PCO with orthorhombic symmetry having Pnma (D_{16}^{2h}) space group using Full-prof code is shown in Fig. 1. The good agreement between the observed and calculated interplanar distances (d-values) of PCO indicates the single phase formation of the material in Pnma space group symmetry. The unit cell parameters, reliability factors, bond distances and bond angles obtained from

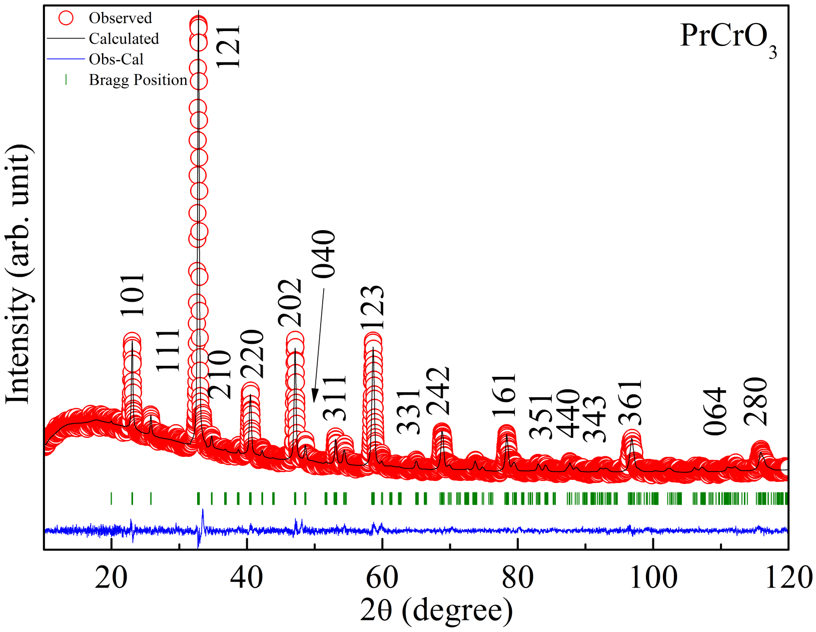

FIG. 1. Rietveld refinement of XRD profile of $PrCrO_3$ at room temperature

TABLE 1. Rietveld refinement data

Lattice parameters (Å)	Bond length(Å)	Bond angle
$a = 5.4721(5)$	$\langle \mathrm{Pr-OI} \rangle = 2.79$, $\langle \mathrm{Pr-OII} \rangle = 2.29$	Cr – OI – Cr = 154.3 °
$b = 7.7107(5)$	$\langle \mathrm{Cr-OI} \rangle$ 1.99, $\langle \mathrm{Cr-OII} \rangle = 1.96$	Cr – OII – Cr = 161.1 °
$c = 5.4445(5)$	$R_P = 3.76$, $R_{wp} = 4.93$, $R_{exp} = 5.23$, $\chi^2 = 0.891$	

Atom	x	y	z	Multiplicity	B_{iso} (Å^2)
Pr	0.5357(3)	0.25	0.4946(9)	4	0.429
Cr	0.25	0	0	4	0.087
OI	−0.0184(4)	0.25	0.5945(8)	4	0.705
OII	0.2891(7)	0.0235(5)	0.72077(7)	8	0.972

Rietveld refinement are given in Table 1. The mean size of coherent scattering regions, as calculated from the XRD data, was found to be 100 nm.

The high resolution TEM (HRTEM) image and selected area electron diffraction (SAED) pattern of PCO are shown in Fig. 2. The HRTEM image presented in Fig. 2(a) shows the well resolved lattice fringes of nanoparticles. The SAED pattern shows strong spots in regular positions indicating that particles are well crystalline in nature. The SEM image as shown in Fig. 2(c) indicates the compactness of the grains. The average grain size is found to be 92 nm. EDAX analysis shows that the atomic percentage of Pr, Cr and O in PCO is 19.09 %, 15.27 % and 65.64 % respectively.

We have studied the Raman spectrum of PCO to get a better understanding of the crystal structure and its consequence on the vibrational features of the material. The room temperature Raman spectrum of PCO as shown in Fig. 3 (Symbols are the experimental points) is typically matched with the Raman spectrum of perovskite having orthorhombic crystal structure. According to group theory, the orthorhombic Pnma structure has 24 Raman active modes ($7A_g + 5B_{1g} + 7B_{2g} + 5B_{3g}$) at the zone center. The antiphase tilt of the adjacent CrO_6 octahedra and the antiparallel displacements of Pr cations activate the Raman modes. The sum of 20 Lorentzian lines (violet solid lines in Fig. 3) is used to fit the experimental data. For the clarity of the figure, the frequency range is divided into two parts. Very weak intensity peaks are neglected during the Lorentzian fitting of the experimental data and thus a lesser number of peaks are obtained than the theoretical prediction.

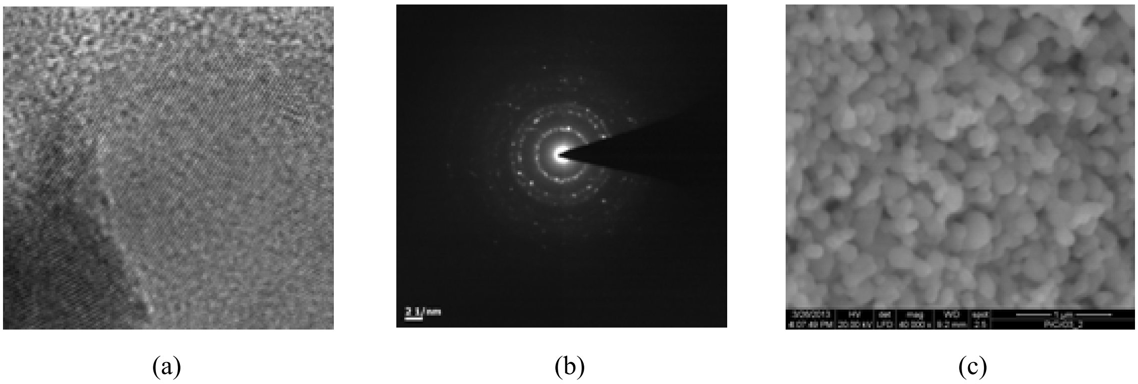

(a) (b) (c)

FIG. 2. HRTEM (a), SAED pattern (b) and SEM image (c) of $PrCrO_3$

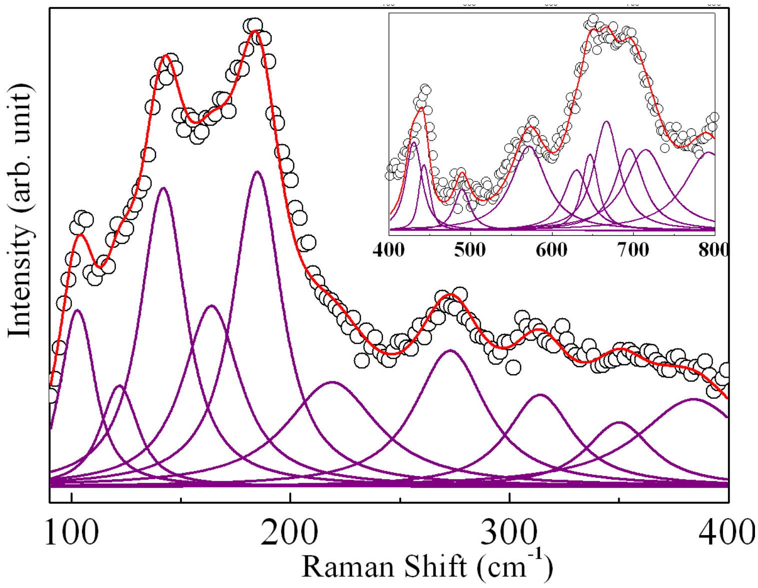

FIG. 3. Raman spectrum of $PrCrO_3$ at room temperature

3.2. Ac conductivity and dielectric relaxation

The angular frequency ($\omega = 2\pi\nu$) dependent log-log plots of ac conductivity (σ_{ac}) for PCO at different temperature are shown in Fig. 4. At each temperature, the conductivity decreases with decreasing frequency and becomes independent of frequency in the low frequency region. The extrapolation of this region towards $\omega = 0$ gives dc conductivity (σ_{dc}) which is attributed to the long range translational motion of the charge carriers. In this low frequency region, the electric field cannot perturb the hopping conduction mechanism of charged particles and hence, the conductance is approximately equal to the dc value. As the temperature is increased, the dc part of the conductivity spectra shifts to higher frequency side. The large value of dc conductivity at the higher temperature range with respect to the value in the lower temperature range indicates the generation of large number of thermally activated charge carriers in the experimental temperature range. The conductivity begins to increase after the frequency exceeds the critical frequency called hopping frequency (ω_H). The conductivity spectra of PCO follow the power law [5] as shown by the solid lines in Fig. 4. The temperature dependence of σ_{dc} obtained from the fitting of the experimental data to the power law at different temperatures follows Arrhenius' law (inset of Fig. 4) with an activation energy of 0.32 eV. The activation energy value indicates that polaron hopping may be responsible for conduction processes in PCO.

In Fig. 5 the frequency dependent dielectric constant (ε') and loss tangent ($\tan\delta$) of PCO as a function of temperature are shown. The observed peaks in $\tan\delta$ can be explained according to the fact that a strong correlation between the conduction mechanism and the dielectric behavior exists in PCO. For a thermally activated relaxation

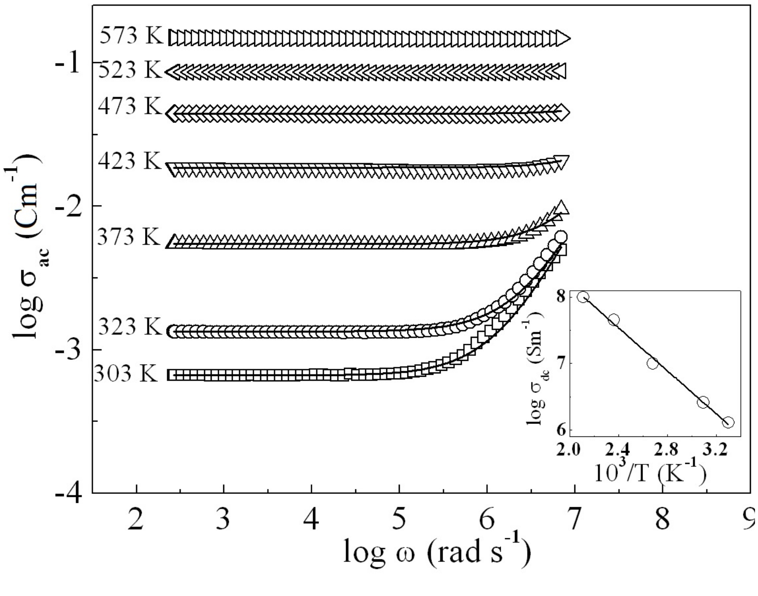

FIG. 4. Frequency dependent Ac conductivity. Inset is the temperature dependence of σ_{dc}

process, the relaxation time τ has the form $\tau_0 \exp(E/k_B T)$, where E and k_B are the activation energy for the relaxation process and the Boltzmann constant, respectively. Then the resonant condition is $\omega_{\max}\tau_0 \exp(E/k_B T) = 1$, where $\omega_{\max}$ is the frequency at which $\tan\delta$ has its maximum value. The temperature dependence of the most probable relaxation frequency ($\omega_{\max}$) follows Arrhenius' law (inset of Fig. 5), and a straight line fit to the experimental data gives an activation energy of 0.319 eV. This activation energy is equal to the activation energy obtained for the temperature dependence of σ_{dc}. This suggests that the dielectric loss in PCO is due to the conduction of charge carriers.

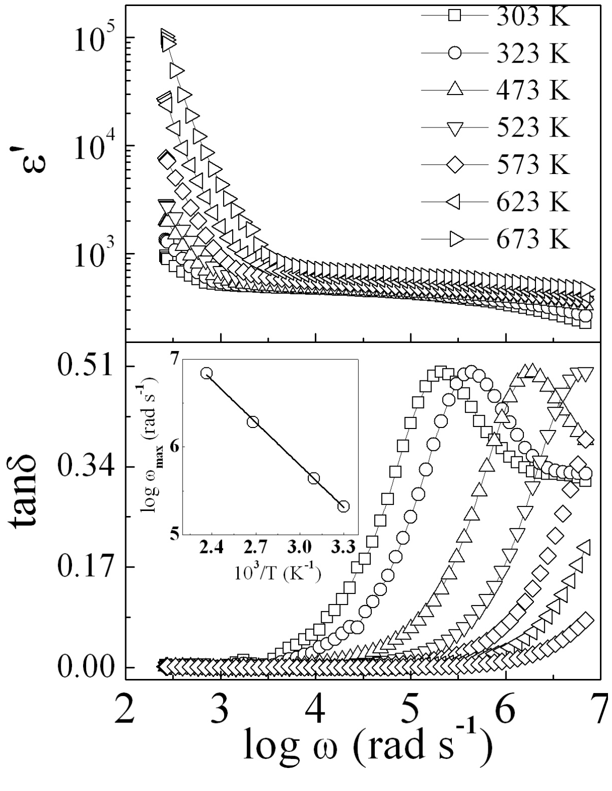

FIG. 5. Frequency dependence of ε' and $\tan\delta$. Inset is the Arrhenius plot of $\omega_{\max}$

4. Conclusions

The Rietveld refinement of XRD profile suggests the single phase formation of PCO with Pnma space group. The Raman spectrum fitted with 20 Lorentzian lines substantiates the orthorhombic crystal structure of PCO with space group Pnma. The dielectric properties of the sample have been investigated as a function of frequency and temperature. The frequency-dependent conductivity spectra follow the power law. The activation energy for charge carrier transport is found to be 0.32 eV, which indicates that polaron hopping plays the main role for the dielectric relaxation in PCO.

Acknowledgements

Alo Dutta thanks to Department of Science & Technology of India for providing the financial support through DST Fast Track Project under Grant No. SB/FTP/PS–175/2013.

References

[1] Shen Y., Liu M., San T.H., Jiang P. Preparation, Electrical Conductivity, and Thermal Expansion Behavior of Dense $Nd_{1-x}Ca_xCrO_3$ Solid Solutions. *J. Am. Ceram. Soc.*, 2009, **92**, P. 2259-?2264.

[2] Gordon G.D., Hornrcich R.M., Shtrikman S., Wanklyn B.M. Magnetization studies in the rare-earth orthochromites. V. $TbCrO_3$ and PrCrO. *Phys. Rev. B*, 1976, **13**, P. 3012–3017.

[3] Prasad B.V., Rao G.N., Chen J.W., Babu D.S. Relaxor ferroelectric like giant permittivity in $PrCrO_3$ semiconductor ceramics. *Mater. Chem. Phys.*, 2011, **126**, P. 918–921.

[4] Zhang Y., Yao C., Fan Y,. Zhou M. One-step hydrothermal synthesis, characterization and magnetic properties of orthorhombic $PrCrO_3$ cubic particles. *Mater. Res. Bull.*, 2014, **59**, P. 387–393.

[5] Jonscher A.K. *Universal relaxation law*. Chelsea Dielectrics Press, London, 1996.

NANOSYSTEMS: PHYSICS, CHEMISTRY, MATHEMATICS, 2016, 7 (4), P. 618–620

Influence of bismuth on the microstructure, hardness and dry sliding wear behavior of magnesium silicide reinforced magnesium alloy composite

D. E. Umesha[1], D. Shivalingappa[2], R. Kishore Kumar[2], Binto Tomy[2], D. Ramesh Rao[3]

[1]Bapuji Institute of Engineering and Technology, Davangere–577004, India

[2]Adhiyamaan College of Engineering, Hosur–635109, India

[3]M.S. Ramaiah Institute of Technology, Bangalore–560099, India

dsivadvg@gmail.com, kishore.rg7@hotmail.com

PACS 06.20.-f 12.60.Rc 61.10.Nz **DOI 10.17586/2220-8054-2016-7-4-618-620**

The modification effect of bismuth (Bi) on in-situ-formed magnesium silicide (Mg_2Si) reinforced magnesium-aluminium (Mg–Al) alloy is investigated using optical microscope, scanning electron microscope and X-ray diffraction. Processing of the in-situ composite was carried out through a stir casting technique. The size of Mg_2Si is significantly refined and the optimal modification effect was obtained when the Bi content in the composite is 1.4%. A slight decrease in hardness values and increase in wear resistance were observed in the study with bismuth addition.

Keywords: Mg–Al Alloy, bismuth, modifier, in-situ composite, wear resistance.

Received: 3 February 2016

Revised: 4 April 2016

1. Introduction

Increasing the fuel efficiency of a vehicle is one of the main considerations in automotive field, which in turn, is directly influenced by the weight of the vehicle. Magnesium alloys and composites are the lightest structural materials which can be used extensively in automotive industries. Magnesium metal matrix composites can be processed using both ex-situ and in-situ techniques. However, it has been noted that the in-situ method of processing results in improved grain structure, mechanical properties and wear properties for the final metal matrix composites [1, 2]. Magnesium alloys containing Mg_2Si particles seem to show high melting temperatures, low density, high hardness, low thermal expansion coefficients and reasonably high elastic moduli. Uniform morphology of Mg_2Si particles is difficult to obtain and moreover the size of these particles are larger in nature [3]. This can lead to poor mechanical properties for the composite. Modification is found to be a simple and effective technique for improving the morphology and size of Mg_2Si particles in Mg–Al alloys [4]. Modification of Mg_2Si can be also done by adding additives such as P, Li, Na, KBF4, Ca, La [5–8] etc. Bismuth is found to be one of the suitable additives that can be used for the modification of Mg_2Si particles.

The primary aim of the present study was to investigate the effect of Bi modification on the Mg_2Si phase in Mg–Al alloy. Based on these results, the hardness and dry sliding wear behavior of composites with different amounts of Bi were investigated.

2. Experimental Procedures

2.1. Materials and Processing

Commercially pure Mg ingot (99.3% purity), Al ingot (99.2% purity) and Si powder (99.9% purity) were used as the starting materials to prepare the Mg–Al/ Mg_2Si composites. The melting process was carried out in a steel crucible kept in a 2 kW electric resistance furnace under a protective atmosphere of argon gas. The furnace had a bottom pouring configuration and was also provided with an inert gas atmosphere.

The processing of composites was carried out in two stages by a stir casting technique. In the first stage, cast aluminium-silicon master alloy was synthesized by dispersing silicon particles into the molten aluminium. In the second stage, cast Al–Si master alloy was dissolved in the molten magnesium (760 °C) in such amounts so that the final mixture had 9 wt% Al in Mg–Al matrix alloy and 2.5 wt% Mg_2Si reinforcement. For refinement of Mg_2Si bismuth (0, 0.7, 1.4, 2 wt%) was added to the molten magnesium. Stirring was done at 600 rpm for 10 minutes for all samples. Finally, the composite slurry was poured into a 30mm×50mm×120mm steel mold.

2.2. Materials characterization and phase analysis

XRD analysis was carried out for powders from Mg–Al/ Mg_2Si composite containing 1.4 wt% Bi and Mg–Al/ Mg_2Si composite without Bi. Specimens for microstructure analysis were prepared using standard procedures and optical microscopy and SEM examination and EDS analysis were carried out.

2.3. Hardness and wear tests

The Brinell hardness test was used to measure the hardness of the specimens. Test specimens were indented with a 5 mm diameter hardened steel ball subjected to a load of 150 N applied for 10 seconds. Dry sliding wear tests were conducted according to the ASTM G99 standard using pin-on-disc machine. The wear tests for all specimens were conducted under two different loads (10 N and 20 N) and varying the disc rotating speeds of 300, 350, 400 and 450 rpm. Wear tests were carried out for a total sliding distance of approximately 1000 m. The pin samples were 30 mm in length and 8 mm in diameter.

3. Results and Discussion

3.1. Microstructural features

Figure 1 shows the XRD patterns of Mg–Al/ Mg_2Si composite without Bi content and with 1.4 wt. % Bi content respectively. The XRD pattern reveals that the processed in-situ composite contains α-Mg, β-$Al_{12}Mg_{17}$ and Mg_2Si phases. Some new peaks appear in the pattern with the addition of 1.4 wt. % Bi. The XRD pattern of the in-situ composite which was processed with the bismuth refinement material confirmed the presence of bismuth by showing the additional peaks corresponding to it.

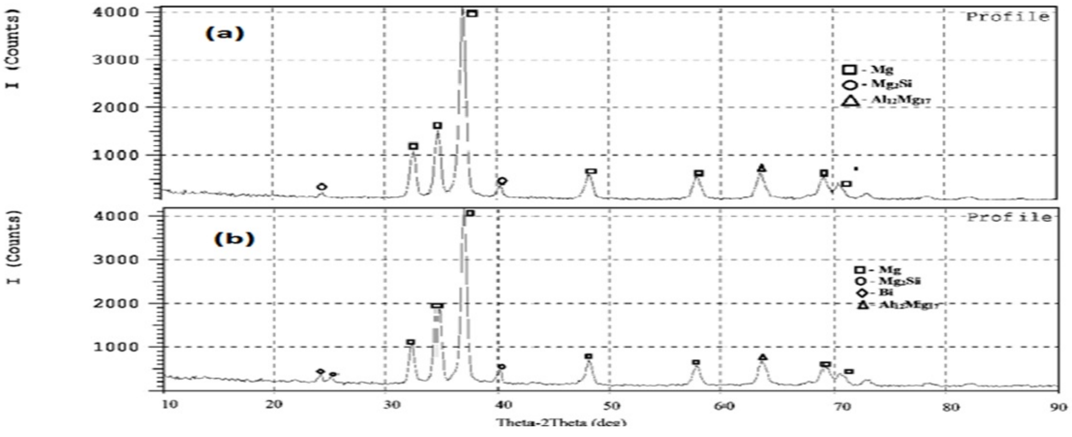

FIG. 1. XRD pattern of Mg–Al/ Mg_2Si composite (a) 0 wt% (b) 1.4 wt% Bi

The SEM micrographs, along with EDS patterns for in-situ composite with and without bismuth are shown in Figs. 2(a) and 2(b) respectively. The presence of bismuth was confirmed from the additional peaks, as is seen in Fig. 2(b) compared to peaks in Fig. 2(a). The larger size of the reinforcing Mg_2Si particles can be seen in the Fig. 2(a), whereas refined and smaller size of Mg_2Si phase can be seen in Fig. 2(b). Small white spots in Fig. 2(b) correspond to bismuth powder. The Mg_2Si particles in an unmodified sample were found to be clustered throughout as large particles.

The morphology was poor when compared to the 2% Bismuth modified specimen. As the percentage of bismuth increased, the Mg_2Si particles became divided, finally resulting in a unique particle distribution. However, it is also readily seen that the particles became coarser with more addition of bismuth.

3.2. Hardness and wear tests

Hardness tests revealed that Bi decreases the hardness value of the composites; however its variation is limited. The Mg–Al/ Mg_2Si composite showed better hardness properties than those Mg–Al/ Mg_2Si composites which were modified by varying amounts of bismuth. The hardness graph of the composite (Mg–Al/ Mg_2Si) with varying bismuth content is shown in Table 1.

Figure 3 shows the variation of wear rate for Mg–Al/Mg_2Si composite with Bi content. A decrease in wear rate can be seen with an increased Bi content and speed. However, the variation of decrease for wear rate can be seen more at higher loads (20N).

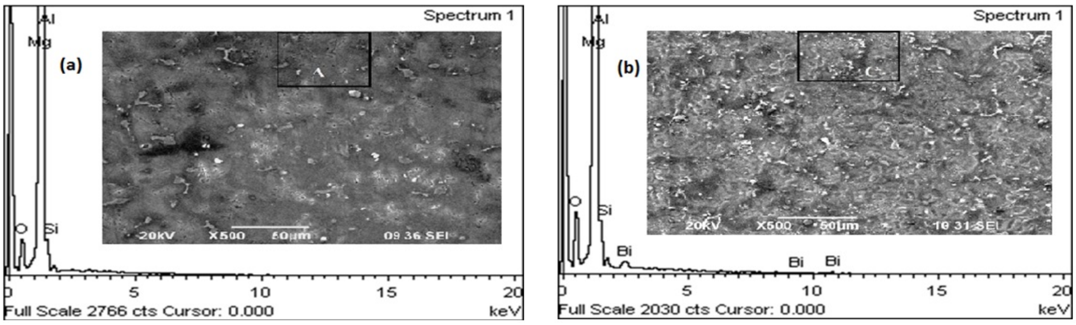

FIG. 2. SEM images with EDS of Mg–Al/ Mg_2Si (a)without and (b)with 1.4 wt% Bi

TABLE 1. Variation of hardness of Mg–Al/ Mg_2Si composite with Bi content

Bismuth (wt%)	0	0.7	1.4	2
Hardness (BHN)	72.9	69.3	69.3	71.5

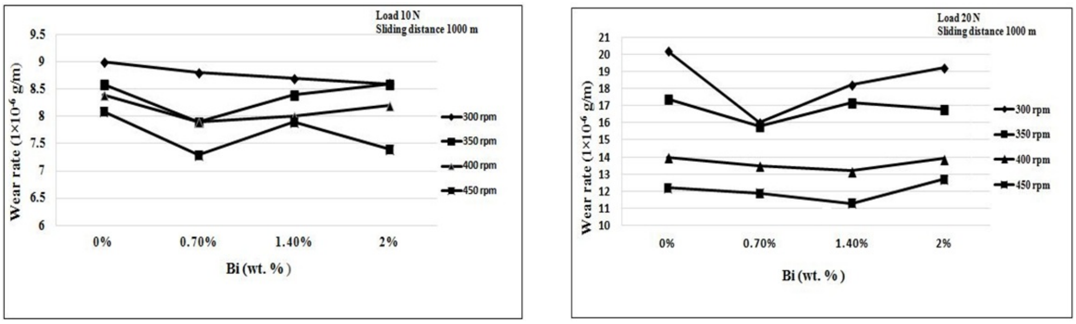

FIG. 3. Variation of wear rate of Mg–Al/ Mg_2Si composite with Bi content

4. Conclusion

From the research, it can be indentified that bismuth plays a significant role in modifying the morphology of Mg_2Si particles in Mg–Al/Mg_2Si composite. The size of the Mg_2Si particles and the hardness values decreased with the addition of bismuth (Bi). However, it was shown that Bi exerts a great influence on wear resistance, as that property was enhanced with increased bismuth content.

References

[1] Bhingole P.P., Chaudhari G.P., Nath S.K. Processing, microstructure and properties of ultrasonically processed in situ MgO-Al_2O_3–$MgAl_2O_4$ dispersed magnesium alloy composites. *Compos. Part A Appl. Sci. Manuf.*, 2014, **66**, P. 209–217.

[2] Shivalingappa D., Daniel B.S.S., Ray S. Effect of reinforcing phase inherited from another composite on the mechanical properties of cast magnesium base composite. *Mater. Sci. Eng. A*, 2012, **541**, P. 172–180.

[3] Hu Y., Rao L. Effect of particulate reinforcement on wear behavior of magnesium matrix composites. *Trans. Nonferrous Met. Soc. China*, 2012, **22**, P. 2659–2664.

[4] Hu J., Tang C., Zhang X., Deng Y. Modification of Mg_2Si in Mg–Si alloys with neodymium. *Trans. Nonferrous Met. Soc. China*, 2013, **23**, P. 3161–3166.

[5] Tang S., Zhou J., Tian C., Yang Y. Morphology modification of Mg_2Si by Sr addition in Mg-4%Si alloy. *Trans. Nonferrous Met. Soc. China*, 2011, **21**, P. 1932–1936.

[6] Qin Q.D., Zhao Y.G., Zhou W., Cong P.J. Effect of phosphorus on microstructure and growth manner of primary Mg_2Si crystal in Mg_2Si/Al composite. *Mater. Sci. Eng. A*, 2007, **447**, P. 186–191.

[7] Hadian R., Emamy M., Varahram N., Nemati N. The effect of Li on the tensile properties of cast Al-Mg_2Si metal matrix composite. *Mater. Sci. Eng. A*, 2008, **490**, P. 250–257.

[8] Emamy M., Khorshidi R., Raouf A.H. The influence of pure Na on the microstructure and tensile properties of Al-Mg_2Si metal matrix composite. *Mater. Sci. Eng. A*, 2011, **528**, P. 4337–4342.

NANOSYSTEMS: PHYSICS, CHEMISTRY, MATHEMATICS, 2016, 7 (4), P. 621–623

Effect of substrate temperature on microstructure and properties of nanocrystalline titania thin films prepared by pulsed laser deposition

G. Balakrishnan[1], S. Manavalan[2], R. Venkatesh Babu[3] and J. I. Song[4]

[1]Centre of Excellence in Patterned Multiferroics & Nanotechnology, Bharath Institute of Science and Technology, Bharath Institute of Higher Education and Research, Chennai – 73, India

[2]Department of Mechanical Engineering, Bharath Institute of Science and Technology, Bharath Institute of Higher Education and Research, Chennai – 73, India

[3]Department of Mechanical Engineering, Sri Lakshmi Ammal Engineering College, Chennai – 126, India

[4]Department of Mechanical Engineering, Chanwon National University, Changwon – 641773, South Korea

balaphysics76@gmail.com, manavalan.kannan@gmail.com, rvbaboo76@gmail.com, jisong@changwon.ac.kr

PACS 81.07. -b **DOI 10.17586/2220-8054-2016-7-4-621-623**

Titanium oxide (TiO_2) films were deposited on silicon (100) and quartz substrates at various substrate temperatures (300 – 873 K) at an optimized oxygen partial pressure of 3.0×10^{-2} mbar by pulsed laser deposition. The effect of substrate temperature on structure, surface morphology and optical properties of the films were investigated using X-ray diffraction (XRD), atomic force microscopy (AFM) and photoluminescence spectroscopy (PL) respectively. The XRD results showed that the films are polycrystalline in nature and have tetragonal structure. The film prepared at higher substrate temperature showed strong rutile phase. The results indicated that all the films possess both phases (anatase and rutile) of titania. The AFM shows the crystalline nature, dense, uniform distribution of the nanocrystallites with a surface roughness of 2 – 8 nm. The photoluminescence studies showed the asymmetric peak $\sim$ 370 nm indicating the bandgap for the TiO_2 films.

Keywords: Titania, thin films, pulsed laser deposition, X-ray diffraction (XRD), atomic force microscopy (AFM), photoluminescence spectroscopy (PL).

Received: 5 February 2016

1. Introduction

Titania (TiO_2) exists in rutile, anatase and brookite phases. TiO_2 thin films are widely studied due to their interesting chemical, electrical and optical properties. TiO_2 thin films exhibit unique properties such as high dielectric constant, wide optical bandgap, high refractive index, photo catalytic, low absorption and high transparency with high chemical and thermal stabilities. Because of its excellent properties, it finds applications in heterogeneous catalysis, photocatalysts, self cleaning windows, solar cells, gas sensors, corrosion resistant coatings, optical coatings, metal oxide field effect transistors, varistors, Li-based batteries and electro chromic devices [1–3]. The occurrence of anatase and rutile phase of TiO_2 thin films mainly depends on the deposition method, process parameters and substrate temperature. Many techniques are used to deposit TiO_2 films, including sol-gel processes [4], reactive evaporation [5], chemical vapor deposition [6], sputtering [7, 8] and pulsed laser deposition (PLD) [9]. Among these techniques, pulsed laser deposition (PLD) is a simple technique to prepare high quality films from metal, semiconductors and ceramics. The rapid rate of ablation from target surface promotes the constituents of the target to evaporate congruently and to retain the stoichiometry in the film. There are many deposition parameters to be optimized to achieve the optimum properties. The oxygen partial pressure and the substrate temperature play an important role to produce high quality films by PLD. The preparation method and process parameters of TiO_2 films are of fundamental importance for obtaining the optimum properties for various applications. In the present work, nanocrystalline TiO_2 films were deposited on silicon and quartz substrates as a function of substrate temperature by PLD and their microstructure and optical properties were investigated.

2. Experimental details

TiO_2 powder was compacted into a pellet of 30 mm diameter and 5 mm thickness using a uni-axial press. The pellet was sintered $\sim$ 1473 K for 8 hours and used as a target for the PLD. TiO_2 films were deposited on Si (100) and quartz substrates at various substrate temperatures from 300 K to 873 K. The films were deposited using KrF excimer laser ($\lambda = 248$ nm) with a repetition rate of 10 Hz. X-ray diffraction (XRD) studies were carried out using X'pert PW 3040 D-8 (PANalytical) diffractometer with $CuK_{\alpha1}$ radiation. The surface topographies and roughnesses of the films were analyzed using atomic force microscope (XE-100 Park systems) in non-contact mode. The photoluminescent spectra of these films were recorded using a (Shimadzu, RF-5301PC) spectrofluorophotometer.

3. Results and Discussion

3.1. Microstructural studies

XRD pattern of the TiO_2 thin films is shown in Fig. 1. The XRD pattern shows the peaks at angles 25.8 ° and 37.9 °, corresponding to the anatase phase ((JCPDF # 21-1272), while the peaks at angles 27.5 °, 44.2 °, 56.5 °, 64.3 ° indicate the rutile phase (JCPDS # 21-1276) of titania. In the XRD pattern, A and R denotes the anatase and rutile phase of titania respectively [9]. The XRD results showed that the films were polycrystalline in nature and had tetragonal structure. The films deposited in the lower substrate temperatures (300 – 673 K), showed the small intense peaks corresponding to both anatase and rutile phases, while the films deposited at higher substrate temperatures (773 K and 873 K) indicated the strong peaks corresponding to the rutile phase. This indicated the higher rutile phase content and smaller anatase phase content in the films with increasing substrate temperature. The formation of rutile phase with temperature was due to the high energy of particles impinging on the substrate kept at higher temperature. The thickness of the films increased with increasing temperature. The anatase to rutile phase transformation takes place over a wide range of temperatures (from 823 to 1073 K). Ben Amor et al. [10] investigated the properties of TiO_2 films and observed the amorphous nature in the as-deposited condition, while the annealed films at 873 K showed anatase phase.

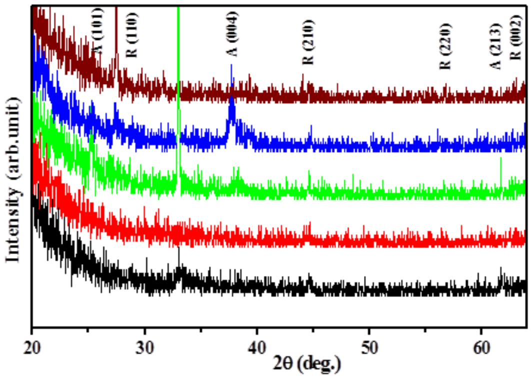

FIG. 1. XRD pattern of the TiO_2 thin films deposited on Si (100) at different substrate temperatures

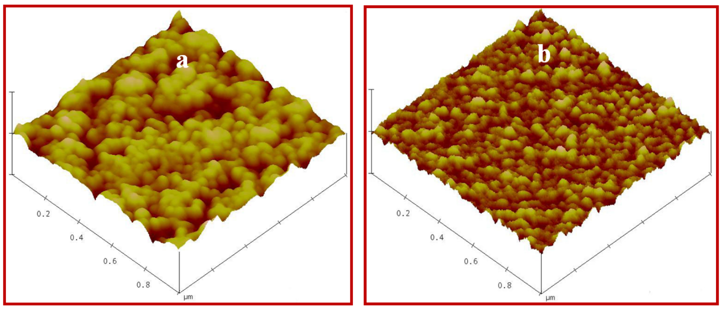

FIG. 2. AFM images of the TiO_2 films prepared at (a) 300 K and (b) 873 K

Figure 2 shows the AFM images of the typical films prepared at room temperature (300 K) and 873 K. The images showed the dense crystallites, uniform formation of the crystallites and smooth morphology. The mobility of the ad-atoms is higher at higher substrate temperatures and the film prepared at 873 K showed the coalescence of the crystallites. The surface roughness of the films were measured and found to be in the range 3 – 8 nm.

3.2. Photoluminescence studies

Figure 3 shows the photoluminescence (PL) spectra of the TiO_2 films deposited on silicon (100) substrates at various substrate temperatures. The PL spectra of the films were analyzed using 325 nm laser excitation wavelength. PL spectra showed broad and asymmetric peaks, indicating the presence of both anatase and rutile phases. At 873 K, two PL peaks were observed, indicating the clear anatase and rutile peaks. The small intense peak ∼ 470 nm (2.7 eV) is probably due to the structural defects, which are related to deep-level emissions like oxygen vacancy [9, 11, 12]. The PL peak intensity of TiO_2 films with respect to substrate temperature is associated with its crystallinity and defects. The glancing incidence X-ray diffraction (GIXRD) results of the films showed more rutile phase (Fig. 1) at higher substrate temperatures. The PL peak intensity decreases systematically with the increased substrate temperature [9]. The variation of PL peak intensity is related to the formation of rutile and anatase phases at different substrate temperatures. The PL results are consistent with our XRD results [13]. All these results showed that the optical properties of TiO_2 films are dependent on their microstructure influenced by substrate temperature. Table 1 gives the details for the crystallite size, surface roughness and bandgap of the titania films with respect to the substrate temperature.

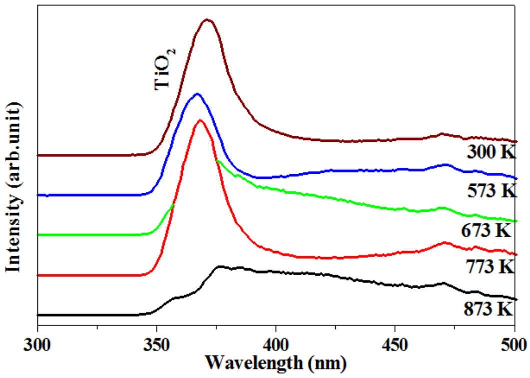

FIG. 3. Photoluminescence spectra of the TiO_2 films prepared at different temperatures

TABLE 1. Substrate temperature *vs* crystallite size, surface roughness and bandgap

Substrate Temp. (K)	Crystallite size Rutile (110) (nm)	Surface roughness AFM (nm)	Bandgap (eV) PL
300	—	3.0	3.35
573	—	5.2	3.37
673	—	6.5	3.37
773	30	7.2	3.37
873	48	8.0	3.30

4. Conclusions

The TiO_2 thin films were deposited on Si (100) and quartz substrates at various substrate temperatures by pulsed laser deposition. The XRD studies indicated small intense peaks corresponding to both anatase and rutile phases at low substrate temperatures, while the strong peaks indicated higher rutile phase content at higher substrate temperatures. The rutile phase content increased with increased substrate temperature. The AFM studies illustrated the dense, uniform distribution of the crystallites with smooth morphology. PL studies demonstrated the broad and asymmetric peaks ~ 370 nm, indicating a bandgap of $\sim 3.30 - 3.37$ eV.

References

[1] Gyorgy E., Socol G., et al. *Appl. Surf. Sci.*, 2005, **247** (4), P. 429–433.
[2] Tay B.K., Zhao Z.W., Chua D.H.C. *Mater. Sci. Eng. Rep.*, 2006, **52** (1), P. 178–182.
[3] Byun C., Jang J.W., et al. *Mater. Res. Bull.*, 1997, **32** (5), P. 431–440.
[4] Vorotilov K.A., Drlova E.V., Petrovsky V.L. *Thin Solid Films*, 1992, **207**, P. 135–144.
[5] Pulker H.K., Paesold G., Ritter E. *Appl. Opt.*, 1976, **15**, P. 2986.
[6] Lu J.P., Wang J., Raj R. *Thin Solid Films*, 1991, **204**, L13.
[7] Suhail M.H., Mohan Rao G., Mohan S.J. *Appl. Phys.*, 1992, **71** (3), P. 1421.
[8] Argelia Perez-Pacheco, Prieto C., Castaneda-Guzma R., Garcia-Lopez J. *Thin Solid Films*, 2009, **517**, P. 5415.
[9] Balakrishnan G., Vengala Rao Bandi, et al. *Mater. Res. Bull.*, 2013, **48**, P. 4901.
[10] Ben Amor S., Baud G., Besse J.P., Jacquet M. *Mater. Sci. Eng. B*, 1997, **47**, P. 110.
[11] Chung C.K., Liao M.W., Lai C.W. *Thin Solid Films*, 2009, **518**, P. 1415.
[12] Madhu Kumar P., Badrinarayanan S., Murali S. *Thin Solid Films*, 2000, **358**, P. 122.
[13] Gaurav Shukla, Pratima K. Mishra, Alika Khare. *J. Alloy Compd.*, 2010, **489**, P. 246.

NANOSYSTEMS: PHYSICS, CHEMISTRY, MATHEMATICS, 2016, 7 (4), P. 624–628

Study of Faraday effect on $Co_{1-x}Zn_xFe_2O_4$ nanoferrofluids

R. Karthick[1], K. Ramachandran[2], R. Srinivasan[3,*]

[1]Department of Physics, PSNA College of Engineering and Technology, Dindigul–624622, India

[2]School of Physics, Madurai Kamaraj University, Madurai–625021, India

[3]Department of Physics, Thiagarajar College, Madurai–625009, India

karthickr4584@gmail.com, thirumalchandran@gmail.com, *r_srini2067@yahoo.co.in

PACS 47.65.Cb, 63.50.Lm, 33.57.+c, 78.20.Ls **DOI 10.17586/2220-8054-2016-7-4-624-628**

Zinc doped cobalt ferrite$Co_{1-x}Zn_xFe_2O_4$ nanoparticles ($x = 0.1$, 0.5, 0.9) were synthesized by chemical co-precipitation method. The crystallite size, which was calculated from the full width half maximum (FWHM) value of the strongest peak (311) plane using Scherer approximation, was found to decrease with higher zinc content. The surface morphology of the powder samples was obtained using transmission electron microscopy (TEM). Magnetic properties, such as Saturation magnetization (M_s), Remanent Magnetization (M_r) and Coercivity of the powder samples, were measured using Vibrating Sample Magnetometer (VSM) at room temperature and were found to decrease with increased zinc content. Aqueous ferrofluids prepared from the powder samples were subjected to magnetic field to measure their Faraday rotation. Faraday rotation of the ferrofluids was found to increase with applied magnetic field and decrease with increasing zinc composition.

Keywords: nanoferrofluid, vibrating sample magnetometer, faraday rotation.

Received: 5 February 2016

Revised: 4 April 2016

1. Introduction

Ferrofluids are a colloidal suspension of single domain magnetic particles, with typical dimensions of about 10 nm, dispersed in a carrier liquid [1]. To avoid the aggregation of nanoparticles, they have to be covered with a suitable surfactant. Optical property of ferrofluids can be altered by external applied magnetic field [2]. Structural reorientation of the nanoparticles suspended in a magnetic colloid brings out magneto-optic properties [3], which are used in developing optical sensors [4], photonic devices [5], etc. The kinetics of particle aggregation in magnetic nanofluid have been studied using various techniques [6, 7]. The functional group adhered to the nanoparticles (stabilizers) can influence the kinetics of magnetic field induced chain like formation which influences their magneto-optic properties [8]. Among other influencing parameters, the dipolar interaction among nanoparticles is the main driving force for particle aggregation and field induced structural transitions [9]. Common methods of synthesis of ferrofluids employ co-precipitation [10], ball milling [11], sol-gel method [12] and micro emulsion [13]. Among these methods, co-precipitation is the low cost and less energy required for synthesis of ferrofluids.

2. Sample preparation

The chemical co-precipitation method was used to synthesize $Co_{1-x}Zn_xFe_2O_4$ nanoparticles for $x = 0.1$, 0.5 and 0.9. Stoichiometric ratios of $FeCl_{3.6}H_2O$, $CoCl_2$ and $ZnCl_2$ solution were mixed and added to NaOH solution under constant stirring. Diluted HCl was added until the pH reaches 9. In order to prevent agglomeration of the nanoparticles, oleic acid was added. The resultant precipitates were isolated by centrifugation and washed with de-ionized water, acetone and ethanol to remove impurities and then dried at 60 °C for 4 hours. Powder samples were used to carry out initial characterization such as XRD, TEM and VSM. Then, aqueous nanoferrofluids were prepared to study their magneto-optic effect.

3. Results and discussion

3.1. X-ray diffraction

The XRD pattern of the powder samples are shown in Fig. 1, which confirm the spinel structure (JCPDS no 22-1086) [14]. The crystallite size for each composition was calculated using the Debye-Scherer formula for the (311) plane. The crystallite size decreases from 11.4 nm to 5.6 nm with an increase in zinc content. In spinel ferrite, zinc ions have stronger preference to occupy tetrahedral site, iron ions preferentially occupy tetrahedral site while cobalt ions have octahedral site preference [15]. Increasing x values in $Co_{1-x}Zn_xFe_2O_4$ spinel ferrite causes zinc ions to occupy tetrahedral sites preferentially, displacing iron ions from the octahedral sites [16]. Therefore, replacement of cobalt ions by zinc ions forces the transformation of inverse spinel into normal spinel structure.

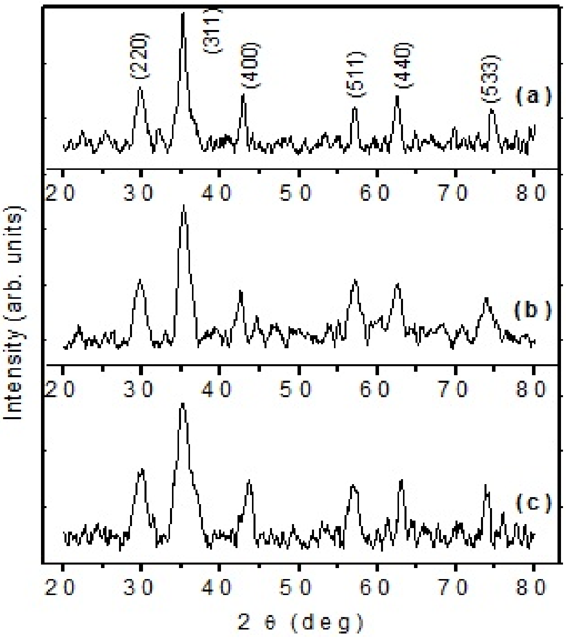

FIG. 1. XRD pattern of the samples (a) $Co_{0.9}Zn_{0.1}Fe_2O_4$, (b) $Co_{0.5}Zn_{0.5}Fe_2O_4$ and (c) $Co_{0.1}Zn_{0.9}Fe_2O_4$

3.2. Transmission electron microscopy

Figure 2 shows the transmission electron microscope (TEM) images of $Co_{1-x}Zn_xFe_2O_4$ nanoparticles. Physical particle sizes of the samples are found to be slightly larger than the crystallite size obtained by XRD. It was also observed that the presence of surfactant and decrease in the magnetic moment of particles reduced magnetic nanoparticle aggregation.

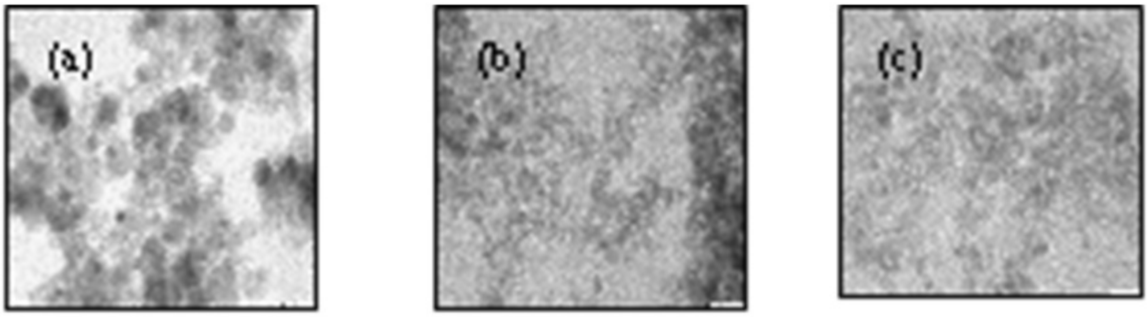

FIG. 2. TEM of the samples (a) $Co_{0.9}Zn_{0.1}Fe_2O_4$, (b) $Co_{0.5}Zn_{0.5}Fe_2O_4$ and (c) $Co_{0.1}Zn_{0.9}Fe_2O_4$

3.3. Magnetic measurements

M-H loop of the powder samples are shown in Fig. 3. Magnetization in a spinel ferrite arises as a result of dominant interaction existing between tetrahedral (A) site and octahedral (B) site mediated by oxygen A-O-B interactions [17]. Increasing zinc content in $Co_{1-x}Zn_xFe_2O_4$ spinel ferrite causes zinc ions to occupy tetrahedral sites and displaces iron ions to octahedral sites [16]. In octahedral sites, cobalt ions are replaced by iron ions [18]. Thus, the substitution of non-magnetic zinc ion varies the A-O-B interaction. Magnetic parameters, such as saturation magnetization (M_s), remanent magnetization (M_r) and coercive field (H_c), were found to vary with zinc content and are shown in Table 1. The values are in agreement with the literature [19]. Moreover, saturation magnetization of bulk cobalt ferrite is 65 emu/g [20]. Coercivity is a measure of magnetocrystalline anisotropy of

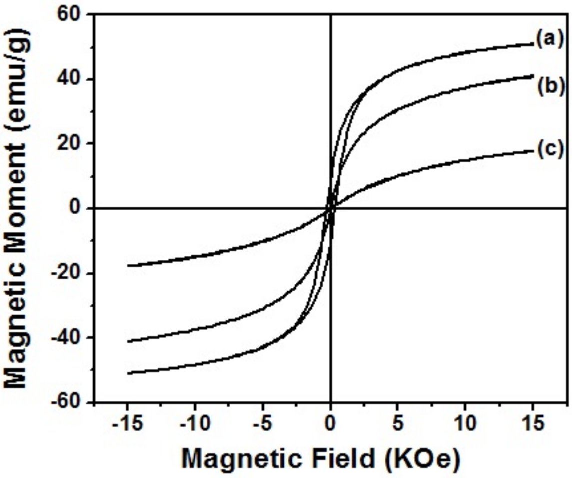

FIG. 3. M-H loop at room temperatureof the samples (a) $Co_{0.9}Zn_{0.1}Fe_2O_4$, (b) $Co_{0.5}Zn_{0.5}Fe_2O_4$ and (c) $Co_{0.1}Zn_{0.9}Fe_2O_4$

the samples [17]. Decreasing values of coercivity and remanence at room temperature indicate that the samples are approaching superparamagnetism [21]. Surface defects, such as formation of dead layer, canting of particle surface spins and deviation in cation distribution may reduce the magnetic properties [15].

TABLE 1. Magnetic parameter of the samples

Samples	Saturation Magnetization (emu/g)	Remanent Magnetization (emu/g)	Coercive Field (KOe)
$Co_{0.9}Zn_{0.1}Fe_2O_4$	50.95	9.4350	0.2878
$Co_{0.5}Zn_{0.5}Fe_2O_4$	41.04	0.0638	0.0044
$Co_{0.1}Zn_{0.9}Fe_2O_4$	17.89	0.0046	0.0013

3.4. FaradayrRotation

Faraday rotation of the samples was measured using standard technique, which includes electromagnet, polarizer, analyzer, cuvette and a monochromatic sodium vapor lamp. $Co_{1-x}Zn_xFe_2O_4$ nanoparticles were dispersed in de-ionized water and sonicated for 30 minutes. The volume fraction was kept as 0.005 for all the samples. Linearly polarized light from a polarizer was allowed to pass through the electromagnet, ferrofluid and an analyzer. In this set-up, a magnetic field applied is longitudinal to the polarized light. Light emerging out from analyzer was detected using a photodetector. The angle of rotation (θ_F) of plane polarized light is proportional to the product of applied magnetic field (B) and optical path length (l) of the ferrofluid through which the light passes:

$$\theta_F = VBl,$$

where, V is Verdet constant of the sample.

When a magnetic field is applied to the samples, degeneracy is lifted and the relative energies are determined by Lande g factor. During the transition of electrons between degenerate states, rotation of plane of polarization is accompanied by the development of an ellipticity of the originally polarized light [22]. Also, it was reported that Faraday rotation can be enhanced due to crystal field transitions and intervalence charge transfer transitions between neighboring ions [22,23]. Varying the occupancy of tetrahedral and octahedral sites changes the Faraday rotation. The variation of Faraday rotation and Verdet constant are shown in Fig. 4 and Fig. 5. Variation of Verdet constant below 600 gauss for samples (a) and (b) indicates the need to increase the accuracy of measurement system at low fields.

4. Conclusion

$Co_{1-x}Zn_xFe_2O_4$ nanoparticles were synthesized by co-precipitation method using oleic acid as surfactant. The XRD diffraction patterns confirm the cubic spinel structure. The crystallite size decreases with increased zinc

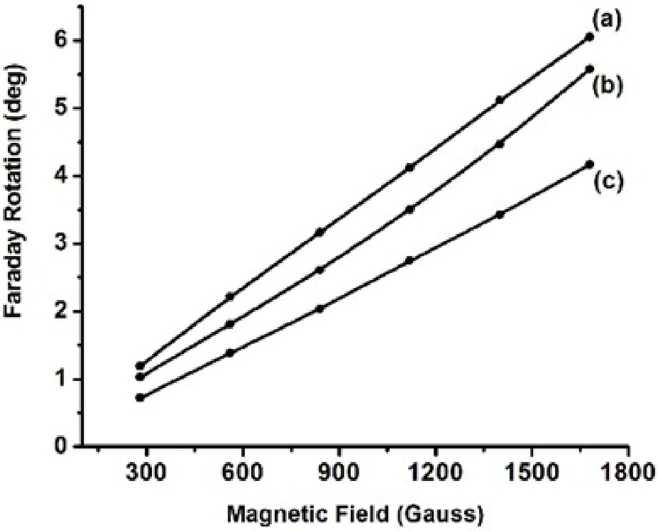

FIG. 4. Faraday rotation of the samples (a) $Co_{0.9}Zn_{0.1}Fe_2O_4$, (b) $Co_{0.5}Zn_{0.5}Fe_2O_4$ and (c) $Co_{0.1}Zn_{0.9}Fe_2O_4$

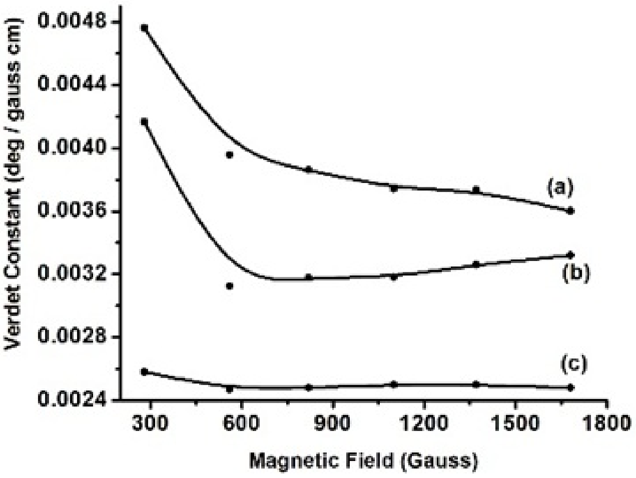

FIG. 5. Verdet constant vs magnetic field of the samples (a) $Co_{0.9}Zn_{0.1}Fe_2O_4$, (b) $Co_{0.5}Zn_{0.5}Fe_2O_4$ and (c) $Co_{0.1}Zn_{0.9}Fe_2O_4$

content. The magnetic properties and Verdet constant of $Co_{1-x}Zn_xFe_2O_4$ nanoparticles vary with the incorporation of zinc and cobalt ions into iron oxide spinel ferrite. The Faraday rotation and hence the Verdet constant decreases with increased zinc substitution.

Acknowledgement

The authors would like to thank SAIF, IIT Bombay for providing TEM facility.

References

[1] Ibrahim Sharifi, Shokrollai H., Amiri S. Ferrite based magnetic nanofluids used in hyperthermia applications. *Journal of Magnetism and Magnetic Materials*, 2012, **324**(6), P. 903–915.

[2] Masajada J., Bacia M., Drobczyński S. Cluster formation in ferrofluids induced by holographic optical tweezers. *Optics Letters*, 2013, **38**(19), P. 3910–3913.

[3] Bhatt H., Patel R. Optical transport in bidispersed magnetic colloids with varying refractive index. *Journal of nanofluids*, 2013, **2**(3), P. 188–193.

[4] Mahendran V., Philip J. Nanofluid based optical sensor for rapid visual inspection of defects in ferromagnetic materials. *Applied Physics Letters*, 2012, **100**(7), P. 073104.

[5] Fan C.Z., Wang G., Huang J.P. Magnetocontrollable photonic crystals based on colloidal ferrofluids. *Journal of Applied Physics*, 2008, **103**(9), P. 094107.

[6] Duncan P.D., Camp P.J. Aggregation kinetics and the nature of phase separation in two-dimensional dipolar fluids. *Physical Review Letters*, 2006, **97**(10), P. 107202.

[7] Ukai T., Maekawa T. Patterns formed by paramagnetic particles in a horizontal layer of a magnetorheological fluid subjected to a dc magnetic field. *Physical Review E*, 2004, **69**(3), P. 032501.

[8] Regmi R., Black C., Sudakar C., Keyes P.H., Naik R., Lawes G., Vaishnava P., Rablau C., Kahn D., Lavoie M., Garg V.K., Oliveira A.C. Effects of fatty acid surfactants on the magnetic and magnetohydrodynamic properties of ferrofluids. *Journal of Applied Physics*, 2009, **106**(11), P. 113902.

[9] Brojabasi S., Muthukumaran T., Laskar J.M., John Philip. The effect of suspended Fe_3O_4 nanoparticle size on magneto-optical properties of ferrofluids. *Optics Communications*, 2015, **336**, P. 278–285.

[10] Amighian J., Karimzadeh E., Mozaffri M. The effect on Mn^{2+} substitution on magnetic properties of $Mn_xFe_{3-x}O_4$ nanoparticles prepared by coprecipitation method. *Journal of Magnetism and Magnetic Materials*, 2013, **332**, P. 157–162.

[11] Yin H., Too H.P., Chow G.M. The effects of particle size and Surface coating on the cytotoxicity of nickel ferrite. *Biomaterials*, 2005, **26**(29), P. 5818–5826.

[12] VijayaBhasker Reddy P., Ramesh B., GopalReddy Ch. Electrical conductivity and dielectric properties of zinc substituted lithium ferrites prepared by sol-gel method. *Physica B*, 2010, **405**(7), P. 1852–1856.

[13] Woo K., Lee H.J., Ahn J.P., Park Y.S. Sol-gel mediated synthesis of Fe_2O_3 naorods. *Advanced Materials*, 2003, **15**(20), P. 1761–1764.

[14] Bragg W.H. The Structure of magnetite and the Spinels. *Nature*, 1915, **95**(2386), P. 561.

[15] BehshidBehdafar, Ahmad Kermanpur, HojjatSadeghi-Aliabadi, Maria del Puerto Morales, MortezaMozaffari. Synthesis of aqueous ferrofluids of $Zn_xFe_{3-x}O_4$ nanoparticles by citric acid assisted hydrothermal-reduction route for magnetic hyperthermia applications. *Journal of Magnetism and Magnetic Materials*, 2012, **324**(14), P. 2211–2217.

[16] VeenaGopalan E., Al-Omari I.A., Malini K.A., Joy P.A., Sakthi Kumar D., Yasuhiko Yoshida, Anantharaman M.R. Impact of zinc substitution on the structural and magnetic properties of chemically derived nanosized manganese zinc mixed ferrites. *Journal of Magnetism and Magnetic Materials*, 2009, **321**(8), P. 1092–1099.

[17] Yüksel Köseoğlu. Structural, magnetic, electrical and dielectric properties of $Mn_xNi_{1-x}Fe_2O_4$ spinel nanoferrites prepared by PEG assisted hydrothermal method. *Ceramics International*, 2013, **39**(4), P. 4221–4230.

[18] López J., González-Bahamón L.F., Prado J., Caicedo J.C., Zambrano G., Gómez M.E., Esteve J., Prieto P. Study of magnetic and structural properties of ferrofluids based on cobalt-zinc ferrite nanoparticles. *Journal of Magnetism and Magnetic Materials*, 2012, **324**(4), P. 394–402.

[19] Vaidyanathan G., Sendhilnathan S., Arulmurugan R. Structural and magnetic properties of $Co_{1-x}Zn_xFe_2O_4$ nanoparticles by coprecipitation method. *Journal of Magnetism and Magnetic Materials*, 2007, **313**(2), P. 293–299.

[20] Yeongll Kim, Don Kim, Choong Sub Lee. Synthesis and characterization of $CoFe_2O_4$ magnetic nanoparticles prepared by temperature-controlled coprecipitation method. *Physica B: Condensed Matter*, 2003, **337**(1-4), P. 42–51.

[21] Mathew D.S., Juang R.S. An overview of the structure and magnetism of spinel ferrite nanoparticles and their synthesis in microemulsions. *Chemical Engineering Journal*, 2007, **129**(1-3), P. 51–65.

[22] Prashant K. Jain, Yanhong Xiao. Ronald Walsworth and Adam E. Cohen. Surface Plasmon resonance enhanced magneto-optics (SuPREMO): Faraday rotation enhancement in gold coated iron oxide nanocrystals. *Nano Letters*, 2009, **9**(4), P. 1644–1650.

[23] Choi K.H. Magnetic behavior of Fe_3O_4 nanostructure fabricated by template method. *Journal of Magnetism and Magnetic Materials*, 2007, **310**(2), P. e861–e863.

NANOSYSTEMS: PHYSICS, CHEMISTRY, MATHEMATICS, 2016, 7 (4), P. 629–632

Preparation and characterization of porous silicon photoelectrode for dye sensitized solar cells

K. Gangadevi[1], K. Ramachandran[2], R. Srinivasan[1,*]

[1]Department of Physics, Thiagarajar College, Madurai–625009, India

[2]School of Physics, Madurai Kamaraj University, Madurai–625021, India

kdevi.ganga@gmail.com, thirumalchandran@gmail.com, *r_srini2067@yahoo.co.in

PACS 81.05.Rm, 82.33.Ln, 88.40.jr, 88.40.hj, 78.55.Mb

DOI 10.17586/2220-8054-2016-7-4-629-632

Nanostructured porous silicon (PS) samples were prepared by electrochemical anodic dissolution of doped silicon (p-Si) of (100) orientation at constant current density of 30 mA/cm^2 for different etching times 10 and 60 min. The samples were characterized by XRD and SEM. The particle size was calculated from XRD using Scherrer's approximation are in the range of 12 to 61 nm and the SEM images confirmed the difference in porosities of the sample. The samples were sensitized with chloroaluminium phthalocyanine (ClAlPc) to fabricate Dye-sensitized solar cells (DSSCs). The bandgaps from UV- Vis and photoluminescence measurements are in the range of 1.5 to 1.8 eV. The photocurrent and photovoltage of the cells were measured using Keithely source meter. The maximum conversion efficiency of 2.8% is observed and results are discussed.

Keywords: Porous silicon, Chloroaluminum Pc, dye sensitized solar cells, photoluminescence.

Received: 5 February 2016

Revised: 10 May 2016

1. Introduction

Dye-sensitized solar cells (DSSCs) are regarded as a promising low cost option to the conventional solid-state semiconductor solar cells, due to the use of relatively cheap materials and the easy manufacturing techniques. A very important component of DSSCs is the photoelectrode, which includes a nanocrystalline porous wide bandgap oxide semiconductor layer with large internal surface area. The Commercial solar cells are fabricated using crystalline silicon which is costly in nature, where the maximum efficiency of 24.5% is reported in literature [1]. In this work, we measured the conversion efficiencies of DSSCs prepared from porous silicon with different porosities.

2. Experimental

Porous silicon samples were prepared by electrochemical etching of p-type (100) silicon wafers (thickness 517 μm and resistivity 0.2–0.5 Ω cm) at a constant current density of 30 mA/cm^2 for etching periods of 10 and 60 minutes [2]. To sensitize the porous samples, the dye solution was prepared by mixing the synthesized ClAlPc dye [3] in 5 ml of ethanol and used for preparation of photoanode (ClAlPc/PS). The photoanodes were characterized by X–Ray Diffraction (XRD), Scanning Electron Microscopy (SEM), Ultraviolet-visible spectroscopy (UV-vis) and Photoluminescence (PL) techniques. The ClAlPc/PS photoanodes with different porosities were used to fabricate DSSCs.The I–V measurements were carried out to calculate the solar efficiencies using Keithley Source Meter 2400.

3. Results and discussion

3.1. XRD measurement

The XRD patterns of PS and ClAlPc/PS prepared at constant current density of 30 mA/cm^2 with etching times 10 and 60 min is shown in Fig. 1 A and B respectively.

In Fig. 1A, the characteristic peaks at 2θ = 24.82° and 64.77° depict the porous nature of silicon, which are identified as (111) and (404) plane respectively and are in agreement with JCPDS (27-1402) values [4]. The peak 2θ = 6.31° for ClAlPc in Fig. 1B agrees well with the reported value [5] and identified as the (2 0 0) plane of α–phase structure and the lattice spacing d = 12.88 Å. Additionally, it is noted that the intensities of the peaks increase with etching time and hence the porosity, as the porosity increases with etching time [6]. The broadened

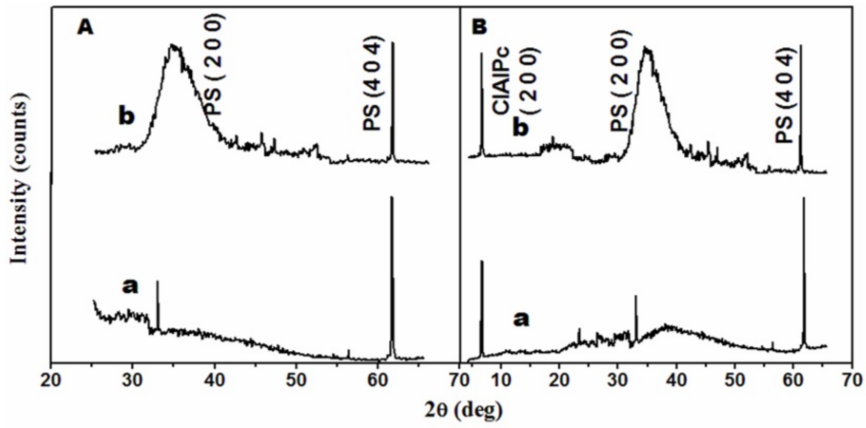

FIG. 1. XRD Pattern of the samples prepared at 30 mA/cm^2 for (a) 10 min (b) 60 min: (A) PS (B) ClAlPc/PS

peak shown by the sample prepared at 30 mA/cm^2, 60 min indicates that it is more nanostructured in nature. The crystallite sizes calculated from Scherrer's approximation are in the range from 12 to 61 nm.

3.2. Scanning electron microscope

The SEM image of the PS sample is shown in Fig. 2. The porosity of the sample increases with increasing etching time [6]. The porosities calculated from gravimetric method were shown to range from 55% to 78%.

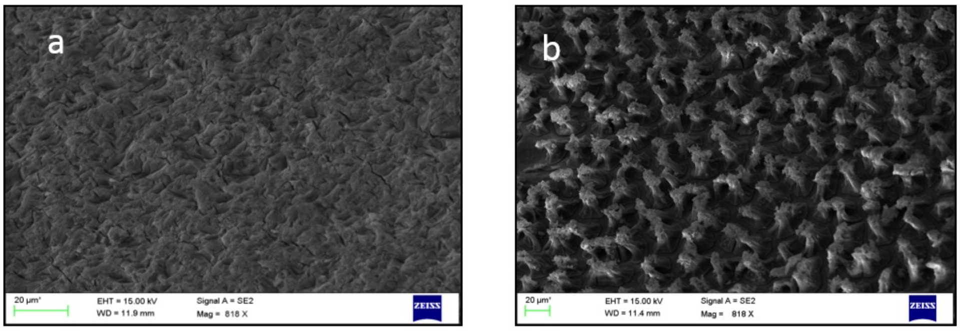

FIG. 2. SEM image of PS samples prepared at 30 mA/cm^2 for etching time (a) 10 min (b) 60 min

3.3. Optical measurements

The optical band gap measurements were carried out using UV absorption and PL emission for PS and ClAlPc/PS samples at room temperature. The PL emission spectra of PS and ClAlPc/PS samples are shown in Figs. 3A and 3B respectively. The calculated band gaps from PL and UV measurement are shown in Table 1. The values are in good agreement with each other.

The band gaps of the PS samples are blue shifted from the bulk silicon (1.1 eV). Also, the band gaps of the PS samples are slightly blue shifted with increased etching time. This shift in band gap (band gap widening) is because of quantum confinement due to reduction in the size of the Si nanocrystallites for increased etching time [7]. The decrease in crystallite size is attributed to the increase in porosity with increased etching time [8]. The PL intensity of the PS samples increases with increasing etching time due to the increase in the total volume of the nanocrystallites on the surface of the PS [9, 10].

For the dye sensitized PS (ClAlPc/PS), the PL emission is shifted to 735 nm (Fig. 3B(a)) compared to the PS sample which is attributed due to the presence of chlorine in the dye. The decrease in PL intensity shown by ClAlPc/ PS with increasing etching time is explained due to the enhanced absorption with an increase in porosity and confinement of particles into a lower dimension [11]. The minimum emission intensity shown by ClAlPc/PS at a current density of 30 mA/cm^2 with etching time of 60 min (Fig. 3B) indicates that it is a good absorber of radiation and can be used for solar cell application.

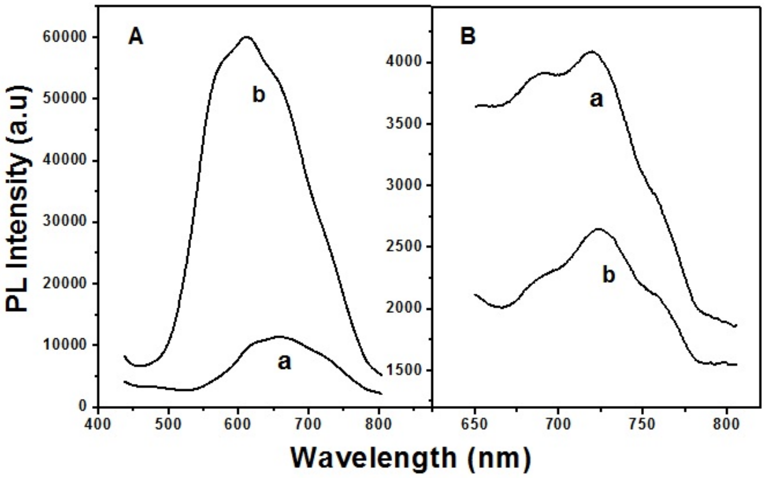

FIG. 3. Photoluminescence spectra of PS samples prepared at 30 mA/cm^2 for (a) 10 min (b) 60 min: (A) PS

TABLE 1. Bandgap of the samples

Etching time	Band gap (eV)			
	PS		ClAlPc/PS	
	PL	UV	PL	UV
a (10 min)	1.81	1.81	1.60	1.59
b (60 min)	2.02	2.05	1.76	1.77

3.4. I-V Measurements

Performance of DSSCs (1 cm^2 size) was analyzed by current–voltage (I–V) characteristics. Photocurrents and voltages were measured using a Keithely source meter 2400, with an 80 W halogen lamp and AM 1.5 G. The conversion efficiency of the samples is given in Table 2. The literature value of conversion efficiency of ClAlPc/TiO$_2$ is 2.1% [12].

TABLE 2. Conversion efficiency of the ClAlPc/PS samples (Current density 30 mA/cm^2)

	Porosity of PS (%)	Efficiency (%)
a (10 min)	55	0.84
b (60 min)	78	2.84

4. Conclusion

Nanostructured porous silicon (PS) samples were prepared at constant current density of 30 mA/cm^2 at etching times of 10 and 60 min. The samples were characterized by XRD, UV-Vis and PL emission techniques. The band gap increases with increased etching time. To study the effect of dye sensitizer, the surface of these PS samples was sensitized with derivative of Chloroaluminum Pc (ClAlPc). The dependence of absorption and emission intensities on these samples indicate that ClAlPc /PS prepared at current density of 30 mA/cm^2 with 60 min etching time is good absorber of radiations. The DSSC prepared by ClAlPc /PS shown a maximum conversion efficiency of 2.8% and can be used for solar cell applications.

Acknowledgement

The authors acknowledge the University Grant Commission (UGC), India, for financial support in the form of Major research project (F.No.41-941/2012 (SR)).

References

[1] Regan B.O., Gratzel M. Low-Cost, High Efficiency Solar Cell Based on Dye Sensitized Colloidal TiO_2 Film. *Nature*, 1991, **353**, P. 737–739.

[2] Smith R.L., Collins S.D. Porous silicon formation mechanisms. *Journal of Applied Physics*, 1992, **71**(8), P. R1–R22.

[3] Azim-Araghi M.E., Krier A. The influence of ammonia, chlorine and nitrogen dioxide on chloro-aluminium phthalocyanine thin films. *Appl. Surf. Sci.*, 1997, **119**, P. 260.

[4] Hadi H.A., Ismail R.A., Habubi N.F. Fabrication and characterization of porous silicon layer prepared by photo-electrochemical etching in CH_3OH:HF solution. *International Letters of Chemistry. Physics and Astronomy*, 2013, **3**, P. 29–36.

[5] Jafari M.J., Azim-Araghi M.E. Gholami M. Chemiresistive Electrical Properties Of Chloroaluminum Phthalocyanine Nanostructured Thin Films. *Optoelectronics And Advanced Materials*, 2012, **6**(9-10), P. 868–874.

[6] Khaldun A., Salman Z. Hassan., Khalid Omar. The effect of etching time of porous silicon on solar cell performance. *Journal of Superlattices and Microstructures – Elesvier*, 2011, **50**, P. 647–658.

[7] Azim-Araghi M.E., Karimi-Kerdabadi E., Jafari M.J. *Eur. Phys. J. Appl. Phys.*, 2011, **55**, P. 302–303.

[8] Srinivasan R., Jayachandran M., Ramachandran K. Photoacoustic studies on optical and thermal properties of p-type and n-type nanostructured porous silicon for (100) and (111) orientations. *Cryst. Res. Technol.*, 2007, **42**(3), P. 266–274.

[9] Kadhim Raheem G., Ismail Raid A., Abdulridha Wasna'a M. Structural, Morphological, Chemical and Optical Properties of Porous Silicon Prepared By Electrochemical Etching. *International Journal of Thin Films Science and Technology*, 2015, **4**(3), P. 199–203.

[10] Kim D.A., Shim J.H., Cho N.H.. PL and EL features of p-type porous silicon prepared by electrochemical anodic etching. *Appl. Surf. Sci.*, 2004, **234**, P. 256–261.

[11] Jayachandran M., Paramasivam M., Murali K.R., Trivedi D.C., Raghavan M. Synthesis Of Porous Silicon Nanostructures For Photoluminescent Devices. *Materphys. Mech.*, 2001, **4**, P. 143.

[12] Walter M.G., Rudine A.B., Wamser C.C. Porphyrins and phthalocyanines in solar photovoltaic cells. *J. Porphyrins Pthalocyanine*, 2010, **14**, P. 759–762.

NANOSYSTEMS: PHYSICS, CHEMISTRY, MATHEMATICS, 2016, 7 (4), P. 633–636

TiO_2 based dye-sensitized solar cell using natural dyes

J. Kalaivani[1], K. Renukadevi[2], K. Ramachandran[3], R. Srinivasan[1,*]

[1]Department of Physics, Thiagarajar College, Madurai–625009, India

[2]Department of Physics, G. Venkataswamy Naidu College, Kovilpatti–628502, India

[3]School of Physics, Madurai Kamaraj University, Madurai–625021, India

renu_kritto@yahoo.com, thirumalchandran@gmail.com, *r_srini2067@yahoo.co.in

PACS 88.40.hj, 83.80.Mc, 78.66.Qn **DOI 10.17586/2220-8054-2016-7-4-633-636**

Nanostructured TiO_2 thin films were prepared for various thicknesses on fluorine – doped tin oxide (FTO) conductive glass by the spin coating method. Anthocyanin dye was used to sensitize the sample. The structural characterization was done by XRD. The bandgaps from UV–Vis and photoluminescence measurements are in the range of 2.41 to 2.59 eV. The photocurrent and photovoltage of the cells was measured using Keithley source meter. A maximum conversion efficiency of 0.27 % was observed and the results were discussed.

Keywords: Dye sensitized solar cells, natural dyes, TiO_2 film.

Received: 5 February 2016

Revised: 20 June 2016

1. Introduction

Dye-sensitized solar cells (DSSC) are expected to be used for future clean energy [1, 2] and are usually composed of a dye-capped nanocrystalline porous semiconductor electrode, a metal counter electrode, and a redox electrolyte containing iodide and triiodide ions. The performance of the cell is primarily dependent on the material and quality of the semiconductor electrode and the sensitizer dye used for the fabrication of the cell. In DSSC, the sensitizer (dye) plays a key role in absorbing sunlight and transforming solar energy into electric energy. Numerous metal complexes and organic dyes have been synthesized and utilized as sensitizers. By far, the highest efficiencies for DSSC have been obtained using Ru-containing sensitizer compounds absorbed onto Nano crystalline TiO_2 reached 11–12 % [3, 4]. Although, such DSSC have provided a relatively high efficiency, they are costly, as the resources are limited in quantity. On the other hand, organic dyes are cheaper and are reported to attain efficiencies as high as 9.8 % [5]. The advantages of natural dyes include their easy availability, environmental friendliness and low cost. In this paper, we report the performance of natural anthocyanin, obtained from black rice extraction. This compound would be used as the dye, since anthocyanin has good chemical bonding with titanium dioxide [6].

2. Experimental procedure

The solvent used to extract dye was prepared by using ethanol, acetic acid and distilled water with molarity ratio about 3:2:1. The blackrice was mixed in the solvent, then the mixture was stirred at 50 °C for 30 minutes, the solution formed was filtered by filter paper, to obtain dark-red solution of anthocyanin dye. TiO_2 nanoparticles of 0.2 g is blended using an agate mortar with 0.4 ml nitric acid solution (0.1 M), 0.8 g polyethylene glycol (MW–10,000) and one drop of nonionic surfactant (Triton X–100) to obtain porous TiO_2 film on FTO plate [7]. The blending process was continued using an ultrasonic bath for 30 minutes until it forms thick paste without any clots. A piece of conductive glass (FTO) is selected and placed on a metal sheet. A scotch tape at four sides was used as masking material on the conductive layer restricts the thickness and area of the paste. Then various thicknesses of TiO_2 thin films are coated over FTO plate by spin coating method for various rpm rates (3000, 4000, 5000 and 6000). Later, the plate is sintered at 450 °C for 2 hours under thermal furnace module. The thicknesses of the sample were measured using optical thickness profilometer and the sintered TiO_2 thin films were immersed in natural dyes for 24 hours, allowing the natural dye molecules to be adsorbed onto the surface of TiO_2 nanoparticles. The DSSC photo electrode (TiO_2/anthocyanin) is ready for testing. The samples were characterized by XRD, PL and UV techniques. Finally, the DSSCs were fabricated with platinum as a counter electrode and potassium iodide as liquid electrolyte.

3. Results and discussion

3.1. Structural characterization (XRD)

Various thickness of TiO_2 on FTO plate were deposited using spin coating method and it was found that the thickness of the sample decreases with increased rpm. The XRD patterns of the samples TiO_2 and TiO_2/anthocyanin for various thicknesses are shown in Fig. 1A and 1B respectively. The thickness of the samples was measured using an optical thickness profilometer. In Fig. 1A, the characteristic peaks at 27 °(110), 37 °(301) and 54 °(211) reveal the formation of ructile phase of TiO_2 (JCPDF card No: 73-1765) [8]. The nature of XRD peaks reflect that the nanoparticles are crystalline. Furthermore, the intensity of peak corresponding to (1 1 0) plane decreases with decreased thickness (Fig. 1A). After the absorption of anthocyanin dye, the peak corresponding to the plane (2 2 1) disappears and the peak corresponding to (1 1 0) decreases due to the formation of chemical bonding between TiO_2 and anthocyanin dye molecules (Fig. 1B) [6]. The thickness and XRD parameters are listed in Table 1.

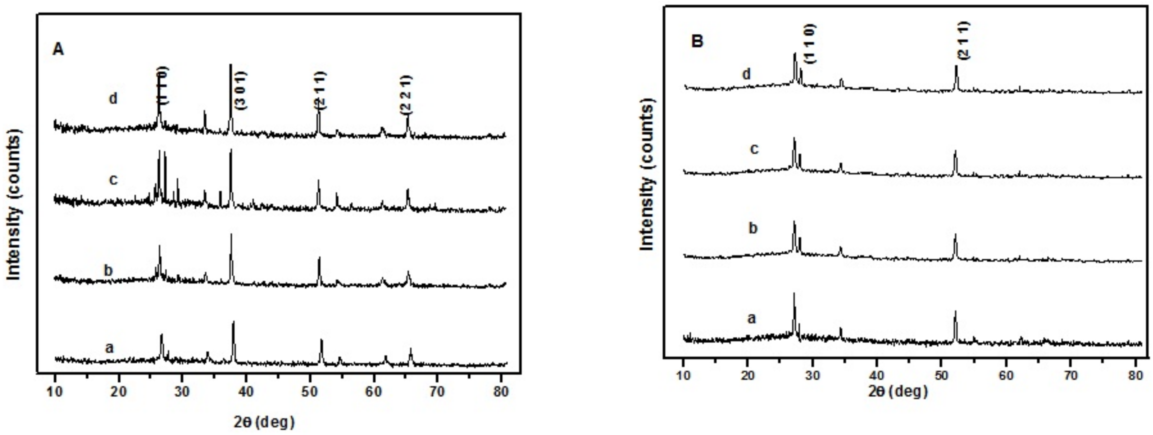

FIG. 1. XRD pattern of the samples prepared at the rpm of a) 3000; b) 4000; c) 5000; d) 6000: A) TiO_2; B) TiO_2/anthocyanin

TABLE 1. Thickness, Lattice Constant, Crystallite size of TiO_2 sample prepared at different rpm

Rotation per minute	Thickness (μm)	Lattice constant (Å)	Crystallite size (nm)
3000	18.62	4.58	27
4000	10.18	4.57	25
5000	7.36	4.56	22
6000	4.78	4.55	21

3.2. Optical measurements

The PL spectra of TiO_2/anthocyanin samples are shown in Fig. 2. The bandgaps, calculated from UV – absorption and Photoluminescence emission spectra of the samples, are given in Table 2. The bandgaps of the prepared samples (2.59 to 2.41 eV) lie in the required range of preparation for solar cells. The intensity of the PL spectra increases with increase in rpm, whereas the bandgaps of the samples decrease due to the decrease in crystallite size [9].

3.3. I–V characterization

The photovoltaic tests of the prepared DSSCs using natural dye extracts as sensitizer were carried out by I–V measurements. Photocurrents and voltages were measured using a Keithley source meter 2400, with a 80 W halogen lamp and AM 1.5 G. The quality of the solar cell is determined by a parameter called solar cell efficiency, which is simply defined by a ratio:

$$\eta = \frac{P_{max}}{P_L} \tag{1}$$

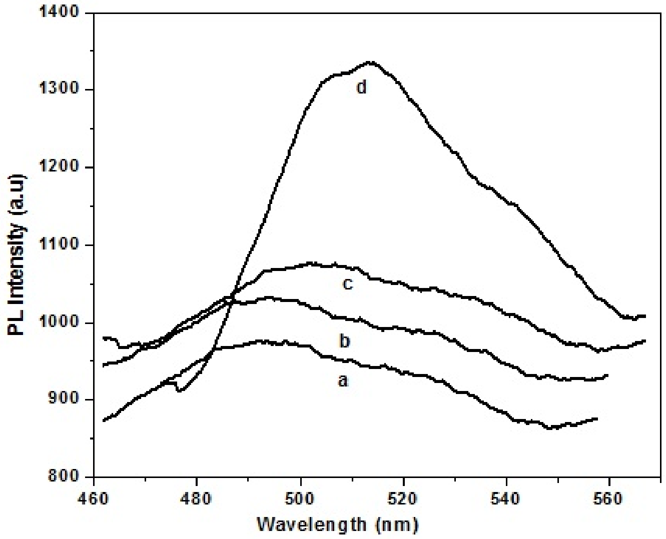

FIG. 2. PL spectra of TiO_2/anthocyanin samples prepared at the rpm of a) 3000; b) 4000; c) 5000; d) 6000

TABLE 2. Bandgap values of TiO_2/anthocyanin samples from PL and UV measurement

Rotation per minute	Band gap (eV)	
	PL	UV
3000	2.57	2.59
4000	2.52	2.52
5000	2.47	2.46
6000	2.41	2.41

where P_{max} is the maximum solar cell power and P_L is power of the incident light. Thus, solar cell efficiency and P_{max} are associated by a linear dependence. The conversion efficiencies were measured and calculated, the results are summarized in Table 3. The fill factor of the sample increases with decrease in thickness of the sample. This increase in fill factor causes increase in efficiency of the DSSCs.

TABLE 3. Conversion Efficiencies of the DSSCs prepared by Natural dyes

Rotation per minute	Thickness (μm)	Fill Factor	Conversion Efficiency (%)
3000	18.62	0.46	0.12
4000	10.18	0.58	0.13
5000	7.36	0.70	0.20
6000	4.78	4.28	0.27

4. Conclusion

The synthesized nanostructured porous TiO_2 samples were sensitized using anthocyanin dye. The structural characterization was done by XRD. The XRD pictures showed the features of TiO_2 and the effect of anthocyanin dye (blackrice). The bandgaps calculated from the UV absorption spectrum are in the range 2.41 to 2.59 eV, which is in agreement with PL measurements. The bandgap decreases with increased RPM's. The suitability of these samples for solar cell applications and sensors were studied and the samples were optimized using UV absorption. The DSSC prepared at the ratio 6000 rpm showed the highest efficiency of 0.27 %.

References

[1] Grätzel M. Dye-sensitized Solar cells. *J. Photochem. Photobiol., C. Photochem. Rev.*, 2003, **4**, P. 145–153.

[2] Law M., Greene L.E., Johnson J.C., Saykally R., Yang P. Nanowire dye-sensitized solar cells. *Nat. Mater.*, 2005, **4,** P. 455–459.

[3] Chiba Y., Islam A., Watanabe Y., Komiya R., Koide N., Han L.Y. Dye-Sensitized Solar Cells with Conversion Efficiency of 11.1%. *Jpn. J. Appl. Phys.*, 2006, **45**, P. L638–L640.

[4] Buscaino R., Baiocchi C., Barolo C., Medana C., Grätzel M., Nazeeruddin Md.K., Viscardi G. A mass spectrometric analysis of sensitizer solution used for dye-sensitized solar cell. *Inorg. Chim. Acta*, 2008, **361**, P. 798–805.

[5] Zhang G., Bala H., Cheng Y., Shi D., Lv X., Yu Q., Wang P. High efficiency and stable dye-sensitized solar cells with an organic chromophore featuring a binary π-conjugated spacer. *Chem. Commun.*, 2009, P. 2198–2200.

[6] Hao S., Wu J., Huang Y., Lin J. Natural dyes as photosensitizers for dye-sensitized solar cell. *Solar Energy*, 2006, **80**(2), P. 209–216.

[7] Kim S., Lee J.K., Kang S.O., Ko J.J., Yum J.H., Fantacci S., De Angelis F., DiCenso D., Nazeeruddin Md.K., Grätzel M. Molecular Engineering of Organic Sensitizers for Solar Cell Applications. *Journal of American Chemical Society*, 2006, **128**, P. 16701–16707.

[8] Sanjay Chakane, Anisha Gokarna, Bhoraskar S.V. Metallophthalocyanine coated porous silicon gas sensor selective to NO_2. *J.Sensors and Actuators B*, 2003, **92**, P. 1–5.

[9] Azim-Araghi M.E., Karimi-Kerdabadi E., Jafari M.J. *Eur. Phys. J. Appl. Phys.*, 2011, **55**, P. 302–303.

NANOSYSTEMS: PHYSICS, CHEMISTRY, MATHEMATICS, 2016, 7 (4), P. 637–642

ZnS nanoparticles decorated graphene nanoplatelets as immobilisation matrix for glucose biosensor

G. Suganthi[1], T. Arockiadoss[2], T. S. Uma[1]*

[1]Bio products laboratory, Central Leather Research Institute, Adyar, Chennai 600 036, Tamil Nadu, India
[2]Department of physics, Madurai Kamaraj University, Madurai 625021, Tamil Nadu, India
Shugankarthick@gmail.com, arockiados@gmail.com, tsuma@clri.res.in

PACS 87 **DOI 10.17586/2220-8054-2016-7-4-637-642**

A glucose biosensor has been fabricated by using ZnS nanoparticle-substituted graphene nanosheets. Thermally exfoliated graphene nanosheets act as a suitable support for the deposition of ZnS nanoparticles. In this work, graphene was functionalized with ZnS nanoparticles by a simple chemical reduction method. The synthesized G/ZnS nanoparticles have been characterized using X-ray diffractometry (XRD), Transmission electron microscopy (TEM), scanning electron microscopy (SEM), energy dispersive spectroscopy (EDS), FT-IR techniques. Aditionally, the Glucose biosensor has been constructed by drop-casting G/ZnS over a conductive carbon support followed by the deposition of Glucose oxidase (GOx) over a G/ZnS electrode. The performance of the biosensor was investigated by an electrochemical method. The resultant bioelectrode retains its biocatalytic activity and offers fast, highly-sensitive glucose quantification and a shelf-life of about 10 weeks under refrigerated conditions.

Keywords: Glucose oxidase, ZnS nanoparticles, graphene, enzymatic, biosensor.

Received: 5 February 2016

1. Introduction

Estimation of glucose level in blood is considered as very important for patients suffering from diabetes, heart diseases, chronic kidney failure and other disorders that require continuous glucose monitoring [1, 2]. Hence, in recent years, the demand has grown in the field of medical diagnostics for simple and disposable devices that also demonstrate fast response time, user-friendliness, cost-efficiency, and are suitable for mass production [3, 4]. Biosensor technologies offer the potential to fulfill these criteria through an interdisciplinary combination of approaches from nanotechnology, chemistry and medical science. Among the various analytical methods, enzymatic methods offer several advantages in terms of rapid determination, sensitivity and selectivity [5].

The immobilization of enzymes is the most critical step in biosensor fabrication, and thus, confers many operational advantages including high selectivity and possible modulation of the catalytic properties. Carbon-based nanomaterials are popularly used in electrochemical method due to its large surface area, excellent electrical and mechanical properties for enzyme loading and direct electron transfer to obtain low detection limits [6, 7]. Glucose oxidase (GOx), a highly specific enzyme, is most widely employed of all enzyme-based glucose biosensors. It catalyzes the oxidation of glucose to gluconolactone and hydrogen peroxide.

Among the various metal nanoparticles, zinc sulfide nanoparticles are an interesting material with a high isoelectric point that allows easy immobilization of an enzyme (with a low Isoelectric point) through electrostatic interaction [8, 9]. Furthermore, its high chemical stability and non-toxic nature, as well as its biocompatibility and high electron transfer capability make ZnS a promising material for building an enzymatic sensor by immobilizing the appropriate biomolecules without electron mediators [10, 11].

Graphene, a nanostructure of carbon, is a two-dimensional honeycomb crystalline single layer lattice of carbon [12, 13]. It has received enormous interest in various areas of research owing to its large specific surface area, extraordinary electrical and thermal conductivities, high mechanical stiffness, good biocompatibility and low manufacturing cost. The biocompatibility, high conductivity, and the large surface area of graphene have made it an ideal candidate in the development of bio-electronic devices. The large surface area and excellent electrical conductivity of graphene allow it to act as an “electron wire” between the redox centers of an enzyme or protein and an electrode’s surface. Rapid electron transfer facilitates accurate and selective detection of biomolecules [14, 15].

Currently, a wide variety of electrode devices are available for electrochemical determination. Toray Carbon paper (GDL) has received much attention in several electrochemical applications such as biofuel cells, super-capactiors, batteries and biosensors, owing to its large surface-volume ratio, high porosity and good electrical conductivity [16].

Herein, we present the design and fabrication of Carbon paper (CP) macro-substrate/Graphene(G)/ZnS based electrodes. The results show good performance, fast response times, nice stability and reproducibility, and low detection limits for the ZnS/G nanocomposite based on the reduction of H_2O_2 by immobilized glucose oxidase on the composite.

2. Materials and Methods

2.1. Materials

Glucose oxidase (GOD, type x-s from Aspergillus niger), D-(+)-glucose, Flake graphite powder (99.99 % SP-1, Bay carbon, average particle size 45 mm), were purchased from Sigma Aldrich. Carbon paper (TGPH-60) was obtained from Toray Ind., Hydrogen peroxide (H_2O_2, 30 % wt/V) was purchased from Fisher scientific. Concentrated sulfuric acid (H_2SO_4, 99 %), concentrated nitric acid (HNO_3, 98 %), potassium permanganate ($KMnO_4$) were obtained from Rankem Chemicals, India and used without further purification. Zinc sulfide nanoparticles were prepared by an aqueous chemical method using zinc chloride ($ZnCl_2$) and Sodium Sulfide (Na_2S). 0.1M phosphate buffer solution (PBS, pH 7) prepared using were prepared by mixing stock standard solution of K_2HPO_4. The aqueous stock solution of KH_2PO_4 was prepared using deionized water (DI water). The common chemicals used for the preparation of buffers, etc., were of analytical reagent grade. All the electrochemical studies and synthesis were performed using deionized (DI) water.

2.2. Synthesis of Graphene (G)

Graphene was synthesized according to thermal exfoliation method using GO as the precursor [12]. Thermal exfoliation was done in a quartz tube at 800 °C. For dispersing metal nanoparticles over graphene, the as-prepared graphene (G) was functionalized by continuous stirring in a solution of concentrated sulfuric and nitric acids (3:1) for 30 min.

2.3. Synthesis of ZnS/G nanocomposite

Zinc chloride and sodium sulfide was taken such that the ratio between the ZnS produced and the f-G is 3:7. In a typical preparation, functionalized graphene and 1 M zinc chloride was prepared in 100 ml of deionized water. Then solution of 1 M sodium sulfide was added dropwise to the magnetically stirred mixture at 70 °C, which resulted in formation of ZnS/f-G nano-colloid. The suspension was filtered and washed several times with DI water and finally the residue was dried in a vacuum oven at 60 °C.

2.4. Materials characterization techniques

The crystallinity of the synthesized material was characterized by X-ray diffraction technique using PANalytica X'pert pro X-ray diffractometer with Cu-Kα as the X-ray source. The surface morphology of the sample was examined by SEM (FEI, Quanta 3D) and TEM (TECNAI G F20,S-TWIN). Electrochemical studies were carried out by CH Instrument, electrochemical workstation with a three-electrode electrochemical cell comprising a ZnS/G modified carbon paper electrode as the working electrode, a Pt wire as the counter electrode and a Ag/AgCl (1 M KCl solution) as the reference electrode. PBS was used as the supporting electrolyte for all the electrochemical studies at ambient temperature.

2.5. Fabrication of the Bioelectrodes

The bioelectrode was fabricated over the Carbon paper electrode (CPE). The electrode was modified by a simple drop casting method. First, 1 mg/ml graphene (G) solution was prepared by ultrasonication of 1 mg of G in 1 ml of 0.5 % nafion solution. Nafion gives better dispersion as well as stability to the graphene (G). About 15 μl of the solution was dropped over the surface of carbon paper electrode and allowed to dry at room temperature. 10 μl of GOD was film cast over the dried G film. Finally, another 5 μl layer of NA was dropped and allowed to dry and kept at 4 °C to preserve the enzyme activity. The similar procedure was used for fabricating ZnS/G electrode. The fabricated electrodes will be termed as f-G/GOD/NA/CPE and Au/f-G/GOD/NA/CPE from here onward.

3. Results and discussion

3.1. XRD and FT-IR studies of the samples

The XRD pattern of the hybrid composite has been compared with the starting material. Fig. 1 depicts the XRD pattern of (a) ZnS and (b) ZnS-G. Well resolved crystalline peaks appear at 13.15 °, 21.8 °, 26.6 °, 31.6 °, 40.5 ° and 55 ° corresponding to ZnS nanoparticles [10]. Fig. 1(b) shows the diffraction peaks appear at 29.0 °, 33.5 °, 48.1 ° and 57.0 ° (JCPDS No. 05-0566) corresponding to ZnS nanostructure along with C (002) peak. This indicates the successful functionalization of graphene with ZnS nanoparticles.

The compatibility study was carried out using a Perkin Elmer FTIR spectrophotometer in the region of 4000 to 500 cm^{-1}. Spectra for ZnS, graphene and their admixture were obtained and compared. In the Fig. 2(b) FTIR spectra exhibit strong bands appearing in 643, 947, 1129, 1410, 1629 and 3419 cm^{-1}, corresponding to ZnS nanoparticles [11]. The peak at 612 cm^{-1} is assigned to the ZnS band (i.e., corresponding to sulfides). The O–H bending region due to absorbed water appear at 1629 cm^{-1} and O–H stretching at 3419 cm^{-1}. From FT-IR spectroscopy shown in Fig. 2(c), it is clear that several types of functional groups, particularly carbonyl and hydroxyl groups have been generated on acid-oxidized graphene sheet surfaces as expected [13]. Examination on surfaces of acid oxidized graphene was carried out using a Fourier transform infrared (FT-IR) spectrophotometer to ensure formation of desired surface functional groups. The absorption spectra at 3441 cm^{-1} exhibit OH stretching and OH-bending at 1624 cm^{-1}. Hence, the information provided there indicates uniform distribution of ZnS nanoparticles on the graphene surface.

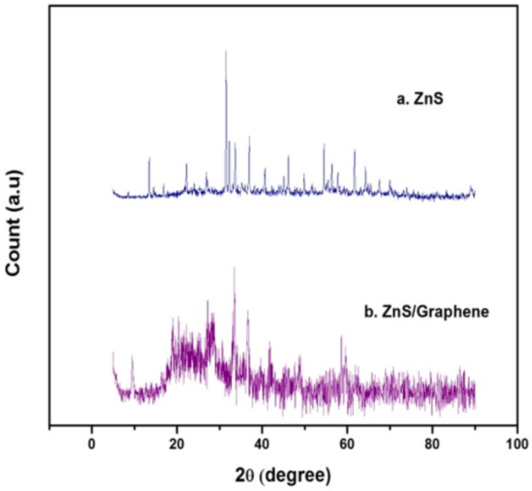

FIG. 1. XRD of ZnS and ZnS/Graphene

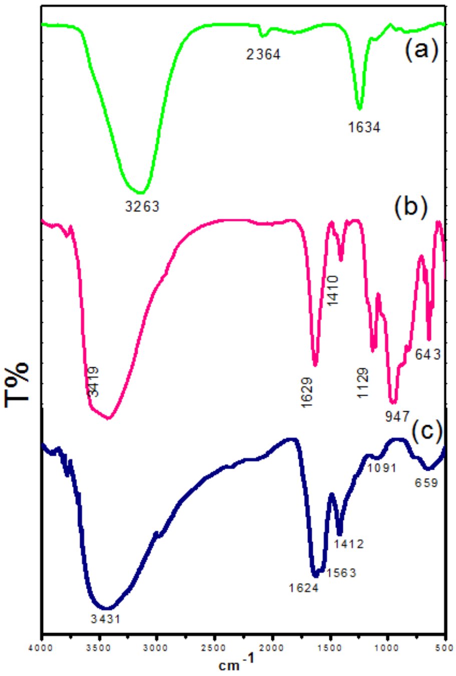

FIG. 2. FTIR spectra of (a) ZnS/G (b) ZnS and (c) G

3.2. SEM and TEM analysis of the samples

The surface morphology of the samples was studied by electron microscopy. SEM and TEM images of G and ZnS/G composites at different resolutions reveal the 2D structure of G sheets and the uniform distribution of ZnS nanoparticles on the surface of G with low and high magnification, as shown in Figs. 3 & 4. Energy dispersive X-ray analysis (EDX) results demonstrate the presence of ZnS in the corresponding samples [10].

Figure 5(a) illustrates that EDX of graphene shows the weight percentage of carbon 93.64 % and oxygen 06.36 % and Fig. 5(b) shows the edax of ZnS decorated graphene nanocomposites shows the weight percentage of carbon 71 %, oxygen 3 %, Zinc 22 % and Sulphur 4 % present in the corresponding samples.

The EDX results explains the composition of elements such as C, O, S and Zn for the corresponding samples and discussed above.

3.3. Electrochemical activity towards H_2O_2

The collective electro-catalytic effect of nanoparticles and graphene towards H_2O_2 is well-documented in the literature. In the present study, the enzymatic generation of hydrogen peroxide is achieved in the reaction layer of the G or (G/ZnS) film. In order to investigate the electro-catalytic performance towards the electrochemical reaction of hydrogen peroxide at the G or (G/ZnS) film, cyclic voltammetry (CV) has been performed. The CVs with ZnS and G/ZnS film modified CPE before and after addition of 10 μM H_2O_2 in 0.1 M phosphate buffer solution (pH 7) are shown in Figs. 6 and 7. The two electrodes show only a small background current in the

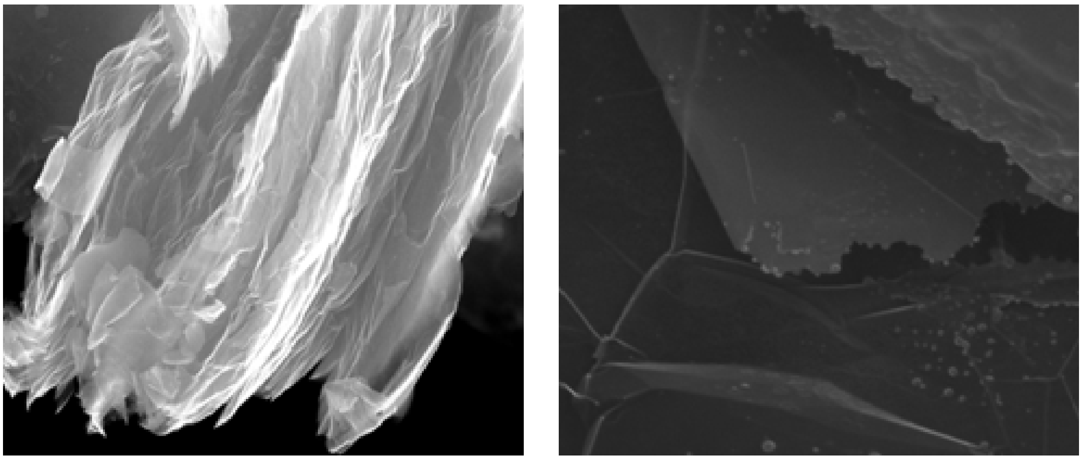

(A) (B)

FIG. 3. SEM images of (A) G and (B) ZnS/G

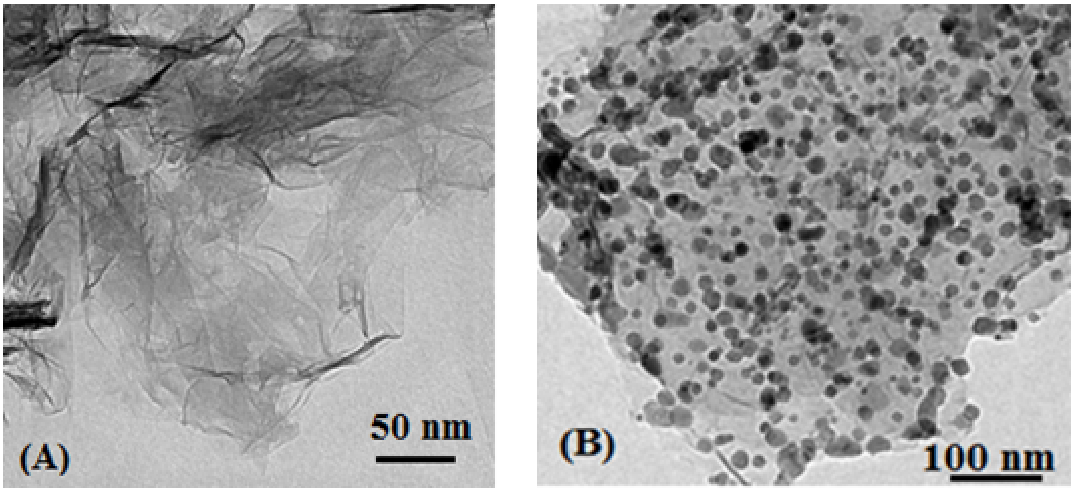

FIG. 4. TEM Images of (A) G and (B) ZnS/G

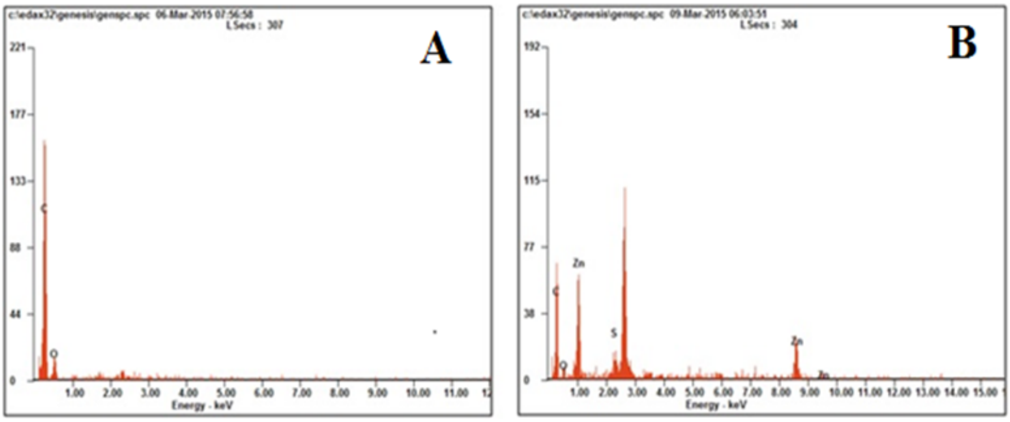

FIG. 5. EDX spectra of (A) G and (B) ZnS/G

absence of hydrogen peroxide. Upon addition of hydrogen peroxide, the CV of G/ZnS modified electrode changed with obvious increase of the current relative to that of G. A pair of well-defined redox peaks appears with G/ZnS electrode. This is due to the high electron transfer rate of the G/ZnS/GOD/NA/CP electrode, high aspect ratio and huge working surface area of the nanocomposite.

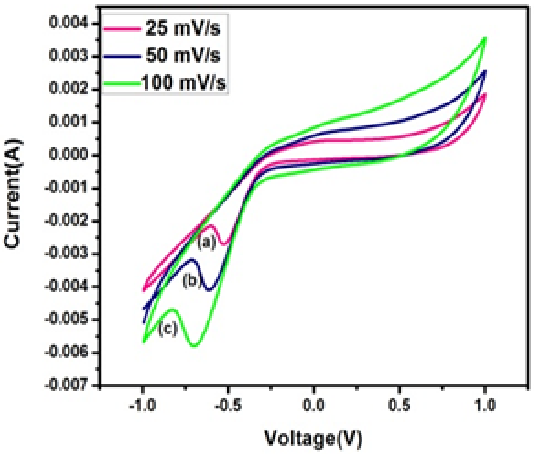

FIG. 6. CV of G/GOD/NA/CPE in 0.1 M PB solution (pH 7) containing 0.3 mM H_2O_2 at a scan rate of (a) 25 mV/s; (b) 50 mV/s; (c) 100 mV/s

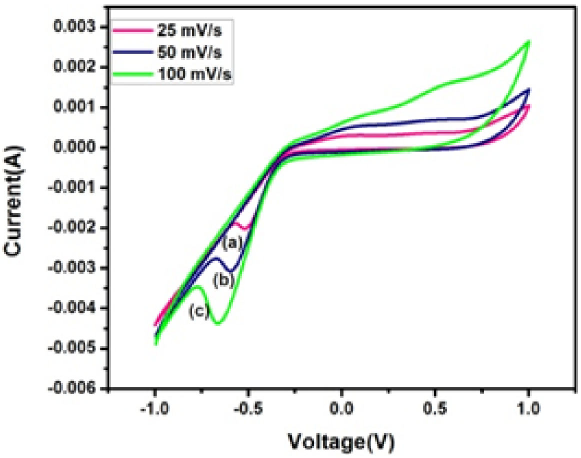

FIG. 7. CV of ZnS/G/GOD/NA/CPE in 0.1 MPB solution (pH 7) containing 0.3 mM H_2O_2 at a scan rate of (a) 25 mV/s; (b) 50 mV/s; (c) 100 mV/s

3.4. Electrochemical activity towards glucose

Figures 8 & 9 illustrates the CV responses of G/GOD/NA/CPE and G/ZnS/GOD/NA/CPE with the addition of 100 μM glucose recorded at a scan rate of 25, 50 and 100 mV/s. G/ZnS/GOD/NA/CPE exhibits a couple of redox peaks versus Ag/AgCl reference electrode, showing the potential characteristic of graphene. An increase in current has also been observed from the CV curve of ZnS/G/GOD/NA/CPE with glucose in PBS compared to ZnS/ChOx/NA/GCE with glucose in PBS. The origins of well-defined redox peaks from the CV curve of G/ZnS/GOD/NA/CP electrode in PBS with 100 μM glucose is due to the H_2O_2 generation during the oxidation of glucose by GOD. In addition to this, because of high surface area of G/ZnS, GOD attached to the surfaces of G/ZnS facilitates the fast and direct electron transfer between the active sites of immobilized GOD and electrode surface which leads to well-defined peaks. Therefore, glucose is efficiently detected with the G/ZnS/GOD/ NA/CPE.

4. Conclusions

Graphene nanosheets have been successfully substituted with ZnS nanoparticles and GOD has been immobilized on the G-ZnS/CP electrode. The incorporation of Graphene into the electrode increases the surface area and serves as an excellent support for ZnS nanoparticles that effectively catalyze redox reactions involving H_2O_2. In addition, the combination of G and ZnS nanoparticles facilitates the low potential amperometric detection of glucose and exhibits both good reproducibility and long-term stability of the biosensor, thereby providing a suitable platform for biosensor design and other biological applications.

Acknowledgements

We are grateful to The Director, CLRI, Chennai, for his kind permission to publish this work.

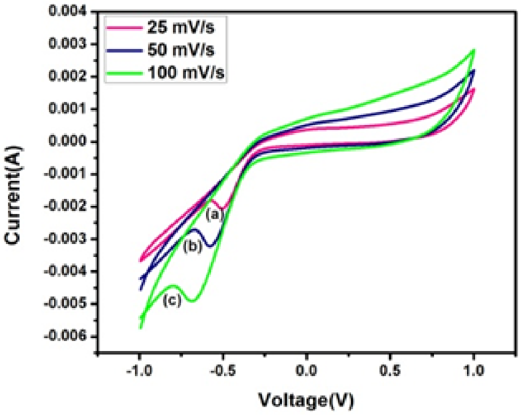

FIG. 8. CV of G/GOD/NA/CPE in 0.1 M PB solution (pH 7) containing 100 μM cholesterol at a scan rate of 25, 50 and 100 mV/s

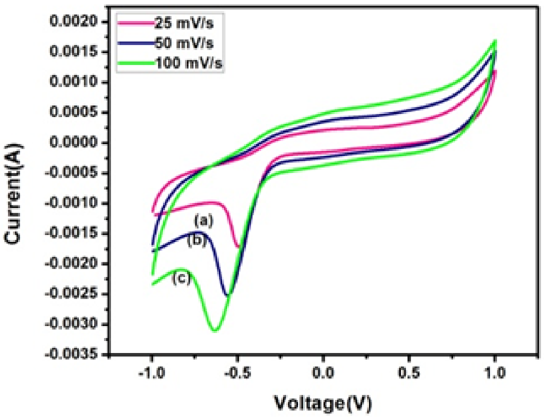

FIG. 9. CV of ZnS/G/GOD/NA/CPE in 0.1 M PB solution (pH 7) containing 100 μM cholesterol at a scan rate of 25, 50 and 100 mV/s

References

[1] Wild S., Roglic G., et al. Global prevalence of diabetes estimates for the year 2000 and projections for 2030. *Diabetes Care*, 2004, **27** (5), P. 1047–1053.

[2] American Diabetes Association. Diagnosis and classification of diabetes mellitus. *Diabetes Care*, 2003, **36** (Suppl 1), S67–S74.

[3] Bakker E., Qin Y. Electrochemical sensors. *Anal. Chem.*, 2006, **78** (12), P. 3965–3984.

[4] Luo X., Morrin A., Killard A.J., Smyth M.R. Application of nanoparticles in electrochemical sensors and biosensors. *Electroanalysis*, 2006, **18** (4), P. 319–326.

[5] Heller A., Feldman B. Electrochemical glucose sensors and their applications in diabetes management. *Chem. Rev.*, 2008, **108** (7), P. 2482–2505.

[6] Dungchai W., Chailapakul O., Henry C.S. A low-cost, simple, and rapid fabrication method for paper-based microfluidics using wax screen-printing. *Analyst*, 2011, **136** (1), P. 77–82.

[7] Nie Z.H., Nijhuis C.A., et al. Electrochemical sensing in paper-based microfluidic devices. *LabChip*, 2010, **10** (4), P. 477–483.

[8] Wang F., Hu S. Electrochemical sensors based on metal and semiconductor nanoparticles. *Microchim Acta*, 2009, **165** (2), P. 1–22.

[9] Wang J. Nanomaterial-based electrochemical biosensors. *Analyst*, 2005, **130** (4), P. 421–426.

[10] Rita J., Sasi S. Florence optical, structural and morphological studies of bean-like Zns nanostructures by aqueous chemical method. *Chalcogenide Letters*, 2010, **7** (4), P. 269–273.

[11] Xu J.F., Ji W., et al. Preparation of ZnS nanoparticles by ultrasonic radiation method. *Appl. Phys. A*, 1998, **66**, P. 639–641.

[12] Konstantin K.N., Ozbas B., et al. Raman Spectra of Graphite Oxide and Functionalized Graphene Sheets. *Nano Lett.*, 2008, **8** (1), P. 36–41.

[13] Schniepp H.C, Li J.L., et al. Functionalized single graphene sheets derived from splitting graphite oxide. *J. Phys. Chem. B*, 2006, **110** (17), P. 8535–8539.

[14] Yang W., Ratinac K.R., et al. Carbon nanomaterials in biosensors: should you use nanotubes or graphene? *Angew. Chem., Int. Ed.*, 2010, **49** (12), P. 2114–2138.

[15] Zhu Z., Garcia G.L., et al. A Critical Review of Glucose Biosensors Based on Carbon Nanomaterials: Carbon nantubes and graphene. *Sensors*, 2012, **12** (5), P. 5996–6022.

[16] Kuwahara T., Ohta H., Kondo M., Shimomura M. Immobilization of glucose oxidase on carbon paper electrodes modified with conducting polymer and its application to a glucose fuell cell. *Bioelectrochemistry*, 2008, **74** (1), P. 66–72.

NANOSYSTEMS: PHYSICS, CHEMISTRY, MATHEMATICS, 2016, 7 (4), P. 643–646

Bistable electrical switching and performance of a pentacene-based write once/read many memory device

A. G. Gayathri, C. M. Joseph

Department of Physics, Dayananda Sagar College of Engg, Shavige malleswara Hills,
Kumaraswamy layout, Bangalore-560076, India

gaythri305@yahoo.com, cmjoseph@rediffmail.com

PACS 72.80.Le, 73.61.Wp, 73.61.Ph, 85.25.Hv **DOI 10.17586/2220-8054-2016-7-4-643-646**

In this paper, the performance of a pentacene-based write once/read many memory device is reported. The IV characteristics of a pentacene device deposited at 5 Å/s on an ITO-coated glass substrate was studied. This device showed a stable switching from ON to OFF state with an ON-OFF current ratio of nearly 10^3 and a retention time of 5×10^4 s with a switching threshold voltage of 3.9 V. The irreversible switching of this device makes it suitable for write once/read many memory devices. The structural studies of pentacene thin films on glass substrate were also done and the dependence of device performance on grain size is reported. Improved performance of this device due to the addition of C_{60} layer is also discussed.

Keywords: Organic semiconductor, pentacene, thin films, vacuum thermal evaporation, WORM memory.

Received: 5 February 2016

1. Introduction

In recent years, organic memory devices with an active layer sandwiched between two electrodes have attracted much attention as future information storage devices [1–5]. The demand on organic non-volatile memory devices increases rapidly due to their simplicity in device structure, good scalability, low cost potential, low power operation and large capacity for data storage. Electrical bistable switching phenomena have been observed and reported for a variety of organic materials and device structures [1–10]. Several conductance mechanisms are also reported to explain this switching phenomenon.

Different types of organic memory devices are: random access memory, re-writable memory and write once/read many memory (WORM). WORM memory is a type of non volatile memory that is capable of storing data permanently and being read from repeatedly. Thus it is potentially applicable for permanent data storage, such as wireless identification tags, smart cards, etc. Lidan Wang et al. [11] demonstrated a non volatile organic WORM memory device based on CuPc/F_{16}CuPc p–n junction. Shengwei Shi et. al. [12] fabricated an organic electrical memory device with a simple structure based on a single layer pentacene film embedded between Al and ITO electrodes. Bin Li et. al. [13] reported the impact of electrode metals on a pentacene based WORM device. They found that devices with Fe electrodes have lower threshold voltages. However, in terms of application, organic memory devices are often characterized by their performance and materials with good reliability need to be developed.

In this work, we fabricated a write once/read many memory device with vacuum evaporated pentacene on ITO coated glass substrate with aluminium as the top electrode and the performance of the fabricated device was studied and compared with a device with an additional layer of C_{60}.

2. Experimental

Figure 1(a) shows the chemical structure of pentacene molecule. Thin films of pentacene (99.999 % source powder purchased from Aldrich) were thermally deposited onto chemically cleaned glass substrates under vacuum ($\sim 2 \times 10^{-6}$ Torr) using a HIND HIVAC coating unit (Model no. 12A4D). For the devices, films were coated on to pre-cleaned ITO coated glass substrates kept at room temperature. Source material was evaporated from a molybdenum boat at a deposition rate of 5 Å/s to get a thickness of around 90 nm. Finally, aluminium was deposited thermally at a deposition rate of 20 Å/s from a tungsten basket to complete the device as in Fig. 1(b). The deposition rates and thicknesses of the deposited thin films were controlled by a quartz crystal thickness monitor. The layered structure of the device was Glass/ITO/Pentacene (5 Å/s, 90 nm)/Al (150 nm). For comparison, a layer of C_{60} was deposited on pentacene layer at a deposition rate of 5 Å/s to get a thickness of 60 nm. The overlap between the electrodes defined the dimensions of the memory cell (9 mm^2). The distance between molybdenum source and substrate holder was about 13 cm. The electrical measurements of the fabricated device were measured using a Keithley 2400 source meter and an Agilent B1500A semiconductor device analyzer.

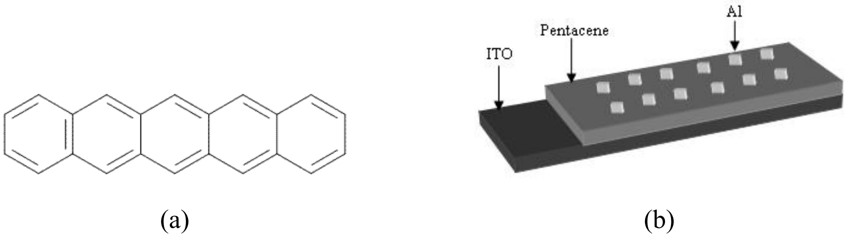

(a) (b)

FIG. 1. Chemical structure of pentacene (a) and schematic view of the fabricated pentacene device (b)

The structural studies were done using a Rigaku X-ray diffractometer. All the electrical tests were conducted at ambient conditions, without any device encapsulation and the measurements were done with a probe dimension of around 14 μm.

3. Results and discussion

3.1. Structural studies of pentacene thin films

An XRD spectrum of the pentacene thin films deposited at 5 Å/s is shown in Fig. 2. XRD pattern exhibits crystalline nature with the major diffraction peaks indexed and matches with the previous results [14, 15]. The peak was observed at $2\theta = 5.80$ which corresponds to α phase triclinic pentacene in the (001) plane. Average crystallite size was calculated using Debye-Scherrer formula [16] and was found to be 200 Å. The dislocation density was also evaluated using Williamson and Smallman's formula [16] for the deposited films and was found to be 2.5×10^{15} m^{-2}.

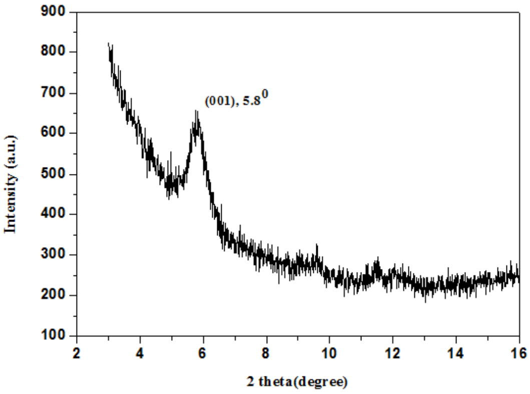

FIG. 2. X-ray diffraction patterns of pentacene thin films grown at 5 Å/s

3.2. IV characteristics of fabricated device

Figure 3(a) shows the IV plot of the device ITO/pentacene (5 Å/s)/Al for a forward and a reverse voltage sweep for 8 continuous voltage sweep cycles. The voltage was scanned from 0 V to 15 V and back to 0 V. Initially the device stayed in the high current state which is usually referred to as ON state. At a threshold voltage V_T of 3.9 V, the resistance increased suddenly from kiloohms to megaohms, indicating a sudden transition from ON state to OFF state. This hysteresis loop clearly shows the bistability of the device. The ratio of the conductivities achieved between the two states was about 10^3. After this transition, the device remained in the same state even after turning off of the power as shown in the second voltage scan. This revealed the non-volatile nature of this pentacene device. One of the important features of this device was that the switching was irreversible as reported [12, 13] and never returned to the initial off state even by applying a negative voltage pulse. This property makes it potentially suitable for a write-once/read many memory (WORM) device. For the ON state, the sweep voltage is between 0 V and 1.5 V, and the current can be measured very stably at a constant low voltage as long as the current transition has not occurred. For the high resistance state, the sweep voltage is between 0 V and 15 V.

After switching to the low current state, the device will stay in the OFF state with the next voltage sweep cycle. The voltage sweep cycles can be more for both ON and OFF states. The stability of the device under stress was evaluated in a continuous bias condition (@1V). The device showed a good performance for 5×10^4 s retention time test as shown in the Fig. 3(b).

Figure 4 compares the device performance of the device with and without C_{60} layer. Addition of C_{60} layer improved the device performance with an ON-OFF ratio 10^8 and $V_T = 3.17$ V.

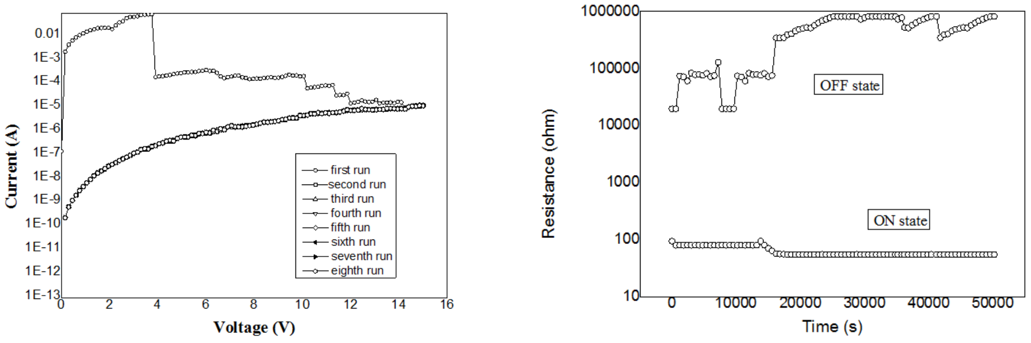

(a) (b)

FIG. 3. (a) IV characteristics of ITO/ pentacene (5 Å/s)/Al with eight continuous voltage sweep cycles. Inset shows retention time measurements both in the ON state and OFF state (@1V). (b) Retention time measurements both in the ON state and OFF state (@1V).

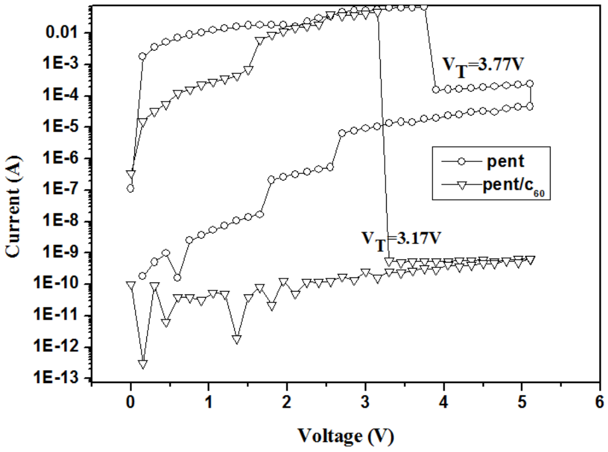

FIG. 4. Comparison of IV characteristics of ITO/Pentacene/Al and ITO/Pentacene/C_{60}/Al

The conducting mechanism of a pentacene-based WORM devices were reported earlier [11, 12]. In those devices with a structure Al/pentacene/Al, Al/pentacene/Fe and ITO/pentacene/Al, the top metal atom diffuse in to the pentacene layer under positive bias forming conductive channels responsible for high ON state. P. Aruna et al. reported the effect of fullerene doping on the electrical properties of P3HT-PCBM layers [17]. Salaoru I. et al. [6] successfully demonstrated a new donor acceptor small organic molecular pair with tetrathiafulvalene (TTF) as an electron donor and tetracyanoethylene as an electron acceptor element that determined memory behavior. The initial ON state of our devices can be explained on the basis of grain size calculation. The grain size of the films deposited at 5 Å/s was found to be more. Due to this large grain size, the metal will be diffused into the active layer, which leads to the formation of huge interface dipole layer at the electrode interface resulting in an initial high ON state. However, this interface dipole is destroyed for a large space field resulting in the decrease of the current. Addition of C_{60} layer significantly improves the device performance due to the molecular storage capability of the fullerenes, significantly enhancing the storage density capability as previously reported [5].

4. Conclusions

Bistable electrical switching of pentacene devices was studied and compared to that of a device with a C_{60} layer. The irreversible switching of these devices makes it suitable for a write once read many memory device applications. The devices with pentacene deposited at 5 Å/s showed a stable switching from low resistance state to a high resistance state. This is because as the grain size increases, the penetration of Al increases, resulting in an initial OFF state. ON-OFF ratio of the films increases from 10^3 to 10^8 with the addition of C_{60} layer. Threshold voltage decreases from 3.77 V to 3.17 V with the addition of C_{60} layer.

Acknowledgements

Financial support by Visvesvaraya Technological University (VTU), Belgaum, Karnataka, India through a grant is gratefully acknowledged. Financial support by Vision Group on Science and Technology (VGST), Department of Information Technology, Biotechnology & Science and Technology, Government of Karnataka, India through a CISE grant is also acknowledged.

References

[1] Ma L., Xu Q., Yang Y. Organic non-volatile memory by controlling the dynamic copper-ion concentration within organic layer. *Appl. Phys. Lett.*, 2004, **84**, P. 4908–4910.

[2] Pyo S., Ma L., et al. Experimental study on thickness related electrical characteristics in organic/metal-nanocluster/organic systems. *J. Appl. Phys.*, 2005, **98**, P. 054303(1–6).

[3] Ouyong J., Chu C.W., et al. Programmable polymer thin film and non-volatile memory device. *Nature materials*, 2004, **3**, P. 918–922.

[4] Konno K., Sakai H., Matsushima T., Murata H. An organic nonvolatile memory using space charge polarization of a gate dielectric. *Thin solid films*, 2009, **518**, P. 534–536.

[5] Alokik K., Shashi P., Manish C. Organic memory devices using C_{60} and insulating polymer. *Mater. Res. Soc. Symp. Proc.*, 2005, **830**, D7.2.1–D7.2.5.

[6] Salaoru I., Paul S. Memory devices based on small organic molecules donor-acceptor system. *Thin Solid Films*, 2010, **519**, P. 559–562.

[7] Li Y., Chu Y., et al. Synthesis and memory characteristics of polyimides containing noncoplanar aryl pendant groups. *Polymer*, 2012, **53**, P. 229–240.

[8] Thanh Dao T., Matsushima T., Murata H. Organic nonvolatile memory transistors based on fullerene and an electron-trapping polymer. *Org. Electronics*, 2012, **13**, P. 2709–2715.

[9] Min Kim D., Ko Y.G., et al. Digital memory behaviors of aromatic polyimides bearing bis(trifluoromethyl)-and bithiophenyl-triphenylamine units. *Polymer*, 2012, **53**, P. 1703–1710.

[10] Ling Q.D., Liaw D.J., et al. Polymer memories: Bistable electrical switching and device performance. *Polymer*, 2007, **48**, P. 5182–5201.

[11] Wang L., Su Z., Wang C. Interfacial dipole in organic p/n junction to realize write-once/read-many-times memory. *Org. Electronics*, 2013, **14**, P. 1163–1169.

[12] Shi S., Peng J., Lin J., Ma D. Write-once read-many-times memory based on a single layer of Pentacene. *Electron. Dev. Lett.*, 2009, **30**, P. 343–345.

[13] Bin L., Kao C.Y., Arthur J.E. Impact of electrode metals on a pentacene-based write-once read-many memory device. *Letter/Synth. Met.*, 2010, **160**, P. 2385–2388.

[14] Puigdollers J., Voz C., et al. Pentacene thin films obtained by thermal evaporation in high vacuum. *Thin solid films*, 2003, **427**, P. 367–370.

[15] Girtan M., Dabos-Seignon S., Stanculescu A. On morphological, structural and electrical properties of vacuum deposited pentacene thin films. *Vacuum*, 2009, **83**, P. 1159–1163.

[16] Onlaor K., Tunhoo B., et al. Electrical bistable properties of copper phthalocyanine at different deposition rates. *Solid-State Electronics*, 2012, **72**, P. 60–66.

[17] Aruna P., Suresh K., Joseph C.M. Effect of fullerene doping on the electrical properties of P3HT/PCBM layers. *Materials Science in Semiconductor Processing*, 2015, **36**, P. 7–12.

NANOSYSTEMS: PHYSICS, CHEMISTRY, MATHEMATICS, 2016, 7 (4), P. 647–649

Investigations on tri manganese tetra oxide nano particles prepared by thermal decomposition

C. Sagi Rani[1], P. Athira[1], N. Joseph John[2]

[1]Department of Physics, Noorul Islam Centre for Higher Education, Noorul Islam University,
Kumaracoil, Tamil Nadu, India
[2]Department of Physics, Govt. Arts College, The Nilgris, Tamil Nadu, India

sagirani.c@gmail.com, athira01011993@gmail.com

PACS 81.07.-b, 81.07.Bc **DOI 10.17586/2220-8054-2016-7-4-647-649**

Oxides of manganese have large number of applications in the field of sensors, piezoelectric crystals etc. In the present work, Mn_3O_4 nano materials were synthesized by using manganese acetate, adopting the method of thermal decomposition. The Nano materials thus prepared were characterized by employing various techniques like PXRD, FTIR, UV and Thermal analyses. The average particle size, calculated using Debye-Scherrer formula, was found to be in the range of 51 – 62 nm. The presence of Mn_3O_4 is also confirmed from FTIR. Thermal studies were also carried out. The optical band gap for the prepared nano materials was obtained from the UV-spectroscopic studies.

Keywords: Nano particles, thermal decomposition, PXRD, FTIR, UV, thermal studies.

Received: 5 February 2016. Revised: 31 May 2016.

1. Introduction

Nanotechnology provides the ability to create new materials or devices with new functions and properties. The current age is characterized by increased technological advances and rapid nanotechnology development [1]. Technologies with such a system of materials having at least one of its dimensions within 100 nm are referred to as nanoscience. The fundamental, physical, chemical and natural properties of materials are considerably altered as the size of their consistent grains is decreased to the nanometer scale. Most of the nanostructured materials have properties significantly different from those of the bulk materials due to the factors such as large fraction of surface atoms, high surface energy and reduced imperfections [2, 3].

It is evident that nanostructured materials are expected to have improved optical properties compared with bulk materials, as these properties depend on their size, shape and local dielectric environment [4]. In recent years, the synthesis of semiconductor materials with specific size and morphology has attracted a lot of interest due to their significant mechanical, electrical, optical and magnetic properties for potential applications in various fields [5]. Nanoscience and nanotechnology find applications in almost every branch of science and technology, electronics, astrophysics and in medical science. Recent progress in the preparation and characterization of materials on nanometer scale has introduced a new point of view for scientists in reduced dimensions. This will change the crystalline and electronic structure considerably [2].

Transition metal oxide nanoparticles are very attractive due to their variety of applications [6]. Mn_3O_4 is an important transition metal oxide due to its extensive applications in magnetic, electrochemical, lithium ion batteries, catalytic applications, super capacitors and dilute magnetic semiconductors etc. [7]. It is one of the most stable oxides of manganese [6]. Due to its nanometer size and large surface area, different morphologies are expected to display better performance in all the above mentioned applications [6]. The optical properties are the most fascinating and very useful properties of nano metal oxides. Oxides of manganese have optical properties which are associated with the intrinsic and extrinsic effect. The optical transition between the electrons in the conduction band and holes in the valence band causes the intrinsic effect. Mn_3O_4 is a direct band gap semiconductor and a transparent conducting material. By using a large number of techniques such as optical absorption, photo-reflection, photoluminescence etc. the optical transitions can be widely used in variety of applications.

In the present study, Mn_3O_4 nanoparticles were prepared using the thermal decomposition technique. Manganese oxide nanoparticles are water insoluble, brownish black powder and have no odor. Mn_3O_4 has the spinel structure [3], where the oxide ions are cubically closed packed and the Mn^{II} ions occupy tetrahedral sites whereas the Mn^{III} occupy the octahedral sites [3, 7].

2. Experimental procedure

Tri manganese tetra oxide nanoparticles were prepared by adopting the method of thermal decomposition. The required quantity of manganese acetate tetra hydrate [$(CH_3COO)_2Mn{\cdot}4H_2O$] in its dry form is taken in a ceramic container and is heated in a muffle furnace for a period of 24 hrs, maintained at a temperature of 950 °C. As a result, a brownish black powder of Mn_3O_4 particles was obtained and collected for further characterization.

3. Result and discussion

3.1. XRD characterization

The prepared Mn_3O_4 nanomaterials were characterized by powder X-ray diffraction. X-ray powder diffraction measurements were performed using the X-ray diffractometer operating with Cu-Kα radiation ($\lambda = 0.15406$ nm). Fig. 1 shows the X-ray diffraction spectra for the prepared Mn_3O_4 nanoparticles.

Figure 1 shows the crystalline structure with several significant peaks that can be readily indexed as (112), (200), (103), (211), (004), (220), (105), (224), (312) and (400) crystal planes respectively, which is in good agreement with the standard value, JCPDS No. 024-0734. All the peaks in the pattern can be indexed to a tetragonal phase with lattice constants $a = b = 5.7621$ Å, $c = 9.4696$ Å.

The particle size is calculated according to Debye-Scherrer formula:

$$2d = \frac{0.9\lambda}{\beta cos\theta},$$

where λ is the wave length of Cu-Kα radiation, β is the full width at half maximum, corresponding to the diffraction angle 2θ. The crystal size for the prepared Mn_3O_4 nano particle was found to be 51 – 62 nm.

3.2. FTIR characterization

Figure 2 shows the FTIR spectra of the prepared Mn_3O_4 nano particles which show several significant absorption peaks that help to understand various chemical bonds present in it.

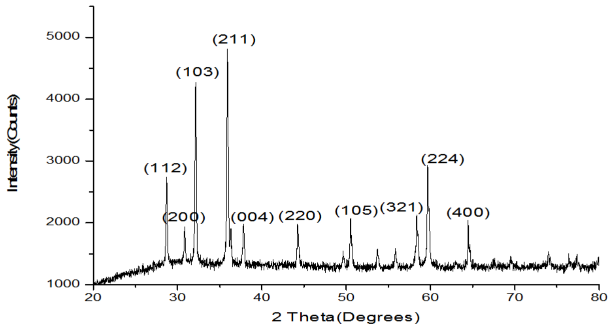

FIG. 1. XRD Spectra for the prepared Mn_3O_4 nano particles

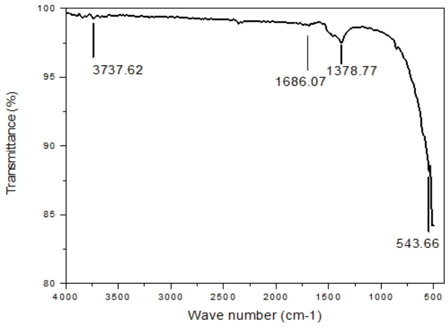

FIG. 2. FTIR Spectra for the prepared Mn_3O_4 nano particle

The vibration frequency located at 543 cm^{-1} corresponds to the vibration of Mn–O stretching modes. Moreover, the broad band at 3738 cm^{-1} and the narrow one at 1666 cm^{-1} correspond to O–H vibrating mode of the adsorbed water. Thus, FTIR provides concrete evidence for the presence of manganese oxide.

3.3. Thermal analysis (TGA/DTA)

The thermal stability of the prepared Mn_3O_4 nano particles was carried out between 250 – 1050 °C.

Figure 3 represent the TGA/DTA spectra for the prepared Mn_3O_4 nano particles. In the temperature range up to 300 °C a weight loss of 2.85 % can be related to the release of weakly adsorbed water molecules. It is found that the sample was completely decomposed within the given range.

3.4. UV characterization

The UV absorption spectra for the prepared Mn_3O_4 nano particle is shown in Fig. 4. The optical absorption peak intensity was found to be 316.507 nm. The optical band gap of the sample is calculated using the formula, $E_g = hc/\lambda$, where E_g – energy gap, c – velocity of light and λ – wave length. The optical band gap for the prepared Mn_3O_4 nano particle was found to be on the order of 3.824 eV.

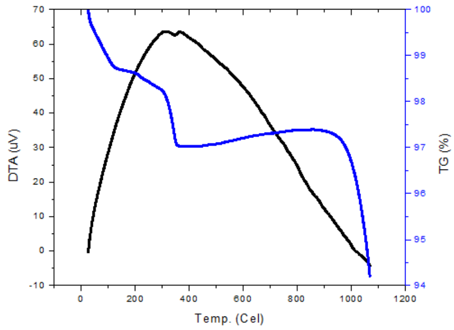

FIG. 3. TGA/DTA Spectra for the prepared Mn_3O_4 nano particle

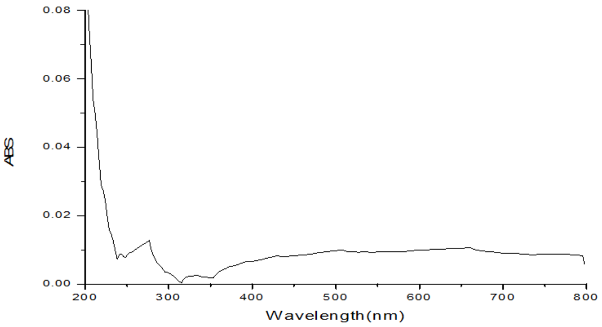

FIG. 4. UV Spectra for the prepared Mn_3O_4 nano particles

4. Conclusions

Mn_3O_4 nano particles were successfully synthesized by using manganese acetate by adopting the method of thermal decomposition. The nano materials thus prepared were characterized by adopting various techniques like XRD, FTIR, UV and thermal analysis. The average particle size is calculated using Debye-Scherrer formula as 56 nm. Presence of Mn_3O_4 is also confirmed from FTIR. Thermal studies were also carried out. The optical band gap for the prepared nanomaterials was found to be 3.824 eV.

Acknowledgements

We would like to acknowledge The University of Kerala X-RD Laboratory (DST-PURSE) Kariavattom Campus, Trivandrum for the XRD characterization. The facilities provided by the research laboratories of Department of Physics as well as the department of Nanotechnology, Noorul Islam Centre for Higher Education were also greatly acknowledged.

References

[1] Shanmugam S. *Nanotechnology*, MJP publishers. 2011.

[2] Usha K., Mahadevan C.K. Structure, Morphology and Electrical properties of Mn_3O_4 nanocrystals. *Scholars Research Library, Archives of Physics Research*, 2011, **2** (1), P. 75–80.

[3] Sherin J.S., Thomas J.K., Suthagar J. Combustion Synthesis and Magnetic Studies of Hausmannite, Mn_3O_4, nanoparticles. *International Journal of Engineering Research and Development*, 2014, **10** (7), P. 34–41.

[4] Hassouna Dhaouadiet, Hassouna Dhaouadi, et al. Mn_3O_4 Nanoparticles: Synthesis, Characterization, and Dielectric Properties. *International Scholarly Research Network Spectroscopy*, 2012, Article ID 706398, 8 p.

[5] Mote V.D., Dargad J.S., Dole B.N. Effect of Mn doping concentration on structural, Morphological and optical studies of ZnO Nano-Particles. *Nanoscience and Nano engineering*, 2013, **1** (2), P. 116–122.

[6] Vijaya Lakshmi S., Pauline S., Maria Vinosel V. Microstructural Characteriztion of Trimanganese Tetra Oxide (Mn_3O_4) Nanoparticle by Solvothermal Method and Its Dielectric Studies. *International journal of engineering sciences & research technology*, 2014, **3** (11), P. 123–131.

[7] Shrividhya T., Ravi G., Mahalingam T., Hayakawa Y. Synthesis and Study on Structural, Morphological and Magnetic properties of nanocrystalline Manganese Oxide. *International Journal of Science and Engineering Applications*, Special Issue NCRTAM ISSN-2319-7560, 2013. DOI: 10.7753/IJSEANCRTAM.1004.

[8] Harish Kumar, Manisha, Poonam Sangwan. Synthesis and Characterization of MnO_2 Nanoparticles using Co-precipitation Technique. *International Journal of Chemistry and Chemical Engineering*, 2013, **3** (3), P. 155–160.

[9] Wang Z.H., Geng D.Y., et al. Magnetic properties and exchange bias in Mn_2O_3/Mn_3O_4 nanoclusters. *Journal of applied physics*, 2009, **105**, 07A315.

[10] Yanyan Yang, Lifen Xiao, Yanqiang Zhao, Fengyun Wang. Hydrothermal Synthesis and Electrochemical Characterization of α-MnO_2 Nanorods as Cathode Material for Lithium Batteries. *Int. J. Electrochem. Sci.*, 2008, **3**, P. 67–74.

[11] Jianghong Wu, Hongliang Huang, Li Yu, Junqing Hu. Controllable Hydrothermal Synthesis of MnO_2 Nanostructures. *Advances in Materials Physics and Chemistry*, 2013, **3** (3), P. 201–205.

[12] Pradeep Kumar B.M., Shivaprasad K.H., et al. Preparation of MnO_2 nanoparticles for the adsorption of environmentally hazardous malachite green dye. *International Journal of Application or Innovation in Engineering & Management (IJAIEM)*, 2014, **3** (12), P. 102–106.

[13] Hansung Kim, Branko N. Popov. Synthesis and Characterization of MnO_2-Based Mixed Oxides as Super capacitors. *Journal of the Electrochemical Society*, 2003, **150** (3), D56–D62.

[14] Hiromichi Hayashi, Yukiya Hakuta. Hydrothermal Synthesis of Metal Oxide Nanoparticles in Supercritical Water. *Materials*, 2010, **3**, P. 3794–3817.

[15] Edelsten A.S., Cammarata R.C. *Nanomaterials synthesis properties and applications*. Novel research laboratory, Washington, 1988.

NANOSYSTEMS: PHYSICS, CHEMISTRY, MATHEMATICS, 2016, 7 (4), P. 650–656

Superhydrophobic coatings using nanomaterials for anti-frost applications – review

S. V. Laturkar, P. A. Mahanwar

Department of Polymer and Surface Engineering, Institute of Chemical Technology,
Matunga, Mumbai, 400019, India

supriyalaturkar13@gmail.com, pa.mahanwar@ictmumbai.edu.in

PACS 82.35.Np, 68.03.Cd **DOI 10.17586/2220-8054-2016-7-4-650-656**

Frost formation and accretion on various outdoor structures like aircraft, wind turbines, heat exchanger coils etc. as well as on glass doors of indoor refrigerators is a serious issue as it presents economic as well as safety challenges. Most of the research done on anti-frost coatings is based on the theme of making the surface super hydrophobic (contact angle > 150 °, Sliding angle < 10 °) mimicking a lotus leaf which provides low or zero ice adhesion. Nanomaterials have played a significant role in such coatings as they help in tuning the surface properties which are surface roughness and surface energy. In this paper, we have tried to investigate why all superhydrophobic surfaces may not be ice-phobic and how nanomaterials improve super hydrophobicity of the surface, in turn, making them anti-frosting. This paper is a detailed study of anti-frosting strategies based on nanosystems which have been developed to date.

Keywords: Anti-frost coatings, superhydrophobic, icephobic, nano fillers, surface roughness, surface energy, contact angle.

Received: 5 February 2016

Revised: 21 April 2016

1. Introduction

When moist air comes in contact with a cold surface, whose temperature is below the triple point of water, frosting or icing takes place on the surface [1].

Considering the phase equilibrium of water-system, if pressure is applied to the system at the triple point (where all the three phases coexist); the effect of applying pressure will be to cause condensation of vapor to liquid or solid phase. Ultimately, the vapor phase will disappear and only two phases, solid and liquid, will stay and further application of pressure will cause increase of pressure with change of temperature along the fusion curve on phase diagram [2]. This implies that pressure exerted by humid air is responsible for frosting or icing on many outdoor structures in colder regions such as wind turbines, aircrafts, heat exchangers (air-conditioners/heaters), as well as domestic and industrial refrigerators/freezers. Thus, frosting is a condensation phenomenon and temperature of the (cold) surface, percent relative humidity (% RH) and temperature of air, are the factors which influence frosting and defrosting.

Frost formation and accretion on various infrastructures is a serious issue as it presents economic as well as safety challenges. For example, the ice accretion on aircraft results in drag increase and sometimes may lead to dangerous loss of lift force, which may cause tragic crashes [3]. Ice accretion on wind turbine blades can cause a production loss of as much as 50 % of the annual production [4]. Furthermore, frost and ice accumulation in refrigerators and heat exchangers results in a decrease of heat transfer efficiency up to 50 – 75 % [5].

Several conventional defrosting/de-icing techniques include electric heating which accelerates ice melting or breaking the accretion by direct scrapping which neither safe nor efficient. In addition, Automatic robots, electromagnetic forces [6] are reported for the de-icing of overhead transmission lines. Thus, most of these conventional anti-frosting strategies are often inefficient, energy-consuming, high-cost, or environmentally harmful. Applying an anti-frost or defrosting coating on the cold surface has been found as the most promising and interesting method in the past two decades, realizing the objective of preventing frosting and saving energy.

Initially freezing point depressants such as Ethylene glycol were incorporated into the resin or a hydrophilic polymer was impregnated with an anti-freeze, for defrosting in heat exchangers [7]; which was later replaced by- developing an 'ice-phobic' surface where the substrate is mostly made superhydrophobic which exhibit water contact angles exceeding 150 °C, mimicking a lotus leaf. Today, many such anti-frosting strategies have been developed by incorporating various nanomaterials in the coating formulation.

This paper clarifies the terms 'superhydrophobicity' and 'ice-phobicity'. It reviews the significance of nanomaterials for tuning the surface properties of a glass or a metal substrate so as to make it 'anti-frost'; along with some important anti-frosting strategies which have been developed till date.

2. Superhydrophobicity and ice-phobicity

The wettability of a flat surface is directly related to the surface energy and is expressed by contact angle (CA) θ of a water droplet given by Young's equation:

$$\cos\theta = \frac{\gamma_{SV} - \gamma_{SL}}{\gamma_{LV}}, \tag{1}$$

where, γ_{SV}, γ_{SL}, γ_{LV} refer to the interfacial surface tensions with S(solid), L(liquid) and V(gas) respectively. Surfaces with water contact angles (CA's) greater than 150 ° are considered superhydrophoic or ultraphobic. The dynamic CA's are measured during the growth (advancing) and shrinkage (receding) of a water droplet as contact angle hysteresis CAH ($\triangle\theta = \theta a - \theta r$). The values of $\triangle\theta$ can be as low as below 10 ° on some surfaces, whereas many surfaces show much larger hysteresis, due to chemical heterogeneity and roughness [8].

The superhydrophobic surfaces are usually covered with micro- or nanoscale asperities (rough). Water can either penetrate the asperities (Wenzel state: wet-contact mode) or be suspended above the asperities (Cassie Baxter state: nonwet-contact mode). In either case, much higher contact angles are observed than those obtained for the corresponding flat surface. For a hydrophobic surface, in the Wenzel's regime, the contact angle and its hysteresis increase as the roughness factor increases until it exceeds 1.7, from where the CAH starts to decrease. The decrease in the contact angle hysteresis is attributed to the switching from the Wenzel to the Cassie–Baxter state due to the formation of hierarchical rough morphology with sufficient air trapped in the gap to reach Cassie state of suspension of water droplet on top of the asperities as shown in Fig. 1 [8, 9].

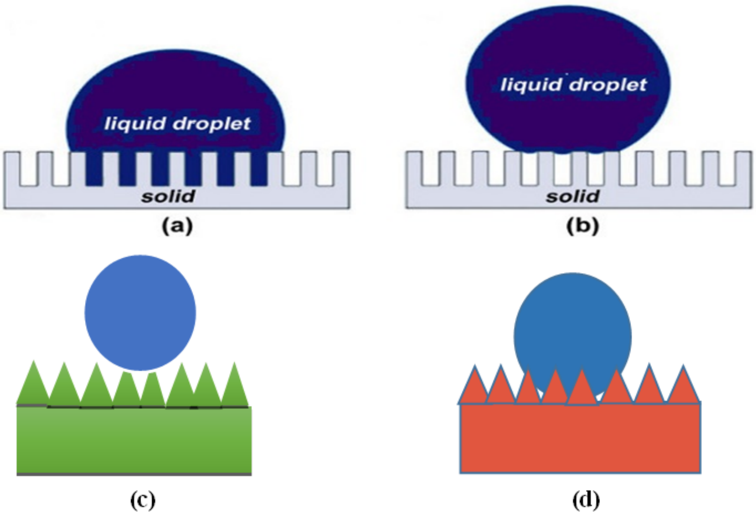

FIG. 1. Wenzel model (a); Cassie-Baxter model (b); Behaviour of a liquid droplet on lotus leaf (Cassie state) (c); Behaviour of a liquid droplet on rose petal (Cassie impregnating wetting state) (d)

Thus, when a rough surface reaches 'Cassie' state it can show the 'self-cleaning' effect from where the dust particles or frost roll off when surface is slightly tilted, mimicking a Lotus leaf. (Also known as 'lotus effect' characterized by high CA and low CAH). Another special case of Cassie state is 'rose petal' inspired surfaces where the water droplets enter into the larger scale grooves of the petal but not into the smaller ones, thus forming a Cassie impregnating wetting state (characterized by high CA and high CAH due to adhesive property of the petal). These two effects can be attributed to difference of the microstructures and chemical composition between the petal and the lotus leaf [9].

Now, talking about ice-phobicity, a surface should be called ice-phobic if it delays frost formation from incoming water (moisture) or delays ice formation from condensed droplets (frost crystals) in the situation where normally ice would form and/or there is low adhesion force between ice and the solid surface [10]. Considering this definition, it is clear that to achieve ice-phobicity or anti-frost property on a cold surface, the surface can be made superhydrophobic with low adhesion force i.e. low CAH so that the incoming water droplets (moisture) roll off as soon as they condense and before converting into the frost; thus, frost accumulation can also be avoided due to low or non-adhesion.

This implies that lotus leaf inspired surfaces (high CA, low CAH) can show ice-phobicity and not the rose petal inspired ones. However, it has been also studied that every superhydrophobic surface which shows self-cleaning behavior (lotus effect) may not necessarily show ice-phobicity. There are several other parameters, such as surface roughness, mechanical robustness of the surface so as to maintain the same superhydrophobicity at sub-zero temperatures and with subsequent icing /de-icing events. This can be explained by the following example:

S. A. Kulinich et al. studied the ice-releasing properties of rough hydrophobic coatings based on different materials with different surface topographies [11]. Three samples were investigated for ice-phobic properties: 1. Etched aluminium alloy coated with an organosilane (ODTMS). 2. TiO_2 nanopowder functionalized with perfluoroalkyl methacrylic copolymer (Zonyl) applied on the substrate by spin coating. 3. TiO_2-Zonyl applied by spray coating. Fig. 2 shows both CA and CAH values obtained for the above three samples. Table 1 shows root mean square roughness values for the three samples at various icing-de-icing events. From Table 1 and Fig. 2 it can be seen that sample 3 though maintains high roughness after 6 de-icing cycles, high CAH 80 ° leads to high ice adhesion strength. Sample 1 and 2 show higher contact angles 153 ° and 152 ° respectively along with low CAH values (5.7 ° and 6.1 ° respectively).

TABLE 1. Variation in surface roughness with subsequent icing-deicing events

Sample Number	**Sample Description**	**Root-mean-square roughness (nm) at event:**					
		1	**2**	**3**	**4**	**5**	**6**
1	Etched Al/ODTMS	240	238	237	237.5	232	230
2	TiO_2 spin	210	200	170	168	167	165
3	TiO_2 spray	310	290	300	302	305	305

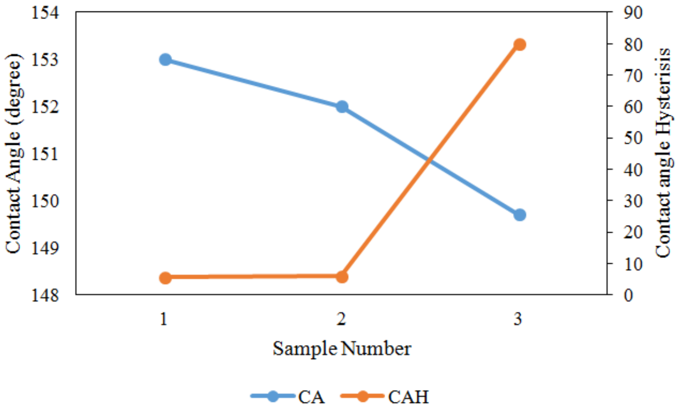

FIG. 2. Contact angle and contact angle hysteresis for three different samples

However, there is a gradual decrease in roughness for sample 2 due to the sharper and much taller asperities which were believed to be gradually damaged during icing/de-icing cycles, whereas sample 1, also having sharp and tall asperities, seemed to be more resistant to damage during icing/de-icing. This was likely due its more rigid asperities (built of Al_xO_y) compared to those in sample 2 (based on fluoropolymer heavily loaded with TiO_2 nanoparticles). Thus, the more robust nanostructured surface prepared by etching the aluminium substrate maintained the ice-releasing properties better compared to its counterparts.

3. Role of nanomaterials

Nanomaterials play a significant role in the tuning of surface properties of the substrate which is desired to be superhydrophobic and also ice-phobic. As mentioned in section 2, to achieve ice-phobicity, the surface has to reach the Cassie state (high CA, low CAH), which can be accomplished by increasing the surface roughness. Nanomaterials such as carbon nanotubes, hydrophobic nanosilica, ZnO nanorods etc. are often used both as fillers and for functionalization, to impart roughness to the surface, and also to improve the mechanical properties of the surface.

Qitao Fu et al. prepared mechanically robust sol-gel type of ice-phobic coatings and once again clarified the significance of nanofillers in designing superhydrophobic surfaces and also that all superhydrophobic surfaces may not be ice-phobic [12]. Two sets of samples were prepared, one having coating samples prepared by using MTEOS, GLYMO and varying amounts (5 – 20 wt %) of silica nanoparticles; and the other having coating samples prepared by adding varying amounts of FAS (4 – 16 wt %) to the above formulations. The first set of samples showed increase in water CA i.e. increase in superhydrophobocity with an increase in nanofiller content as a result of increased surface roughness. However, such samples with high silica content failed in maintaining the superhydrophobicity below room temperature (high ice adhesion). On the other hand, a second set of samples containing a low surface energy fluoroalkylsilane showed ice-phobocity to temperatures as low as -10 °C. With 0.31 – 0.35 μmol/gm of FAS in sol and 16 wt % silica nanoparticles, the surface maintained CA ~ 170 °, SA ~ 4.4 ° at -10 °C. The samples containing only FAS without nanofiller or with up to 8 % nanofillers were able to give CAs up to 120 ° and higher sliding angles (60 – 80 °) and therefore failed to show both superhydrophobicity and ice-phobicity.

Carbon nanotube-based composite materials have been investigated for superhydrophobic coatings to improve mechanical strength. Yoonchul Sohn et al. developed an anti-frost coating with reliable thermal cyclic properties [13]. A superhydrophobic multi-walled carbon nanotube (MWCNT)–silicone composite film (Cassie structure) that can endure over 4000 thermal cycles (-30 °C to room temperature, 40 % RH) was fabricated by controlling the composition and microstructure of the composite. The nanofiller content of this coating was 20 vol %, showing thermo-mechanical reliability without significant change in the contact angle ($\sim$ 160 °). A composite structure having higher nanofiller content (20 – 30 %), which contains numerous pores, can accommodate high levels of thermal stress. The stress relaxation can reach 48 % and 84 % of the reference point for the 20 and 30 vol % MWCNT specimens, respectively. Since the coefficient of thermal expansion (CTE) of silicone (310 ppm °C) is much larger than that of MWCNTs (7 ppm °C), the large expansion and shrinkage of silicone matrix compared to MWCNT fillers resulted in cracking of specimens containing lesser nanofiller content, after 1000 thermal cycles. Though the 30 vol % MWCNT-silicone film is better for stress relaxation, the 20 vol % film shows superior ice-phobic properties (lower CAH).

Thus nanopores in superhydrophobic coatings, constituting air pockets in a Cassie structure, are of great importance not only for wetting characteristics but also for superior reliability induced by stress relaxation. Although a more open structure can help relax more stress arising from a CTE mismatch, the composition of a superhydrophobic coating should be carefully selected to optimize its wetting characteristics while maintaining its mechanical reliability.

4. Superhydrophobic anti-frost coatings using nanotechnology

Min He et al. also developed anti-frost coatings for glass substrates. They prepared superhydrophobic surfaces using ZnO nanorod arrays, which could maintain superhydrophobicity to condensed micro-droplets at temperatures below the freezing point. ZnO nanorod arrays were employed because of their controllable morphologies. Materials with different ZnO nanorod arrays were fabricated by the method of low-temperature wet chemical bath deposition and modified with a fluoroalkylsilane (FAS-17) to obtain super-hydrophobicity, even at temperatures lower than 0 °C [14]. Firstly, ZnO seeds layer was obtained on the cover glass by treating it with zinc acetate and then it was immersed into an equimolar solution of $Zn(NO_3)_2$ and hexamethylenetetramine, and kept sealed at a temperature of 90 °C for different times (t_{ZnO}) to control the growth (size) of the ZnO nanorods. Table 2 shows the change in contact angle with t_{ZnO} at room temp., -5 °C and -10 °C. The values of sliding angle have been mentioned only at room temperature as 1 °, 1 ° and 2 ° for t_{ZnO} 1 h, 2 h and 3 h respectively. The ice-phobic behavior when compared with that of a hydrophobic glass surface, it has been observed that the time of condensed droplets maintaining a liquid state is much longer on the superhydrophobic ZnO nanorod array surfaces. Furthermore, the shorter growth time (t_{ZnO}) of ZnO nanorods, increases the time period for maintaining condensed droplet in the liquid state, thus providing better anti-frost performance.

Hao Wang et al. fabricated anti-frosting copper surfaces for evaporator coils of industrial refrigerators and air-conditioners. This coating was based on nanosized $CaCO_3$ particles modified with heptadecafluorodecyl trimethoxysilane mixed in an ordinary polyacrylate binder [15]. The coating, when applied on glass, showed superhydrophobic behavior (with $CA = 155$ °) and maintained the same superhydrophobicity on copper plate for subsequent 10 frosting-thawing treatments at temperature -7.2 °C and 55 % humidity. In this case, frost formation was not totally inhibited, but the rate of frosting was greatly reduced as compared to bare copper or ordinary hydrophobic surfaces and formed frost was able to roll off the plate when mounted vertically as a result of roughness (nano $CaCO_3$) and low surface energy FAS.

Yanfen Huang et al. developed ice-phobic coatings to protect aluminium ground wires and phase conductors of overhead power lines from icing [16]. The coating was prepared by a simple, inexpensive method using silica/fluorinated acrylate copolymers. The nano silica sol was mixed with fluorinated acrylic copolymers in different weight ratios. The films showed good hydrophobicity (CAs up to $141.7\ ^\circ$C) and especially excellent mechanical properties of adhesion strength and pencil hardness as compared to other superhydrophobic surfaces. The coated Al surface can delay icing for 90 min. compared with the glass surface at $-5.6\ ^\circ$C.

Hyomin Lee et al. prepared a zwitter-wettable surface, i.e. one that has the ability to rapidly absorb molecular water from the environment while simultaneously appearing hydrophobic when probed with water droplets [17]. This can be prepared by using hydrogen-bonding-assisted layer-by-layer (LbL) assembly of poly (vinyl alcohol) (PVA) and poly(acrylic acid) (PAA). An additional step of functionalizing the nano-blended PVA/PAA multilayer with poly (ethylene glycol methyl ether) (PEG) segments produced a significantly enhanced antifog and frost-resistant behavior. The addition of the PEG segments was needed to further increase the non-freezing water capacity of the multilayer film. The desirable high-optical quality of these thin films arises from the nanoscale control of the macromolecular complexation process that is afforded by the LbL processing scheme. The author justifies the inhibition of frost formation on glass due to this type of coating by the fact that in this case, the water molecules are presumably molecularly dispersed as a result of strong polymer-water hydrogen bonding interactions and hence are not capable of freezing at the usual temperature. Also, the above-prepared nanoscale LbL assembly ensures that crystallisation of PVA molecules will be limited or non-existent, which is helpful to accommodate more amount of non-freezing water.

William Tong et al. designed transparent glass windows with antifrost/anti-fog capabilities in order to maintain the aesthetic appearance of glass windows for vehicles and modern buildings [18]. The nanostructured metamaterials can be coated on the window's outside surface. A tungsten-silica-tungsten (at nanoscale) metamaterial coating was used as the solar absorber to coat on window's outside surface. The top layer of the absorber is a 1D tungsten planar stack, the dielectric SiO_2 spacer works as optical cavity and the bottom tungsten film as non-perfect or perfect mirrors. The profile of this three-layer structured coating can be designed by adjusting the thickness of bottom and top layers in such a way that sufficient visible light transmits through the window glass for enough lightening in the room, while maximum infrared waves can be absorbed for heating. The coating was deposited using closed field magnetron sputtering (CFM). This nanoscale metamaterial structure with periodic metal-dielectric interfaces efficiently absorbs solar radiation and with proper design, the window surface temperatures can be well controlled which is useful for efficient anti-frosting and anti-fogging. The transparency can be adjusted by changing the tungsten layer thickness ($\sim$ 300 nm) meanwhile the absorption performance of the solar absorber has no significant variation.

Aeree Kim et al. fabricated a 'nanostructured' and therefore superhydrophobic Al surface for anti-frosting applications due to its property of enhanced self-propelled jumping by condensate droplets. This Al surface was fabricated in three following steps: 1. Alkali treatment (0.05 M NaOH) to produce an aluminium hydroxide ($Al(OH)_3$) layer. 2. Boiling the specimens in deionized water to induce formation of nanostructures. 3. A self-assembled monolayer (SAM) of fluorochlorosilane was applied to render it superhydrophobic as well as ice-phobic. It can be seen from Fig. 3 that the time for which the specimens are immersed in boiling water governs the surface's nanostructure and hence, the CA and CAH. All four specimens were alkali treated for the same time (5 min) and coated with SAM layer, however, different CA and CAH values were obtained for those samples having different boiling times. Samples had higher CA and lower CAH for 5 – 30 minutes boiling, as shown in Fig. 3. Self-Propelled Jumping (SPJ) by condensate droplets that occurs on superhydrophobic surface, shows significant dependency on the super saturation $S = PV/PW$, where PV is the vapor pressure and PW is the saturation pressure that corresponds to the specimen surface temperature. Frost formation on the above 'nanostructured' aluminium was delayed more than 4 times at $S = 3.41$ and $S = 6.39$ compared to smooth Al surface [19].

TABLE 2. Effect of t_{ZnO} on contact angle

	Contact angle		
$t_{\mathbf{ZnO}}$	**Room temp.**	**$-5\ ^\circ$C**	**$-10\ ^\circ$C**
1 hr	170.9 °	167.9 °	163.4 °
2 hr	166.1 °	160.3 °	158.2 °
3 hr	165.8 °	154.6 °	155.4 °

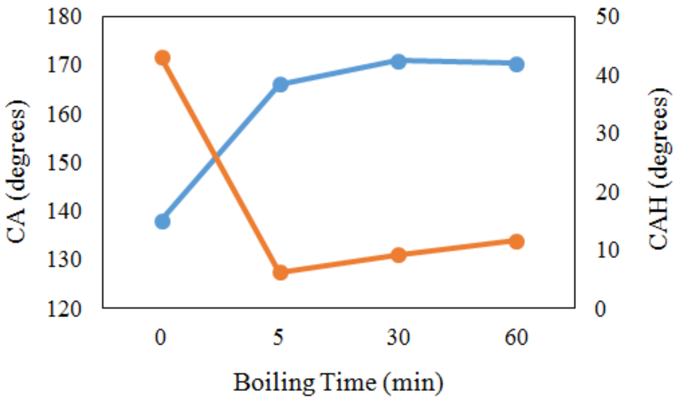

FIG. 3. Effect of boiling time on CA and CAH

The lotus leaf-inspired superhydrophobic surfaces show promising ice-phobicity but at high humidity conditions, they may fail. Due to their high surface area and increased nucleation site density to condensing droplets, they may induce ice nucleation at an even faster rate than smooth surfaces of the equivalent materials at high humidity conditions [20]. Slippery liquid infused porous surfaces (SLIPS) have attracted great interest as anti-icing coatings. The 'pitcher plant' inspired slippery surfaces capable of repelling condensing water droplets have been created by infiltrating a micro/nanoporous substrate with a lubricating liquid to produce a thin, ultra-smooth lubricating layer that repels almost any immiscible materials. Such SLIPS have been fabricated on industrially-relevant metals like aluminium and thus can be used as antifrosting surfaces for aircraft, refrigeration etc. The criteria for designing SLIPS are: 1) the lubricating fluid repellent fluid (e.g. water, oil) have to be immiscible; 2) the chemical affinity between the lubricating fluid and the solid should be higher than that between the repellent fluid and the solid; 3) the solid surface should preferably have roughened nanostructures to provide increased surface area for the adhesion and retention of the infiltrated lubricating fluid [21].

Kim et al. developed aluminium based SLIPS by the electrodeposition of highly textured polypyrrole (PPy) on Al substrates followed by fluorination of the structured coating and infiltration with the lubricant. PPy/Al surfaces having rough and globular morphology were fluorinated with a fluorochlorosilane and infiltrated with a low viscosity perfluorinated lubricating fluid which has freezing point less than -70 °C, immiscible with water and strong chemical affinity to the modified solid substrate. The contact angle hysteresis (CAH) which decides the surface retention force was found to be lowest as below 3 ° for the SLIPS-Al specimens when compared with the bare Al, hydrophobically modified Al and even with superhydrophobic PPy coated Al (without lubricant). While checking the ice-phobic behavior, it has been observed that SLIPS-Al surface delays frost formation. After 100 min of freezing (at -2 °C, 60 % RH), only 20 % surface is covered with ice. After a prolonged exposure to deep freezing, ice accumulates on the surface, however, during the defrost cycle, the large ice patches slide off the surface immediately upon melting at the interface, leaving the surface clean and ready for the next cooling cycle within 1 minute. The average ice adhesion strength on SLIPS/Al has been reported as 15.6 kPa. This low adhesion strength is attributed to the ultrasmooth solid-liquid interface present at the SLIPS surface which has significantly fewer defects/ heterogeneities/pinning points than the solid-solid interface found in conventional superhydrophobic surfaces [22].

Though SLIPS are promising for anti-icing, the most challenging point is their durability. Water tolerance, lubricant retention ability after subsequent icing-deicing cycles are the parameters to be considered while designing a SLIPS. Q Liu et al. developed hierarchically micro structured high temperature vulcanized silicone rubber (HTV) infiltrated with a perfluoropolyether lubricant to form SLIPS. These surfaces showed water contact angle more than 162 ° and lubricant contact angle nearly 0 °, which suggests that the lubricant can infiltrate completely into the substrate. As the no. of icing/deicing cycles increased the freezing and thawing times accelerate which is related to the lubricant depletion. The lubricant retention rate (LRR) at -14 °C, 80 % RH and air at 18 °C for the above surface was found to be nearly 37 % after 4 cycles. Also, these samples showed best results for delayed ice formation. Ice adhesion strength was nearly 250 kPa up to 5 cycles and maximum 700 kPa for 20 cycles [23].

Recently, Chanda et al. studied and compared the advantages and disadvantages of superhydrophobic and hydrophilic surfaces with respect to their anti-frosting properties and came to the conclusion that neither purely (super)hydrophobic polymeric surfaces, nor 'antifreeze' hydrophilic ones provide an ideal solution for the problem of icing [24].

5. Conclusion

Frost formation and accretion on various infrastructures is a serious issue, as it presents economic as well as safety challenges. Considering the current anti-frosting strategies based on superhydrophobic surfaces, it should be made very clear that superhydrophobicity and ice-phobicity are different phenomena as far as practical applications are concerned. Nanotechnology is the backbone of such coatings which helps in tuning the morphology of the surface by providing the required surface roughness for a coating's superhydrophobic nature and mechanical strength. The amount of nanofillers to be incorporated or the procedures to be followed while fabricating a nanostructured surface are also important in order to obtain the desired anti-frosting properties.

There is still scope for development of more bio-inspired anti-frosting strategies, such as grafting nanomaterials on smart interface materials, the use of different binder combinations for naofiller, fluorinated system or simplifying the design methods for 'slippery' surfaces.

References

[1] Zhongliang L., Hongyan W., Xinhua Z. An experimental study on minimizing frost deposition on a cold surface under natural convection conditions by use of a novel anti-frosting paint. Part I. *International Journal of Refrigeration*, 2006, **29**, P. 229–236.

[2] Puri B.R., Sharma L.R., Pathania M.S. *Principles of Physical Chemistry*. Vishal publications, Jalandhar, 2002, 281 p.

[3] Gent R.W., Dart N.P., Cansdale J.T. Aircraft icing. P*hil. Trans. R. Soc. Lond. A*, 2000, **358**, P. 2873–2911.

[4] Botta G., Cavaliere M., Holttinen H. Ice accretion at acqua spruzza and its effects on wind turbine operation and loss of energy production. *BOREAS IV*, 1998, 31 March – 2 April, Hetta, Finland, P. 77–86.

[5] Huang Lingyan, Zhongliang Liu, et al. Experimental Study on Frost Release on Fin-and-Tube Heat Exchangers by Use of a Novel Anti-Frosting Paint. *Experimental Thermal and Fluid Science*, 2009, **33** (7), P. 1049–1054.

[6] Dalili N., Edrisy A., Carriveau R. A Review of Surface Engineering Issues Critical to Wind Turbine Performance. *Renewable and Sustainable Energy Reviews*, 2009, **13**, P. 428–438.

[7] Ostin R., Johannesson G. A Polymeric Approach to Counteract Frosting in Air-to-Air Heat Exchangers. *Heat Recovery Syst. CHP*, 1991, **11** (5), P. 415–421.

[8] Li X.M., Reinhoudt D. What do we need for a superhydrophobic surface? A review on the recent progress in the preparation of superhydrophobic surfaces. *Chem. Soc. Rev.*, 2007, **36**, P. 1350–1368.

[9] Feng L., Zhang Y., Xi J., Zhu Y. Petal effect: A superhydrophobic state with high Adhesive force. *Langmuir*, 2008, **24** (8), P. 4114–4119.

[10] Hejazi V., Sobolev K., Nosonovsky M. From Superhydrophobicity to Icephobicity: Forces and Interaction Analysis. *Scientific reports*, 2013, **3**, P. 2194.

[11] Kulinich S.A., Farzaneh M. On Ice-Releasing Properties of Rough Hydrophobic Coatings. *Cold Regions Science and Technology*, 2011, **65** (1), P. 60–64.

[12] Fu Q., Kumar D., et al. Development of sol-gel icephobic coatings: effect of surface roughness and surface energy. *ACS Applied Materials and Interfaces*, 2014, **6**, P. 20685–20692.

[13] Sohn Y., Kim D., Lee S., Yin M. Anti-frost coatings containing carbon nanotube composite with reliable thermal cyclic property. *Journal of Materials Chemistry A*, 2014, **2**, P. 11465–11471.

[14] He M., Wang J., Li H., Song Y. Super-hydophobic surfaces to condensed micro-droplets at temperatures below the freezing point retard ice/frost formation. *The Royal Society of Chemistry*, 2011, **7**, P. 3393–4000.

[15] Wang H., Tang L., Wu X., Dai W. Fabrication and anti-frosting performance of supehydrophobic coating based on modified nano-sized calcium carbonate and ordinary polyacrylate. *Applied Surface Science*, 2007, **253**, P. 8818–8824.

[16] Huang Y., Hu M., et al. Preparation and characterisation of silica/fluorinated acrylate copolymers hybrid films and the investigation of their icephobicity. *Thin Solid Films*, 2012, **520**, P. 5644–5651.

[17] Lee H., Alcaraz M., Rubner M.F., Cohen R.E. Zwitter-wettability and anti-fogging coatings with frost resisting capabilities. *ACS NANO*, 2013, **7** (3), P. 2172–2185.

[18] Tong W., Tong A. Anti-frost and energy saving transparent glass windows manipulated through solar absorbing metamaterial coatings. *Global Advanced Research, Journal of Engineering, Technology and Innovation*, 2015, **4** (3), P. 31–40.

[19] Kim A., Lee C., Kim H., Kim J. Simple approach to superhydrophobic nanostructured Al for practical anti-frosting applications based on Enhanced self-propelled jumping droplets. *ACS Applied Materials and Interfaces*, 2015, **7**, P. 7206–7213.

[20] Jung S., Dorrestjin M., et al. Are superhydrophobic surfaces best for icephobicity? *Langmuir*, 2011, **27**, P. 3059–3066.

[21] Wong T.S., Kang S.H., et al. Bioinspired self-repairing slippery surfaces with pressure-stable omniphobicity. *Nature*, 2011, **477**, P. 443–447.

[22] Kim P., Wong T.S., Alvarenga J., Kreder M.J. Liquid infused nanostructure surfaces with extreme anti-ice and anti-frost performance. *ACS NANO*, 2012, **6** (8), P. 6569–6577.

[23] Liu Q., Wang Y., et al. Durability of a lubricant infused electrospray silicon rubber surface as an anti-icing coating. *Applied Surface Science*, 2015, **346**, P. 68–76.

[24] Chanda J., Lonow L., Kirillova A., Synytska A. New insight into icing and de-icing properties of hydrophobic and hydrophillic structured surfaces based on core-shell particles. *Soft matter*, 2015, **11**, P. 9126–9134.

NANOSYSTEMS: PHYSICS, CHEMISTRY, MATHEMATICS, 2016, 7 (4), P. 657–661

Electro chemical and photo catalytic studies of MnO_2 nanoparticle from waste dry cell batteries

M. Mylarappa[1,2], V. Venkata Lakshmi*[1], K. R. Vishnu Mahesh**[3], H. P. Nagaswarupa[4],
S. C. Prashantha[4], D. M. K. Siddeswara[4] and N. Raghavendra[5]

[1]Research Centre, Department of Chemistry, AMC Engineering College, Bengaluru-560083, Karnataka, India
[2]Department of Studies and Research in Chemistry, Tumkur University, Tumkur-572103, Karnataka, India
[3]Department of Chemistry, Dayananda Sagar College of Engineering, Bengaluru-560083, Karnataka, India
[4]Research Centre, Department of Science, East West Institute of Technology, Bengaluru-560091, Karnataka, India
[5]CMRTU, RV College of Engineering, Bengaluru-560059, Karnataka, India
*laxmimurthy@rediffmail.com, **vishnumaheshkr@gmail.com

PACS 82.47.-a **DOI 10.17586/2220-8054-2016-7-4-657-661**

The objective of the existing research was essentially focused on recovery of MnO_2 nanoparticles from consumed dry cells by employing adapted hydrometallurgical process. Experimental tests for the recovery of MnO_2 present in the dry cell batteries have been carried out by an acidic reductive leachant, namely oxalic acid. The elemental compositions of the recovered metals from dry cells were confirmed by Energy Dispersive X-ray analysis (EDAX). Surface morphology of the recovered metals was examined using Scanning Electron Microscopy (SEM). Phase composition of the recovered metals from dry cell batteries were confirmed from X-ray Diffract meter (XRD). Cyclic Voltammetry (CV) studies were carried out to clarify the reversibility of the reactions. The obtained MnO_2 catalyst was applied for the degradation of different non-volatile dye compounds such as Indigo carmine (IC) and Rhodamine B (RB). The performance of MnO_2 shows fast degradation of dyes of high concentration.

Keywords: Dry cell batteries, recovery, Zn, Mn, electrochemical, catalytic activity.

Received: 5 February 2016

1. Introduction

Dry cell batteries are used in radios, recorders, toys, remote controls, watches, calculators, cameras, and in many other objects. The waste batteries present serious problems due to their toxicity, abundance and longevity in the environment [1]. The hydrometallurgical methods are the most popular process in all over the world because of its environmental suitability and economical coasts for treating even low zinc and manganese containing materials on small scale with high purity and low energy requirements [2, 3]. Hence, the treatment of these wastes for the recovery of manganese is vigorous for discarded material to raw material recycling. Two different acid-reductive leaching agents have been investigated; sulfuric acid - oxalic acid and sulfuric acid- hydrogen peroxide. MnO_2 is economically and commercially-important with applications in different fields, such as battery industry, catalysis, water treatment plants, steel industry and chemicals. In this study, we show how to recover manganese as MnO_2 from consumed dry cell using a hydrometallurgical process, without altering the concentration of zinc in solutions that can be recovered by precipitation or electro winning [4]. The aim of this work is to study the applicability of electrochemical and photocatalytic enactment of MnO_2 using a hydrometallurgical process and the catalytic action of MnO_2 is due to its high efficiency in the reduction/oxidation cycles [1]. The effects of the recovered conditions and crystallinity of MnO_2 on the catalytic performance in degradation of high concentration dyes (methylene blue indigo carmine and Rhodamine B) were intensively evaluated [5].Nanostructured materials have received enormous interest in recent years because of their unusual properties when compared with bulk materials. Nanoscale one-dimensional (1D) structures such as nanotubes, nanowires and nanorods have attracted much interest because of their unique electronic, optical and mechanical properties due to the low dimensionality and the quantum confinement effect. For example, the electrons interact differently in one dimensional (1D) and three-dimensional structures (3D). The 1D system is the smallest dimensional structure that can be used for efficient transport of electrons and optical excitations, and is thus expected to be critical to the function and integration of nanoscale devices. 1D nanostructure provides a good system for investigating the electrical and thermal transport properties in size and shape reduction [6–8]. The aim of this work is to study the applicability of electrochemical and photocatalytic enactment of MnO_2 using a hydrometallurgical process and the catalytic action of MnO_2 is due to their high efficiency in the reaction/oxidation cycles [1]. The effects of the recovered conditions and crystallinity of MnO_2 on the catalytic performance in degradation of high concentration dyes (methylene blue indigo carmine and Rhodamine B) were thoroughly evaluated [5].

2. Experimental

The waste dry cell batteries in an amount of 100 g were collected from different manufacturers. A series of mechanical processing is conducted in the following sequence to yield enriched Zn and Mn particles. The waste dry cell batteries were fed to a hammer mill for dismantling. Magnetic separator removed the magnetic fractions and the non-magnetic fraction was screened in a 2 mm sieve. A second magnetic separation was carried out to remove the ferrous materials which remain in the sample. The sieved powder was later washed with deionized water and finally dried at 100 °C for 24 hrs. The washed powder (20 g) was subsequently dissolved in 100 mL, 3 M H_2SO_4 followed by addition of 5.94 g Oxalic acid dehydrated as leaching agent. The leaching was continued for 5 hrs at 90 °C with continuous stirring. Recovery of MnO_2 particle from the leaching solution is possible at room temperature without special purification of the solution, and preserving a high efficiency. After the complete reductive acid leaching process, the required quantity of leached solution in a 500 ml beaker and a solution of 4 M NaOH was added slowly to the beaker with constant magnetic stirring. At the end of the precipitation, the solution in the beaker was filtered and the solid residue remaining in the filter paper was dried in an oven at 100 °C for 24 hours. MnO_2 was formed as dark precipitate at the bottom of the cell. The recovered sample was investigated by means of the EDX, SEM and XRD to analyze elemental composition, morphology and phase composition of the powder.

3. Result and discussion

Energy Dispersive X-ray analysis (EDX) was carried out to obtain the elemental composition of the metals in powder sample. The accurate size and morphology of the MnO_2 studied from the Scanning Electron Microscopy (SEM) and X-ray diffraction spectroscopy (XRD). Fig. 1(a) shows that manganese and oxygen contents were detected in that point, indicating the presence of high manganese hydroxide content [9]. The leaching residue showed almost similar particle size compared to that before leaching. Particles are well distributed throughout with little agglomeration; particle sizes ranged from 5 to 30 μm. In Fig. 1(b), the average particle size of MnO_2 is found to be 9 nm, indicating good crystallinity.

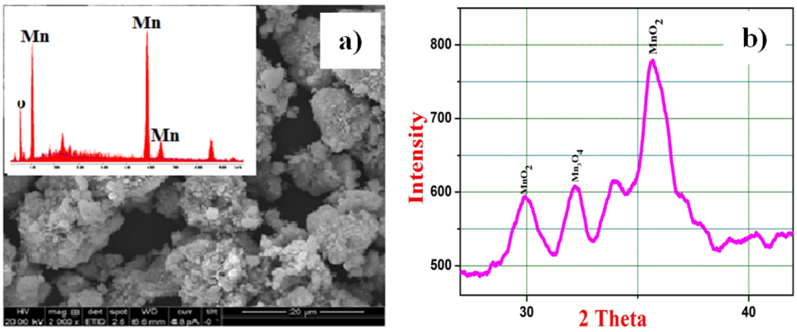

FIG. 1. EDAX/SEM and XRD spectra of MnO_2 from dry cells

4. Cyclic voltammetry studies

The MnO_2 electrode was prepared as a commixture with 10 wt.% of MnO_2 powder as active material with 90 wt.% of graphite. The constituents were mixed along with 3 drops of silicone oil to obtain uniform composition. Electrochemical activity of MnO_2 is often assessed by CV and electrochemical impedance spectra (EIS). An electrochemical measurement utilizes a three-electrode system having working electrode, Ag/AgCl reference electrode and a platinum wire as counter electrode. Cyclic voltammetry (CV) and EIS were performed in potential between $+0$ to -1 V using 0.5 M KCl, NaOH, Na_2SO_4 and NaCl electrolytes at a constant scan rate [6, 10]. To evaluate the electrochemical reversibility (E_R) of the sample, the potential window of CV was changed from $+0$ to -1 V and sweep rate 10 mV as shown in Fig. 2(a). A smaller the value of $E_0 - E_R$ shows the reversibility of the electrode reaction is greater. In Figs. 2(a) and 2(b), it is clearly shown that the smaller the value of $E_0 - E_R$, the greater the reversibility of the electrode reaction is. Samples having lower solution resistance values (Rs) are going higher conductivity values. In Figs. 2(a) and 2(b), it is readily seen that the MnO_2 sample using 0.5 M NaOH has lower E_R compare to different electrolytes, indicating the higher conductivity. The comparative cyclovoltammetric results of electrode in several electrolytes at a scan rate of 10 mV/s are tabulated in Table 1. Fig. 3(a) to (d) show the different scan rates with different electrolytes. The effect of scan rate is presented in Fig. 3. As the

TABLE 1. Electrochemical reversibility

Electrolytes	E_0 (mV)	E_R (mV)	$E_0 - E_R$	Rct (ohm)	$C(F) \times 10^{-5}$
0.5 M KCl	0.3951	0.3373	0.0578	15.75	0.0282
0.5 M NaOH	0.3040	0.3261	0.0221	15.15	0.01594
0.5 M Na_2SO_4	0.4443	0.3939	0.0504	22.28	0.01285
0.5 M NaCl	0.8268	0.3569	0.4699	19.26	0.01414

scan rate increases, the CV profile deviates from the ideal capacitive behavior. This is mainly because the redox reactions depend on the insertion-deinsertion of the alkali ion or protons from the electrolyte. At slower scan rates, the diffusion of ions from the electrolyte can gain access to almost all available pores on the electrode surface, leading to a complete insertion reaction, indicating excellent capacitive behavior and a low contact resistance However, the curve shape is gradually distorted from rectangular to quasi-rectangular with an increase of the scan rate from 10 mV/s to 50 mV/s. The experimental information shows the redox reactions for all electrolytes, as indicated by the moderately large $E_0 - E_R$ and Rct. However, the $E_0 - E_R$ of electrode in 0.5 M NaOH was merely 0.0221 mV and 15.15 Ω, as shown in Fig. 4(a) to (d), which is smaller than that of the different electrolytes as seen the Table 1. This indicates that the capacitive behavior of the given electrode in 0.5 M NaOH is better than the other electrolytes.

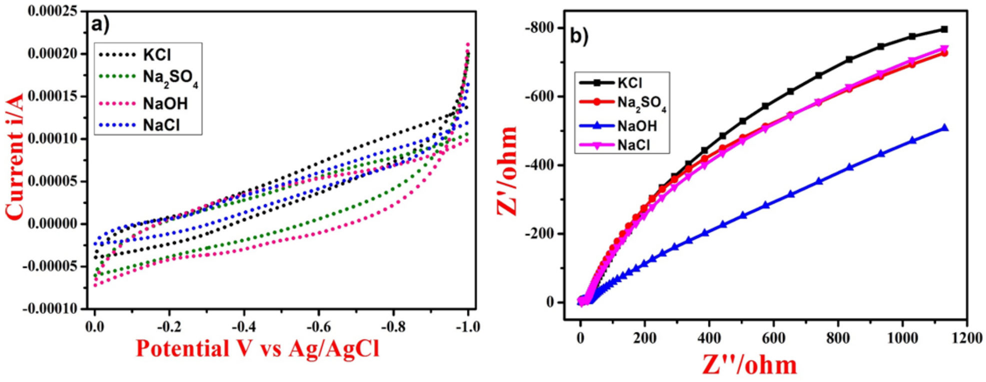

FIG. 2. a) Cyclic voltagramms of MnO_2 different electrolytes; b) Impedance spectra of MnO_2 electrode

5. Photocatalytic Activity of MnO_2

The photocatalytic enactment of the as-prepared sample was assessed through the photocatalytic degradation of Rhodamine-B (RB) and Indigo carmine(IC) under visible light irradiation. In these experiments, 60 mg of MnO_2 was dispersed in 250 ml IC (20 ppm) and similarly Rhodamine-B aqueous solutions respectively. The mixed suspensions were first magnetically stirred in the dark for 30 min to reach the adsorption-desorption equilibrium. Under stirring at ambient conditions, the mixed suspensions were exposed to visible light irradiation produced by a 400 W metal Philips lamp (wavelength: 254 nm). At certain time intervals, 5 ml aliquots of the mixed suspensions were extracted. The filtrates were analyzed by recording UV-vis spectra of RB and IC using a Spectratreats 3.11.01 Release 2A UV–vis spectrophotometer.The UV-vis absorption of MnO_2 show an intense absorption band in the range 200 to 220 nm. In Fig. 5 shows the UV-vis absorption spectra of RB and IC as a function of the catalytic reaction time [11]. Both RB and IC solutions turns colorless after 30 min, which indicates complete degradation of the dye molecules by MnO_2. After 30 min of reaction, the MnO_2 showed a higher efficiency in degradation of IC compared to RB. During the process of IC and RB degradation, the MnO_2 is reduced to Mn^{2+}, and leaches into the water and 74 % degradation is achieved under optimal conditions. It was determined that using the as-recovered MnO_2 Nano particle from waste dry cells, the dye solutions with concentration 60 mg/L can be degraded up to 74 % and mineralized up to 24 % in 45 minutes.

6. Conclusion

In this study, an aqueous technique was utilized to recover MnO_2 nanoparticles from waste dry cells by hydrometallurgy. Highly porous nano-MnO_2 is effectively recovered. Electrochemical estimations meant that the

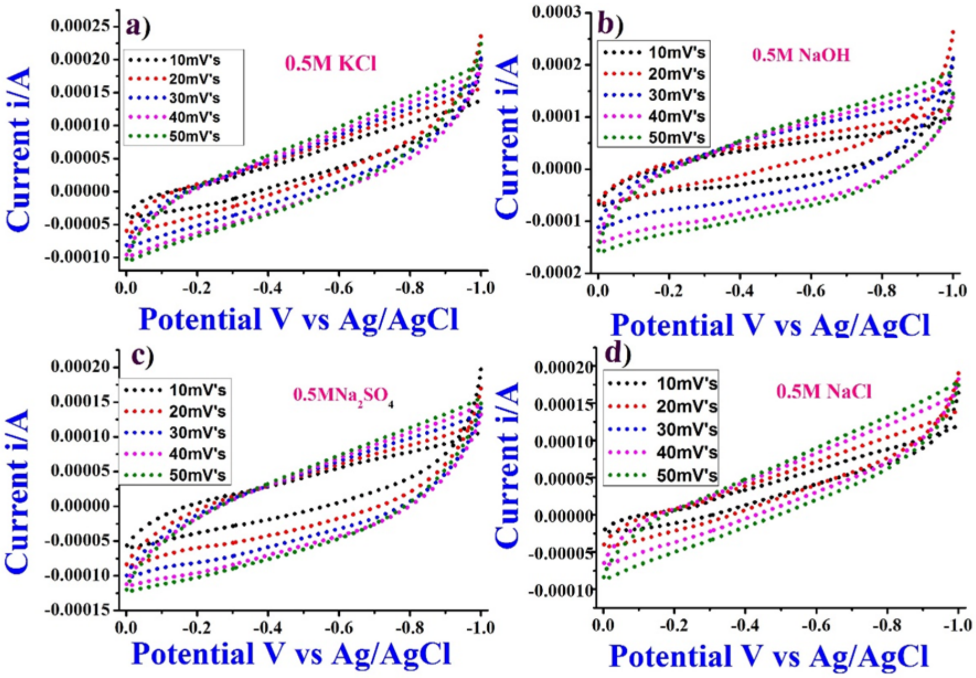

FIG. 3. Different scan rate of MnO_2 in different electrolytes

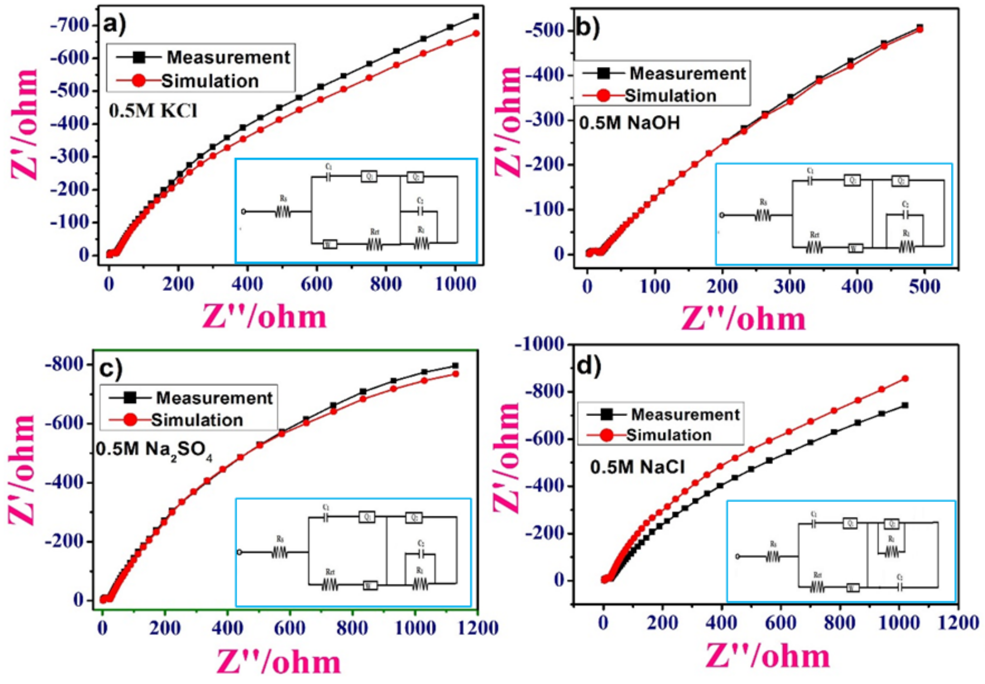

FIG. 4. Nyquist plots and equivalent circuit for MnO_2 electrode in different electrolytes

MnO_2 obtained displayed high electrochemical activity when the precipitates are kept at 100 °C for 24 hrs. The electric limit of this example demonstrated to be superior in correlation with the business tests. This showed that the MnO_2 had the best electrochemical execution at a high sweep rate of 10 mV/s. The recovered specimen displayed low charge exchange resistance (Rct) and high capacitive authorization. The morphology and crystallinity of MnO_2 improve in catalytic enactment in degradation of RB and IC. Using the as-obtained MnO_2, the IC solution with concentration 60 mg/L was shown to be degraded up to 74 % and mineralized up to 24 % and RB up to 72 % in 45 minutes.

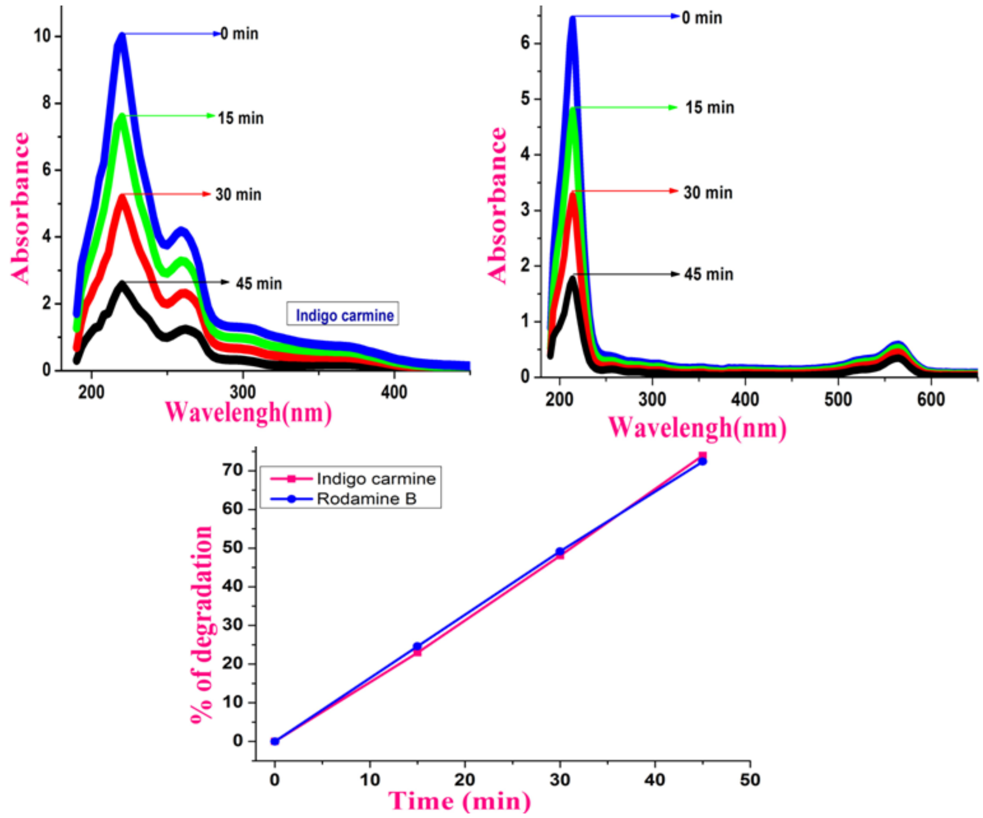

FIG. 5. UV-vis absorption spectra of RB and IC as role of time catalyzed by MnO_2

References

[1] Gallegos M.V., Falco L.R., et al. Recovery of manganese oxides from spent alkaline and zinc-carbon batteries. An application as catalysts for VOCs elimination. *Waste Management*, 2013, **33**, P. 1483–1490.

[2] Sobianowska-Turek A., Szczepaniak W., Zab-locka-Malicka M. Electrochemical evolution of reducers – Recovery of Mn from Zinc-Mn and Zinc-C battery waste. *Journal of Power Sources*, 2014, **270**, P. 668–674.

[3] Baba A.A., Adekola A.F., Bale R.B. Development of a combined pyro-and hydro-metallurgical route to treat spent Zinc-carbon batteries. *Journal of power sources*, 2009, **171**, P. 838–844.

[4] Macolino P., Manciulea A.L., et al. Manganese recovering from alkaline spent batteries by ammonium peroxodisulfate. *Acta Metallurgica Slovaca*, 2013, **19** (3), P. 212–222.

[5] Andrade Tacca C.A., Duart M.M.E. Acid leaching and electrochemical recovery of manganese from spent alkaline batteries. 2nd Mercosur Congress on Chemical Engineering and 4th Mercosur Congress on Process Systems Engineering.

[6] SiXu Deng, Dan Sun, et al. Synthesis and electrochemical properties of MnO_2 nanorods/graphene composites for supercapacitor applications. *Electrochimica Acta*, 2013, **111**, P. 707–712.

[7] Devreese J.T., Evrard R.P., Van Doren V.E. *Highly Conducting One-DimensionalSolids*. Plenum, New York, 1979.

[8] Pandey B.K., Shahi A.K., Gopal R. Synthesis, optical properties and growth mechanism of MnO nano structures. *Applied Surface Science*, 2013, **283**, P. 430–437.

[9] Kursunoglu S., Kavya M. Dissolution and precipitation of Zinc and Manganese obtained from spent Zinc-carbon and alkaline battery powder. *Physicochem. Probl. Miner Process*, 2014, **50**, P. 39–53.

[10] Buzatu M., Aceanu S.S., et al. Recovery of zinc and manganese from spent batteries by reductive leaching in acidic media. *Journal of power sources*, 2014, **247**, P. 612–617.

[11] Chanhlin Yu, Gao Li, et al. Fabrication,characterization of β-MnO_2 micro rod catalysts and their performance in rapid degradation of dyes of high concentration. *Catalysis Today*, 2014, **224**, P. 154–162.

NANOSYSTEMS: PHYSICS, CHEMISTRY, MATHEMATICS, 2016, 7 (4), P. 662–666

Synthesis and characterization of nano ZnO and MgO powder by low temperature solution combustion method: studies concerning electrochemical and photocatalytic behavior

K. N. Shravana Kumara[1,2], H. P. Nagaswarupa[1*], K. R. Vishnu Mahesh[3,4], S. C. Prashantha[1],
M. Mylarappa[5,6], D. M. K. Siddeshwara[7,2]

[1]Research Centre, Department of Science, EWIT, Bengaluru-560091, India
[2]Research and Development Centre, Bharathiar University, Coimbatore-641046, India
[3]Department of Chemistry, Dayananda Sagar College of Engineering, Bengaluru-78, India
[4]Dr. Premachandra Sagar Center for Advance Functional Materials, DSCE, Bengaluru-78, India
[5]Research Centre, Department of Chemistry, AMC Engineering College, Bengaluru-83, India
[6]Department of Studies and Research in Chemistry, B.H Road, Tumkur University Tumkur, Karnataka, India
[7]Department of Chemistry, Jyothi Institute of technology, Bengaluru-560062, India

*nagaswarupa77@gmail.com

PACS 81.07. -b **DOI 10.17586/2220-8054-2016-7-4-662-666**

The objective of the research was mainly focused on the synthesis of ZnO and MgO nanoparticle by low temperature solution combustion method using Urea as fuel. The accurate size and morphology of the nanoparticles were studied from Transmission Electron Microscopy (TEM) to assess the structure of the ZnO and MgO particles. The phase composition of the Synthesized ZnO and MgO nanoparticles were confirmed from powder X-ray diffractometer (PXRD). The electrochemical impedance spectroscopy (EIS) shows the charge transfer capacity was more in the electrode with zinc oxide compared to magnesium oxide. Cyclic voltammetry studies were performed to ascertain the electrochemical reversibility of electrode.We evaluate the photocatalytic activity of nanoparticles shows rapid color removal and reduction in the concentration of dyes.

Keywords: Synthesis, ZnO, MgO, electrochemical and photo catalytic behavior.

Received: 5 February 2016

Revised: 1 May 2016

1. Introduction

The photocatalytic degradation efficiency and mineralization degree of dyes are limited because of the slow interfacial electron transfer. In recent years, the light-converting materials have attracted tremendous attention for photocatalysis and solar energy collection which can be easily absorbed by a given dye and thus effectively excite the dye to generate more electron-hole pairs, resulting in the improvement of the self-sensitized dye degradation. In this work, we report the photocatalytic degradation of Methylene Blue (MB) and Methyl Orange (MO) under visible light irradiation by using ZnO/MgO nanoparticles synthesized by a solution combustion method [1]. It was found that ZnO/MgO particles exhibited high enhancement of visible light photocatalytic performance in the degradation of MB and MO.

Currently, inorganic nano metal oxides (TiO_2, MgO, CaO and ZnO) are attracting research interest due to their safety, stability and multifunctional properties [2]. Design of materials which can be efficiently trapped and transfer energy in the form of charges is a major challenge in photocatalysis, photoluminescence (PL) and solar energy conversion fields. However, less progress has been made for nanomaterials, which often exhibit their unique size dependent physical/chemical properties due to their large surface-to-volume ratio and quantum confinement effects. Zinc oxide finds a wide range of applications as photocatalyst, lasers, white light emitting diodes (WLEDs), sensors, antireflection coatings, antibacterial, antifungal, solar cell material, varistors, optical devices, piezoelectric devices, optoelectronic devices, photonics etc [3].

The aim of the work is the synthesis of ZnO and MgO Nanoparticle with Urea as a fuel by using low cost solution combustion method. The cyclic voltammetry and photocatalytic activity were carried out to predict the properties of prepared samples.

2. Experimental

2.1. Synthesis of ZnO/MgO nano particles

In a synthesis, according to the stoichiometric ratio and molar mass of Zinc Nitrate ($ZnNO_3{\cdot}6H_2O$), Magnesium Nitrate ($MgNO_3{\cdot}6H_2O$) and Urea (NH_2CONH_2) were dissolved in a small amount of distilled water. Then, the solution was heated in a furnace 10 to 15 minutes at 450 °C. After the reaction was complete, the resulting white product was crushed into a fine powder. Then, the as-synthesized products were calcined at 500 °C for 4 h in air to obtain ZnO/MgO nanoparticles [4]. Stoichiometric compositions of the metals nitrates (oxidizers) and urea (fuel) were calculated using the total oxidizing and reducing valences of the components which serve as numerical coefficients for stoichiometric balances.

$$6\mathrm{Zn(NO_3)_2} + 10\mathrm{NH_2CONH_2} \rightarrow 6\mathrm{ZnO} + 10\mathrm{CO_2} + 20\mathrm{H_2O} + 16\mathrm{N_2}, \tag{1}$$

$$6\mathrm{Mg(NO_3)_2} + 10\mathrm{NH_2CONH_2} \rightarrow 6\mathrm{MgO} + 10\mathrm{CO_2} + 20\mathrm{H_2O} + 16\mathrm{N_2}. \tag{2}$$

2.2. Characterization

X-Ray diffraction analyses were carried out using a high resolution X-ray Diffractometer Maxima-7000 (Shimandzu) at a scanning rate of 2 $^\circ\mathrm{min}^{-1}$ using CuKα radiation (λ = 1.54 Å) operating at 40 kV and 30 mA. TEM was used to study the accurate size and morphology of the ZnO/MgO. TEM images of the ZnO/MgO were obtained at 80 kV under high resolution TEM instrument (JEOL, Japan, and JEM-1011). Cyclic voltammetry and electrochemical impedance were measured by Electrochemical workstation CHI604E. The samples were analyzed by recording UV–vis spectra of MB and MO, using a Spectra treats 3.11.01 Release 2A UV–vis spectrophotometer.

3. Result and discussion

3.1. X-Ray diffraction

The average crystalline size, structure and phase of sample were determined using XRD in the 2θ range from 20 – 700 at a scanning rate of 2 $^\circ\mathrm{min}^{-1}$. Using the peak width at half maximum height and peak position (2θ) in the XRD spectra, the inter layer space can be calculated utilizing Bragg's law:

$$n\lambda = 2d\sin\theta, \tag{3}$$

where λ is wave length of X-ray radiation used in the diffraction experiments, d is the space between layers in the clay lattice and θ is the measured diffraction angle.

The XRD form of ZnO/MgO nanoparticles obtained from solution combustion synthesis were as shown in Figs. 1(a) and 1(b). The peaks at 2θ values of 31.71, 34.41, 36.21, 47.46, 56.57, 62.76 and 67.94 ° corresponded to the crystal planes of (100), (002), (101), (102), (110), (103) and (112) of zinc oxide nano particles. The diffraction peaks could be referring to the spherical phase, which was evaluated with the data from JCPDS card No. 89-7102. The strong and narrow peak denotes that the product particles have a well-formed crystalline nature. The particle average size was calculated by the Scherrer formula and found to be in the range of 38 nm. In Fig. 1(b), the XRD results of MgO revealed that the structure was in cubic structure and these results were matched with JCPDS card number 75-1525. Peaks were absorbed at 36.8, 42.8, 62.1, 74.6 and 78.5 ° along with miller indices values (111), (200), (220), (311) and (222) respectively. As the width of the peak increases, the size of particle size decreases, which appears to make the present material in the nano range. The average crystallite size was measured as 40 nm.

3.2. Transmission electron microscopy

Transmission Electron Microscopy (TEM) is useful to understand if amorphous or crystalline sized particles are smaller. The TEM images of ZnO and MgO nano particles were shown in the Figs. 2(a) and 2(b) respectively. From Fig. 1(a), it is clearly shown that, ZnO exhibits nearly circular/spherical like structure and Fig. 1(b) indicating MgO exhibits the hexagonal shape and very homogeneous crystal structures without any observable pores.

3.3. Cyclic voltammetry studies

Cyclic voltammetry (CV) and electrochemical impedance measurements were carried out using CHI604E electrochemical workstation. For cyclic voltammetry studies, the test electrode was prepared by grinding the combination of 20 % prepared ZnO/MgO Nano powder, 70 % graphite powder and 10 % silicone oil used as binder and resulting pasted on a disk electrode. A platinum foil was used as a counter electrode; Ag-AgCl electrode as a reference electrode and 0.5 M Na_2SO_4 solution as electrolyte. All measurements were carried out at room temperature. The representative CV curves for ZnO/MgO are shown in Figs. 3(a,c,d) with different scan

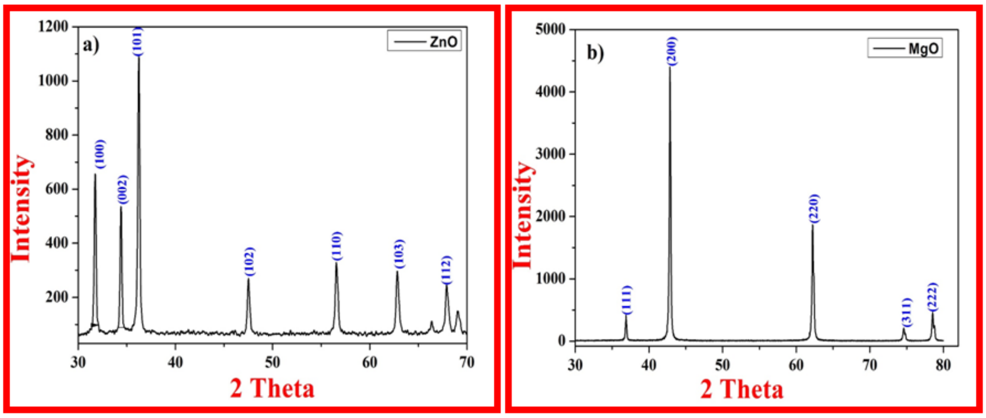

FIG. 1. XRD images of ZnO and MgO nano particles

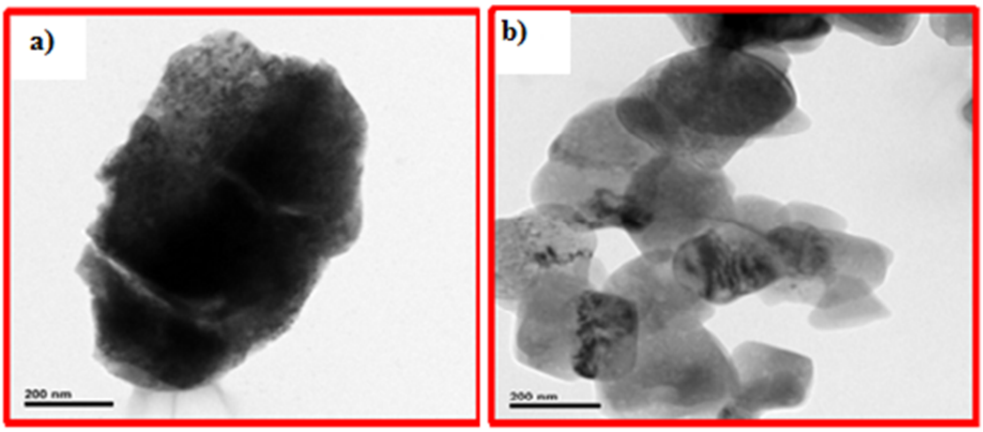

FIG. 2. TEM images of ZnO and MgO nano particles

TABLE 1. Electrochemical reversibility and EIS of ZnO/MgO Electrodes

Electrode	**Electrolyte**	$\mathbf{E_O}$ **(V)**	$\mathbf{E_R}$ **(V)**	$\mathbf{E_O - E_R}$	$\mathbf{Rct(\Omega)}$	$\mathbf{C(F) \times 10^{-5}}$
ZnO	Na_2SO_4	0.2988	0.2739	0.0249	12.01	2.801
MgO	Na_2SO_4	0.2986	0.2639	0.0347	16.09	0.0326

rates. Increasing the scan rate from 10 mv to 50 mv, increases the oxidation and reduction of peaks for ZnO/MgO samples. The comparative CV results of electrodes ZnO/MgO at a scan rate of 0.01 V/s are tabulated in Table 1. The data there confirm that the electrochemical reversibility of ZnO is superior than that of MgO. Therefore, ZnO is more suitable for electro and photo catalytic activity applications. These results indicate that the charge and discharge process of the ZnO pasted electrode shows better electro chemical reversibility than MgO pasted electrodes. Fig. 3(b) represents the electrochemical impedance spectra (EIS) of the ZnO/MgO pasted electrodes. The impedance spectra of all these electrodes display a depressed semicircle considerable from charge transfer resistance (Rct) in the high-frequency region, corresponding to Rct in parallel connection with the capacitance (C) and the line at low frequency regions corresponds to Warburg impedance (W) of proton diffusion. A decrease in the charge transfer resistance and an increase in the capacitance indicate that ZnO-paste electrode shows more surface electrochemical activity than that of MgO-paste electrode.

3.4. Photocatalytic studies

In the current work, Methylene blue (MB) and Methyl orange (MO) dyes were used as pollutants in our models to assess the photocatalytic activity of ZnO/MgO under UV light irradiation. 60 mg of ZnO/MgO was spread in 250 ml MB (20 ppm). The mixed suspensions were first magnetically stirred in the dark for 30 min

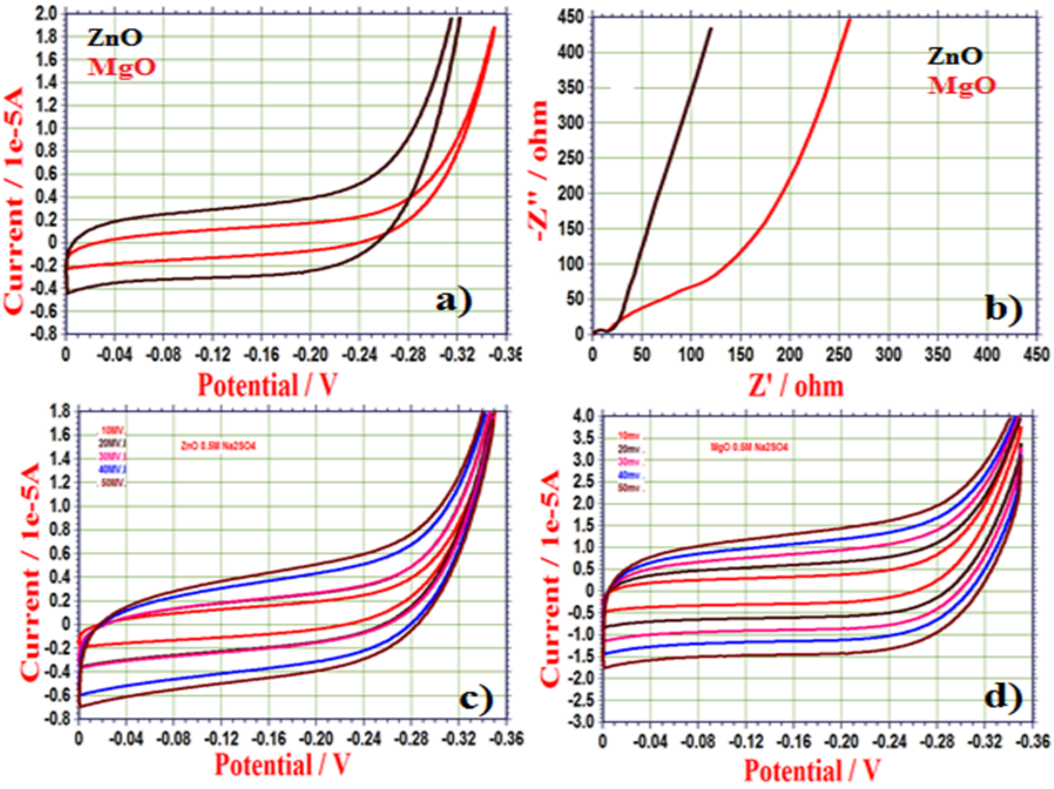

FIG. 3. Cyclic voltagramms and EIS of a) ZnO b) MgO with different scan rate

to reach the adsorption-desorption equilibrium. Under the ambient conditions and stirring, the mixed suspensions were open to visible light irradiation created by a 400 W metal Philips lamp (wavelength: 254 nm). At certain time intervals, 5 ml aliquots of the mixed suspensions was extracted. The filtrates were analyzed by recording UV-vis spectra of MB and MO using a Spectratreats 3.11.01 Release 2A UV-vis spectrophotometer. In UV light, RGO/ZnO can absorb UV light (254 nm) and generate electron-hole pairs. These photo-produced electron and hole pairs can travel into the catalyst surface and react with surface adsorbed O_2 to form active oxygen species. Photo degradation of MB and MO by ZnO/MgO nanoparticles was studied. In Figs. 4(a) to (b) show the UV-vis absorption spectra of MB and MO as a function of the catalytic reaction time. Both MB and MO solutions turns colorless after 60 min that specifies that complete degradation of the dye molecules by ZnO/MgO. After 60 min of reaction, the ZnO/MgO, Showed a good catalytic degradation of MO. It was observed that by using prepared composite material, the MB solution with concentration of 60 mg/L can be degraded up to 93 % in 60 minutes, whereas the MO was degraded up to 76 % using ZnO particle. Additionally, 98 % and 91 % of MB and MO respectively were degraded using MgO nanoparticles.

4. Conclusion

In the present work, ZnO and MgO were prepared by simple and low cost solution combustion method at low temperatures (400 °C). The average grain sizes of ZnO and MgO nanoparticles were found to be 38 nm and 40 nm, which are confirmed by XRD results. The ZnO pasted electrode showed better electro chemical reversibility than the MgO pasted electrode. A decrease in the charge transfer resistance and an increase in the capacitance indicate that ZnO pasted electrode shows more surface electrochemical activity than that of MgO pasted electrode. The photocatalytic activity of ZnO/MgO nanoparticles showed a good catalytic degradation of MB and MO. This indicates that using as-prepared composite material, the MB and MO solution with concentration 60 mg/L can be degraded up to 98 % and 93 %, MO degraded up to 91 % and 76 % in 60 minutes using ZnO and MgO particles.

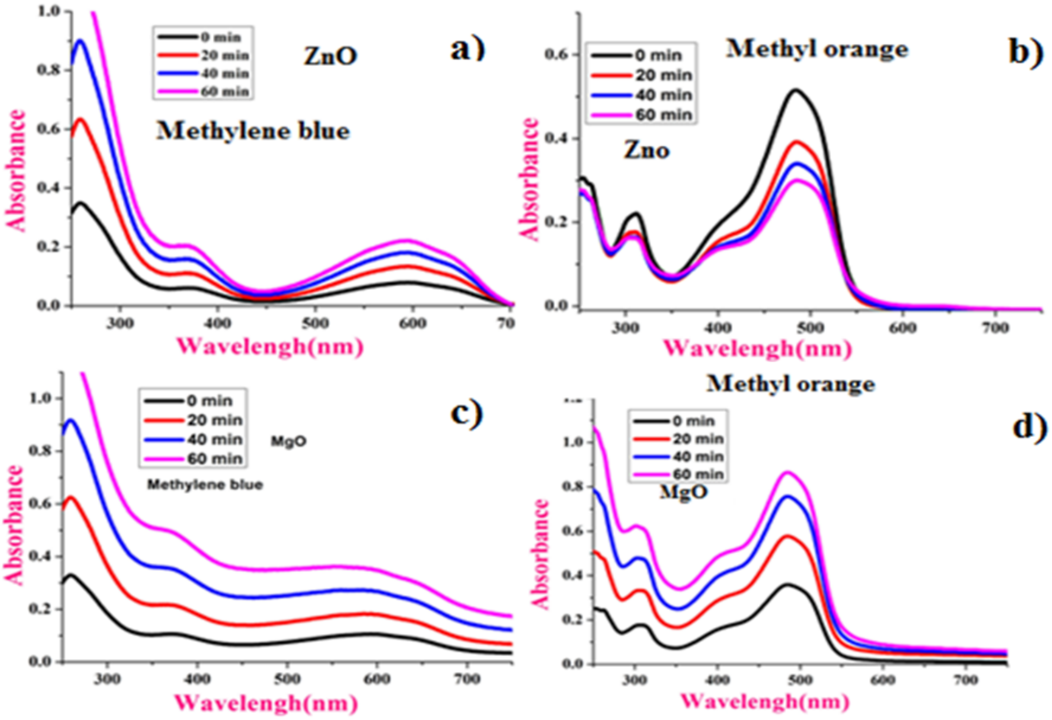

FIG. 4. UV-visible absorption spectra of MB and MO catalysed by ZnO and MgO

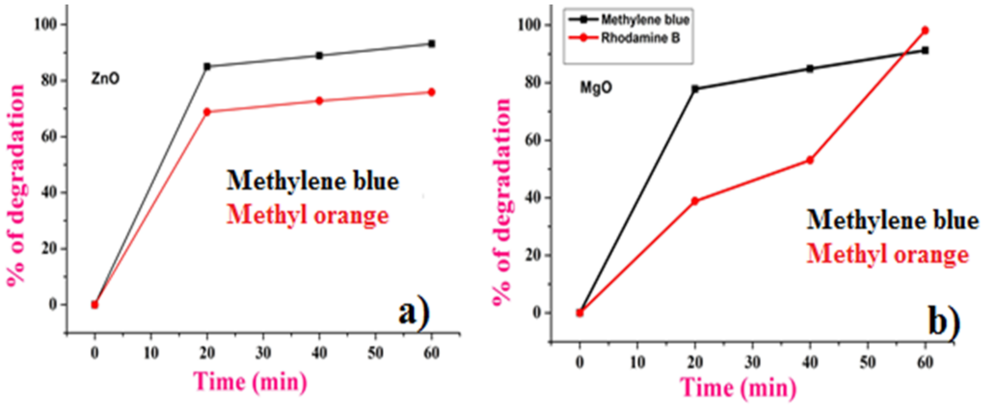

FIG. 5. Effect of Degradation of MB and MO by ZnO and MgO

References

[1] Park J.Y., Lee Y.J., et al. Chemical synthesis and characterization of highly oil dispersed MgO nanoparticles. *J. Ind. Eng. Chem.*, 2006, **12**, P. 882–887.

[2] Naik R., Prashantha S.C., et al. Low temperature synthesis and photoluminescence properties of red emitting Mg_2SiO_4: Eu^{3+} nanophosphor for near UV light emitting diodes. *Sensors Actuators B*, 2014, **195**, P. 140–149.

[3] Anilkumar M.R., Nagaswarupa H.P., et al. Bio-inspired route for the synthesis of spherical shaped MgO:Fe^{3+} nanoparticles: Structural, photoluminescence and photocatalytic investigation. *Spectrochimica Acta Part A: Molecular and Biomolecular Spectroscopy*, 2015, **149**, P. 703–713.

[4] Patil K.C., Hegde M.S., Tanu Rattan, Aruna S.T. *Chemistry of Nanocrystalline Oxide Materials, Combustion Synthesis, Properties and Applications*. World Scientific Publishing Co. Pt. Ltd., UK, 2008.

NANOSYSTEMS: PHYSICS, CHEMISTRY, MATHEMATICS, 2016, 7 (4), P. 667–674

Preparation of chitosan/different organomodified clay polymer nanocomposites: studies on morphological, swelling, thermal stability and anti-bacterial properties

B. H. Nanjunda Reddy[1,a], V. Venkata Lakshmi[*,2], K. R. Vishnu Mahesh[**,3], M. Mylarappa[2,a], N. Raghavendra[4] and T. Venkatesh[5]

[1]Department of Chemistry, Amrita School of Engineering, Bengaluru, Campus, Amrita Vishwa Vidyapeetham University, Bangalore–560035, Karnataka, India

[a]Department of Studies and Research in Chemistry, B.H̃ Road, Tumkur University, Tumkur–572103, Karnataka, India

[2]Research center, Department of Chemistry, AMC Engineering College, Bengaluru–560083, India

[3]Department of Chemistry, Dayananda Sagar College of Engineering, Sahvige Malleshwara Hills, Kumara Swamy Layout, Bangalore–560083, Karnataka, India

[4]CMRTU, RV College of Engineering, Bengaluru–560059, Karnataka, India

[5]Department of Chemistry, ACS College of Engineering, Bengaluru–560074, Karnataka, India

[*]laxmimurthy@rediffmail.com, [**]vishnumaheshkr@gmail.com

PACS 83.80.-k **DOI 10.17586/2220-8054-2016-7-4-667-674**

In the current study, chitosan films were prepared by dispersing different commercially-modified nanoclays, such as C-Na, C-10A, C-15A, C-30B, and C-93A. The exfoliation and morphology were studied using XRD and SEM. The C-15A, C-30B and C-93A nanoclays/Cts BNCs (Bionanocomposites) showed very good uniform exfoliation compared to that of other clays. The thermal analyses were evaluated using DSC and TGA. These results also confirmed that because of exfoliation, the thermal properties were improved in the case of C-15A, C-30B and C-93A nanoclays/Cts BNCs. The swelling capacity of a chitosan/clay films were studied. Increasing the chitosan content in the film increased the swelling capacity significantly; the decreasing order of swelling capacity of Cts/Clay films is in accordance with the decrease in clay content. Greater swelling capacity is shown by films Cts, C-Na and C-10A is because of the presence of greater hydrophilic agencies in the film makeup, which assist in improving the swelling characteristics of the films. The antibacterial activities of Cts/clay were also investigated against Gram-negative and Gram-positive bacteria (*E. coli* and *S. aureus*) according to the zone of inhibition in the disc diffusion method.

Keywords: chitosan, clay, bio-nanocomposites, swelling property and anti-bacterial property.

Received: 5 February 2016

Revised: 11 May 2016

1. Introduction

In the most recent decade, polymer/clay composites have received much attention because of their astonishing ability to improve most of the properties and are an essential alternative to standard polymer composites. The intercalation of polymers into the gallery of the clays brings greater characteristics to hybrid materials [1–4]. In comparison to the vast research on polymer/clay composites, the quantity of biopolymer/clay composites research is comparatively smaller [5–7]. Chitosan (Cts) is a polysaccharide that consists of N-acetyl-glucosamine and N-glucosamine units and it is largely insoluble at neutral and alkaline pH, given that its pKa within the variety of 6.2–7.0 is one of the second most plentiful natural polymers after cellulose in the world, naturally obtained and is derived by deacetylation of chitin present in crustaceous species [8, 9]. In addition to its unique properties such as biocompatibility, biodegrability and non toxicity, it is widely used in biotechnology, pharmaceuticals, cosmetics, textiles agriculture fields due to its antifungal and antimicrobial activities [10]. Unmodified chitosan is not antimicrobially energetic at pH 7, since it does not dissolve or include a large number of charges on the amino groups. The antimicrobial activity of chitosan also increases with increasing degree of deacetylation, due to the increasing number of basic amino groups.

Montmorillonite (MMT) is a member of the smectite group minerals which has a layered shape or platelets. Because of its high aspect ratios and excessive surface area, if clay particles are properly dispersed in a polymer matrix at a loading level of 1–5 % (w/w), precise mixtures of physical and chemical properties may be enhanced, and in turn those composites become more attractive for making films and coatings for a multiplicity of commercial applications, such as drug delivery systems and antimicrobial systems due to their natural abundance and the propensity with which they can be chemically and physically modified for drug delivery applications [11, 12]. Montmorillonite has been appreciably implemented for prolonged release of drugs as it could hold large amounts of drug due to its excessive cation exchangeability. The surface adsorption of various drugs like griseofulvin, indomethacin and prednisone to montmorillonite clay improves their dissolution rate. The hydrophilic and swelling properties of montmorillonite in aqueous media help to facilitate the wetting of hydrophobic drug substances. This clay ultimately improves the bioavailability of drugs.

Cts are capable of engaging with negatively charged clay, which has a silicate layer shape. When Cts dispersions have been blended with clays, the zeta potentioability of clays and the viscosities of the composite dispersion have been changed [13]. The dry fabric acquired from those composite dispersions is called a nanocomposite if the Cts intercalates into the silicate layer of the clay. Different types of clays, such as montmorillonite and rectorite, have all been used to prepare nanocomposite substances with Cts [14–17]. Within the practice method of these substances, it is necessary to use a heating treatment on the composite dispersion to initiate the nanocomposite formation [15, 18] Furthermore, the clay content material stimulated thermal stability and mechanical properties of the nanocomposites [16, 18]. Cts-clay nanocomposites have been developed and characterized for use as biosensors, packaging materials and superabsorbent substances [19–21]. Furthermore, Cts–clay films should retard the release of a bioactive agent integrated into the films. The current objective of these studies, in particular, targeted the impact of various organo-modified nanoclays on the properties of chitosan (Cts) based Bio-Nanocomposites (BNCs).

2. Experimental

2.1. Materials

Low molecular weight chitosan (CS) used in this work was bought from Sigma Aldrich Chemicals, Bangalore, and Karnataka, India. The Clays such as C-Na, C-10A, C-15A, C-30B, and C-93A were procured form Southern Clay Products, USA. Acetic acid and sodium hydroxide were obtained from Sigma Aldrich Chemicals, Bangalore, and Karnataka, India.

2.2. Preparation of clay/chitosan nanocomposites

The 2 % wt/vol of chitosan solution was prepared by dissolving it in 1 % acetic acid (pH=4.0) with continuous magnetic stirring for 30 min. and then allowed to sit overnight for complete dissolution, or alternatively, 3 % wt/vol ratio of clay (based on the chitosan wt.) was used. Therefore, an appropriate quantity of different clays were dispersed in 10 ml of 1 % acetic acid and magnetically stirred continuously for 24 hours at room temperature and ultrasonicated for about 30 minutes, for this solution, the as already prepared chitosan solution was transferred very slowly and this mixture was stirred for an additional 4 hours using magnetic stirrer. The resulting solution was carefully poured into Teflon-coated glass plates and kept overnight in a 60 °C oven. The resulting composite films were soaked in 1 % NaOH solution for 30 minutes to remove excess acidic content, followed by washed with distilled water several times to effect the removal of NaOH. Then, the composite films were peeled off from the glass plates and the resulting films again oven dried. Films were packed in air tight polyethylene pouches for further characterizations. A similar procedure was followed for the other clay sample dispersion in a chitosan matrix.

3. Results and discussion

3.1. X–Ray diffraction

The Fig. 1 shows the XRD patterns of neat Cts, Cts/C-Na, Cts/C-10A, Cts/C-15A, Cts/C-30B and Cts/C-93A nanocomposites with addition of 3 wt% of above commercial clays. The XRD pattern of Cts suggests the characteristic crystalline peaks at round 20 °. In line with the literature, after incorporation of clay inside Cts matrix the basal plane of Cts/C-Na at 2θ=7.2 ° which disappears and which will be substituted by new peak at around 6 ° whose d-spacing d=1.47 nm. The shift of the basal reflection of C-Na to a lower angle indicates the formation of an intercalated nanostructure, even as the peak broadening and lower depth most likely indicate a disordered intercalated or partially-exfoliated structure, in the case of unmodified C-Na, the inter space distance (d001) turned into enlarged from 1.23 to 1.47 nm (information required for specific composites Cts/93A, 15A, 30B)(approximate d-spacing values for C93A, C30B, C15A, C10A are 3.68, 3.53, 3.4, 3.27 respectively in accordance with graph). According to the XRD report, partial exfoliation is achieved only in the sample containing 3 % C-Na unmodified clay but no uniform exfoliation was noted for the composites of C-15A, C-30B and C-93A. However, according to SEM reports, partial exfoliation was achieved for the sample Cts/C-10A and same trend was observed in Fig. 1.

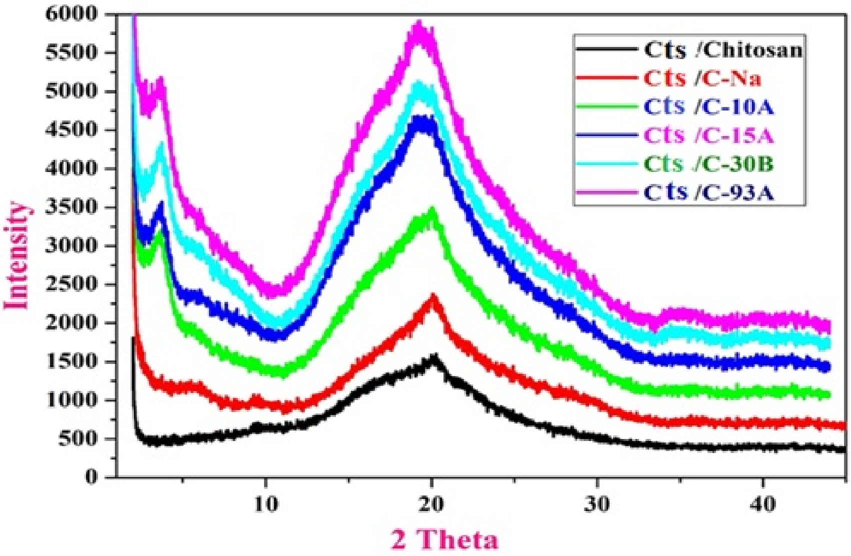

FIG. 1. XRD Pattern of chitosan with different organo modified clay

3.2. Fourier transfer infrared spectroscopy

FTIR was used to characterize the chemical interactions with Cts and clay in the nanocomposites. The organic cations in the clay may additionally comprise diverse useful functional groups that react with chitosan resin to improve interfacial adhesion among clay monolayer and polymer matrix, hence, this cation exchange effect is characterized by the enhancement of the magnitude of the 3193–3187 cm^{-1} band in conjunction with a reduction of intensities because of Si-O and Al-O. The enhanced intensity of the 3193–3187 cm^{-1} band displays the increased hydrogen bonding among the lattice hydroxyls and organic groups. Whilst the protons inside the chitosan are hydrogen bonded oxygen species of Si-O and Al-O segments, Si-O and Al-O bonds might be weakened and the tetrahedral symmetry of these moieties may be distorted. The FTIR spectrum of the clay shows the characteristic bands at 1662 cm^{-1} because of H-O-H bending, 1000 and 1182 cm^{-1} due to Si-O stretching 819 and 670 cm^{-1} due to (Al Mg)-OH vibration modes, while the IR spectra of Cts/C-10A showed additional peaks, including 1725 cm^{-1} (N-H bending), 1590 cm^{-1} (N-H bending) and 1455 cm^{-1} (C-H bending). The absorption band of the carbonyl(C=O) stretching for the secondary amide (amide first band) was observed at 1488 cm^{-1}. At 2356 cm^{-1}, the stretching frequency gradually increased from that of pure chitosan to C93A composite sample with the variation of the type of clay. FTIR was also used to study the polymer/clay interaction, since a shift in the δ_{NH3} vibration might be expected when $-\delta_{NH3}$ groups interact electrostatically with the negatively-charged sites of the clay. In fact, a shift of the δ_{NH3} band towards a lower frequency is noted in all the chitosan/clay films, as is shown in Fig. 2. However, this shift is higher for chitosan/clay films with the lowest amounts of chitosan, while the chitosan/clay films with the highest amounts of biopolymer show a frequency value the trend observed in the films of pure chitosan (Ct). This fact may be related to the $-\delta_{NH3}$ groups that do not interact electrostatically with the clay substrate (Fig. 2). The absorption frequency of pure chitosan in the range of 1721 to 1644 cm^{-1} was related to the vibrations of carbonyl bonds (C=O) of the amide group CONHR (secondary amide, ν_1 = 1721 cm^{-1}) and to the vibrations of protonated amine group (δ_{NH3}, $\nu_2 = 1644$ cm^{-1}).

3.3. Thermal analysis of Cts/clay composites using DSC and TGA

DSC showed two broad peaks for Cts/clay composites, one is an endothermic broad peak and the other one is an exothermic broad peak. The endothermic broad peaks for Cts, Cts/C-Na, Cts/C-10A, Cts/C-30B and Cts/C-93A composite films (as shown in Fig. 3) are: 273, 281, 297.5, 300, 271 and 292 °C respectively. The first temperature region is situated at high temperature in DSC curves because of heating rate used was higher 20 °C min^{-1}. The first peak could be assigned to the water loss, while the second to the decomposition of system components. It is bearing related to the thermal stability of nanocomposites. From these data, it can be concluded that nanocomposites of Ct/C-Na, Ct/C-10A, Ct/C-15A, Ct/C-30B and Ct/C-93A improved the thermal stability of chitosan. Additionally, for the degradation and deacetylation of chitosan and remaining residue at 270 °C and above, the decomposition in air is highly exothermic for the samples Ct/C-30B, Ct/C-93A. This may be due to

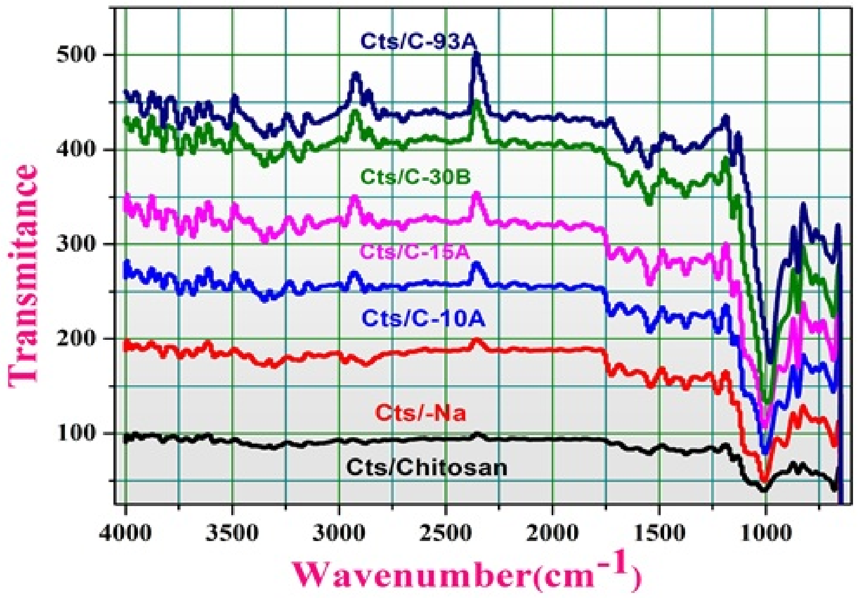

FIG. 2. FTIR patterns of chitosan with different organo modified clay composites

the surfactants used during the modification of these cloisites (C-30B, C-93A) and the same phenomenon was observed in the Fig. 4 (decomposition of intercalated Ct/C-30B and Ct/C-93A layers occurred in the vicinity of 270 °C with significant weight loss). It has been observed that the melting points and exothermic broad peaks all the composite films were 90, 75, 88, 95, 92, 83 °C respectively. The TG, glass transition behavior of Cts and Cts/clay bio-composite films were measured by the DSC evaluation. The TG and melting endothermic height of Cts 3 wt% of Cts/clay has been shifted from approxi. 50–130 °C. The DSC does not detect any traces of thermal transitions for 3 wt% of MMT/clay. The melting endothermic peak of Cts was observed at 140 °C at the same time as the height of Cts/Clay bio composites shown at 150–250 °C, the melting temperature expanded with increased clay content (3 wt%) within the Cts. For these composites, one can find two peaks in TGA curves. In the first stage, a smaller loss in weight 10–12 % was observed compared to the second stage (40 %).

The addition of nanoclays produces a thermal barrier and decreases the weight loss, thus inorganic particles are found to enhance the thermal stability of the chitosan composites. As can readily be seen, better thermal stability was observed for Cts/C-10A, Cts/C-15A, Cts/C-30B, Cts/C-93A composites. This is linked with more intercalation and exfoliation of the chitosan and inorganic fillers (clay). In air flow, another degradation step at 63 °C for the samples Cts/C-10A and Cts/C-93A was observed, the cause of which may be assigned to the oxidative degradation of carbonaceous residue formed during second step. The carbonaceous residue is greater in these samples because of the nature of the modifiers/surfactants which were used in the modification of cloisites.

3.4. Morphological study using SEM

The morphology of surfaces with different surface structure between MMT (clay) and chitosan films are shown in Figs. 5(a-f) using SEM data. The surface of Cts exhibits a smooth laminated structure; comparatively, the surface of composite films seems to be course, indicating an improved intercalation of Cts chains in the clay platelets. Thus, SEM analysis results agreed with the XRD analysis results that produced increase in basal spacing value which was relatively small. This small increase indicated that most of chitosan were on clay (MMT) surface because of formation of hydrogen bonds and intermolecular interactions of these polymers. The exfoliated structure was observed in XRD results. Those outcomes have been corroborated with the aid of SEM effects. The homogenous dispersion of nanoparticles and homogenous matrix in SEM photographs give proof for an exfoliated structure.

3.5. Swelling study

The swelling capacity of a chitosan/clay films performs an essential function regarding the antibacterial activity, wound recovery potential and for biomedical packaging because of their excessive water/solvent retaining potential. The Cts, Cts/C-Na, Cts/C-10A showed higher swelling capacity than Cts/C-15A, Cts/C-30B and Cts/C-93A films, and, among the all these samples, Cts/C-15A showed lowest swelling capacity. This may be because of more

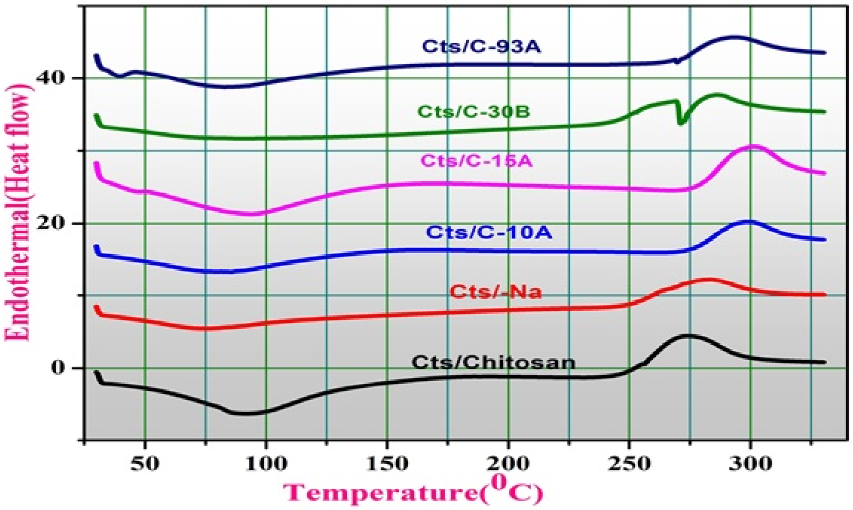

FIG. 3. DSC micrographs of chitosan with different organo modified clays

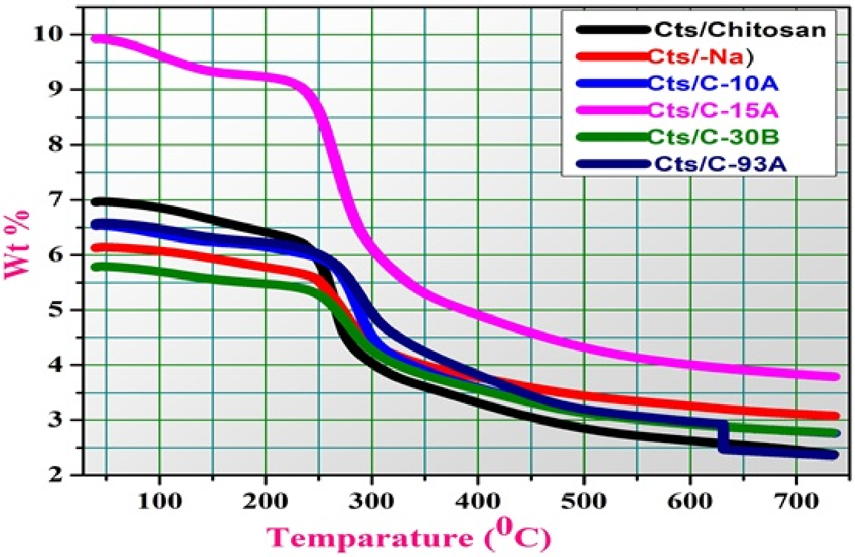

FIG. 4. TGA of chitosan with different organo modified clays

cross linking /interaction of clay with chotosan polymer chains for example, the swelling capacities of the samples were as follows: Cts-1.8 g/g; Cts/C-Na-1.85 g/g; Cts/C-10A 1.75g/g. The other films had the following values: Cts/C-15A-1.58 g/g; Cts/C-30B-1.5 g/g; Cts/C-93A-1.35 g/g respectively. The lowering of the swelling potential is attributed to the clay binding with Cts chains, i.e. the interplay of negative charges on the clay with ‘O’ and N–atoms of hydroxyl and amine groups present in Cts chains. This produces an additional cross links inside the chain networks. The higher degree of cross-linking with the film restricts the penetration of water for swelling. The increase in chitosan content in the film increases the swelling capacity significantly, the decreasing order swelling capacity of Cts/Clay films is in accordance with Cts/C-15A(1.35 g/g)< Cts/C-93A(1.5 g/g)< Cts/C-30B(1.58 g/g) ,Cts/C-10A< Cts/C-Na(1.7 g/g)< Cts(1.78 g/g) more swelling capacity is showed by films Cts,Cts/C-Na and Cts/C-10A is due to the presence of greater hydrophilic agents within the film network which assist in improving the films’ swelling properties (Fig. 6).

4. Antibacterial tests

The antimicrobial activity of chitosan and chitosan-based nanocomposite films were examined qualitatively via an inhibition zone method. In this technique, specific pathogenic microorganism such as *S. aureus* and *Escherichia*

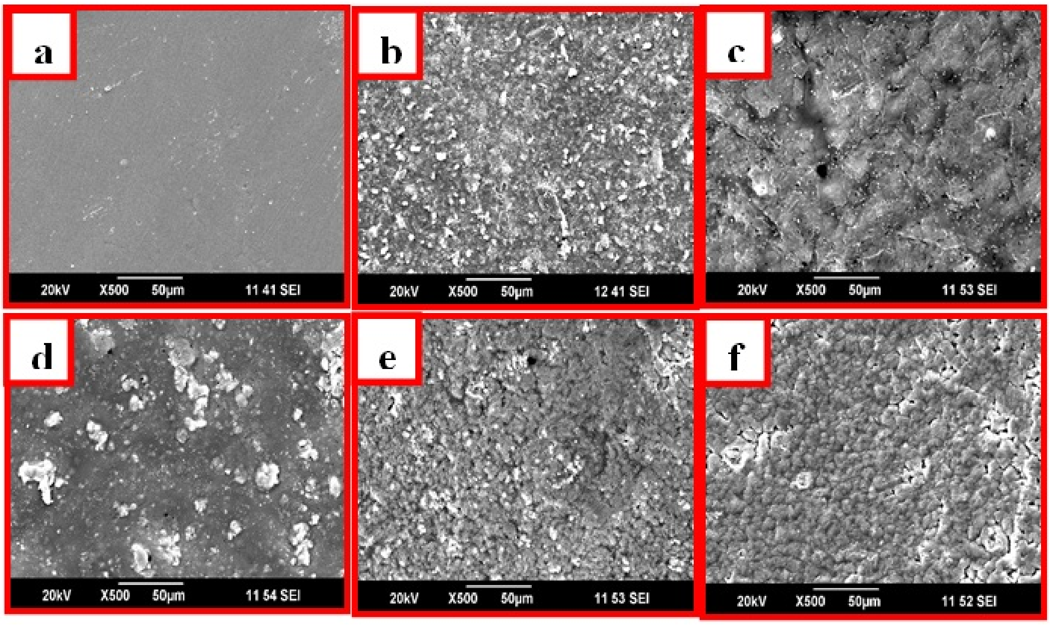

FIG. 5. SEM images of a) Pure Cts, b) Cts/C-NA, c) Cts/ C-10A, d) Cts/C-15A e) Cts/C-30B and f) Cts/C-93A

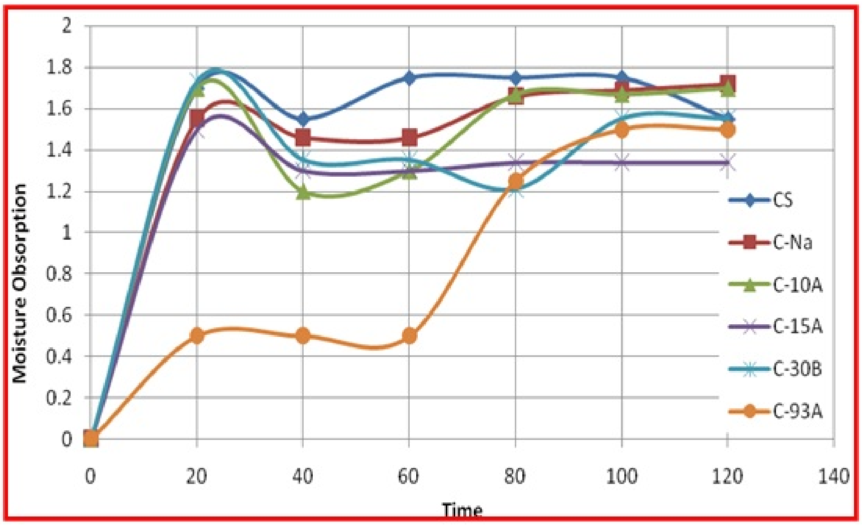

FIG. 6. Swelling behavior of chitosan with different organo modified clays

coli were used to assess the antimicrobial activity of the chosen two films. Both traces of *S. aureus* and *E. coli* were cultivated on tryptic soy (TS) agar (Difco Lab) at 30 °C for two days. All the stock cultures were saved at 4 °C. For the qualitative size of antimicrobial activity, the film samples were punched to make disks (diameter) 6 mm), and the antimicrobial activity present determined the use of a modified agar diffusion assay (disk check). The plates were examined for feasible clean zones after incubation at 37 °C for two days. The presence of any clear zone that shaped across the movie disk at the plate medium was recorded as an illustration of inhibition towards the microbial species. The qualitative antimicrobial activity of the films became determined the use of a quarter inhibition technique for testing pathogenic bacteria.

Pure chitosan film did not show any antibacterial properties. This effect of chitosan may be related fact that chitosan does not diffuse through the adjusted agar media in the agar diffusion test method, so that the only organism in direct contact with the active site of chitosan are inhibited [22–24]. The inhibition zone diameters for the Cts/C-15A sample is better than those of Cts/C93A sample, and it has also been observed that *S. aureus* is more sensitive to Cts/C15A than *E. coli*. This may be attributed to the antimicrobial activity of the quaternary ammonium silicate layer of Ct/C-15A incorporated film. The effectiveness of such groups bearing alkyl substituents in disrupting bacterial cell membranes (especially for *S. aureus*) and causing cell lysis has been well documented in the literature [25–28]. In the case of Cts/C93A, greater activity was noted against *E. coli* than *S. aeureus*. There are some suggestions that the antimicrobial activity of polymer clay nano composites depends on super molecular organization of the surfactants and the nanostructure of the components. Cts/C-93A has most activity against *E. coli* despite having the lowest surfactant content in the organoclay, that is, 90 % of the surfactants with respect to CEC(Cationic exchange capacity) whereas Cts/C-15A has highest surfactant content in the organo clay and has highest activity against *S. Aureus* (Fig. 7).

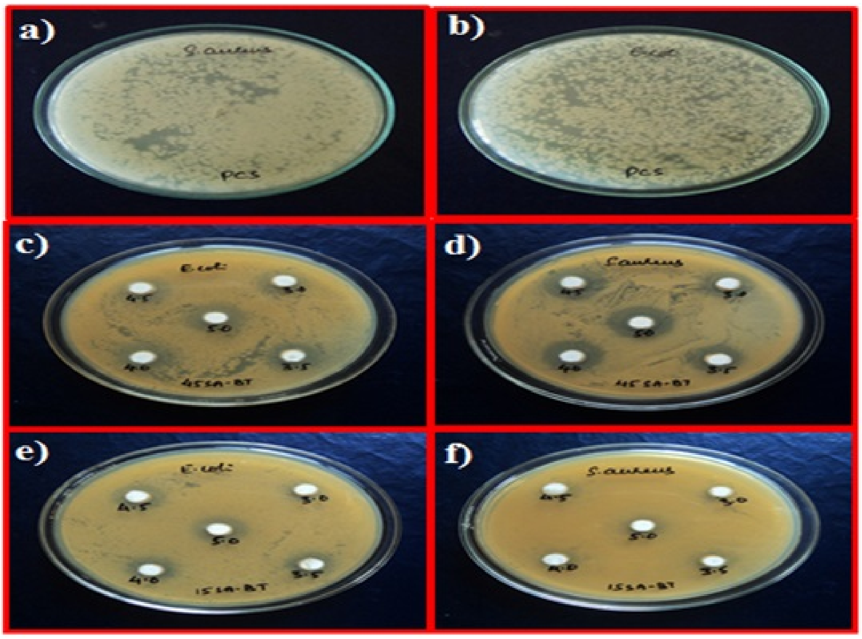

FIG. 7. Antimicrobial activity of a) pure Ct for E coli., b) Pure Ct for S aureus, c) Ct/C-93A for E coli, d) Ct/C-93A S aureus, e) Ct/C-15A for E coli, f) Ct/C-15A for S aureus

5. Conclusion

The effect of different organo-modified nanoclays on the properties of chitosan (Cts) based bio-nanocomposites (BNCs) was evaluated. The exfoliated structure was observed in XRD results. These results were corroborated by SEM results. The homogenous dispersion of nanoparticles and homogenous matrix in SEM images provided evidence for the BNC's exfoliated structure. The addition of nanoclays produces a thermal barrier and decreases the weight loss, thus inorganic particles are found to enhance the thermal stability of the chitosan composites. The increase in chitosan content in the film increased the swelling capacity significantly; the decreasing order swelling capacity of Cts/Clay films was due to the presence of more hydrophilic groups in the film network, which assist in improving the swelling characteristics of the films. The chitosan with different organo-modified clays exhibited optimum antibacterial activity against *E. coli.* and *S. aureus*.The inhibition diameters of these complexes were slightly smaller and the amount of antibiotic explains the smaller inhibition halos that the adsorption complexes showed in comparison to those of the antibiotic solutions.

References

[1] Ray S.S., Okamoto M. Polymer/layered silicate nanocomposites: a review from Preparation to processing. *Prog in Polym Sci.*, 2003, **28**, P. 1539–1641.

[2] Pavlidou S., Papaspyrides C.D. A review on polymer-layered silicate nanocomposites, *Prog in PolyM Sci.*, 2008, **33**, P. 1119–1198.

[3] Wilson B., Samanta M.K., Santhi K., Sampath Kumar K.P., Ramasamy M. Suresh Chitosan nanoparticles as a new delivery system for the anti-Alzheimer drug tacrine. *Nanomedicine: Nanotechnology, Biology, and Medicine*, 2010, **6**, P. 144–152.

[4] Dev A., Binulal N.S., Anitha A., Nair S.V., Furuike T., Tamura H., Jayakumar R. Preparation of poly (lactic acid)/chitosan nanoparticles for anti-HIV drug delivery applications. *Carbo Poly.*, 2010, **80**, P. 833–838.

[5] Wang X., Du Y., Luo J., Lin B., Kennedy J.F. Chitosan/organic rectorite nanocomposite films: structure, characteristic and drug delivery behavior. *Carbohydrate Polymers*. 2007, **69**, P. 41–49.

[6] Depan D., Pratheep Kumar A., Singh R.P. Cell proliferation and controlled drug release studies of Nano hybrids based on chitosan-g-lactic acid and montmorillonite. *Acta Biomater.*, 2009, **5**, P. 93–100.

[7] Wang X., Du Y., Yang J., Wang X., Shi X., Hu Y. Preparation, characterization and antimicrobial activity of chitosan/layered silicate nanocomposites. *Polymer.*, 2006, **47**, P. 6738–6744.

[8] Mizushima Y., Ikoma T., Tanaka J., Hoshi K., Ishihara T., Ogawa Y., Ueno A. Injectable porous hydroxyapatite micro particles as a new carrier for protein and lipophilic drugs. *J Cont Rele.*, 2006, **110**, P. 260–265.

[9] Xu Q.G., Czernuszka J.T. Controlled release of amoxicillin from hydroxyapatite-coatedpoly (lactic-co-glycolic acid) microspheres. *J Control Release*, 2008, **127**(2), P. 146–153.

[10] Real R.P., Padilla S., Vallet-Regí M. Gentamicin release from hydroxyapatite/poly (ethyl Methacrylate) composites. *J. Biomed Mater Res.*, 2000, **52**, P. 1–7.

[11] Han Y.S., Lee S.H., Choi K.H., Park I. Preparation and characterization of chitosan-claynanocomposites with antimicrobial activity. *Jour of Phys and Chem of Solids.*, 2010, **71**, P. 464–467.

[12] Katti K.S., Turlapati P., Verma D., Gujjula P.K., Katti D.R. Static and dynamic mechanical behavior of hydroxyapatite-polyacrylic acid composites under simulated body fluid. *Ameri Jour Biochem Biotechno*, 2006, **2**, P. 73–79.

[13] Ebru Günister, Dilay Pestreli, Cüneyt H. Ünlü, Oya Atıcı, Nurfer Güngör. Synthesis and characterization of chitosan-MMT biocomposite systems. *Carbohydrate Polymers*, 2007, **67**(3), P. 358–365.

[14] Alexandre M., Dubois P. Polymer-layered silicate nanocomposites: Preparation, properties and uses of a new class of materials. *Materials Science and Engineering*, 2008, **R28**, P. 1–63.

[15] Margarita Darder, Montserrat Colilla. Eduardo Ruiz-Hitzky Chitosan-clay Nano composites: application as electrochemical sensors. *Applied Clay Science*, 2005, **28**, P. 199–208.

[16] Wang S.F., Shen L., Tong Y.J., Chen L., Phang I.Y., Lim P.Q., Liu T.X. *Polymer Degradation and Stability*, 2005, **90**, P. 123–131.

[17] Sadok Letaïef, Pilar Aranda, Eduardo Ruiz-Hitzky. Influence of iron in the formation of polypyrrole-clay nanocomposites. *Applied Clay Science*, 2005, **28**(1-4), P. 183–198.

[18] Xiaoying Wang, Yumin Du, Jianhong Yang, Xiaohui Wang, and Xiaowen Shi, Ying Hu. *Polymer*, 2006, **47**, P. 6738–6744.

[19] Rhim J., Hong S., Park H., Perry K.W. Preparation and characterization of chitosan-based nanocomposite films with antimicrobial activity. *Journal of Agricultural and Food Chemistry*, 2006, **54**, P. 5814–5822.

[20] Fan J., Hanson B. *Inorg. Chem.*, 2005, **44**, P. 6998–7008.

[21] Fan J., Slebodnick C., Angel R., Hanson B.E. *Inorg. Chem.*, 2005, **44**, P. 552–558.

[22] Ojagh S.M., Rezaei M., Razavi S.H., Hosseini S.M. Effect of chitosan coatings enriched with cinnamon oil on the quality of refrigerated rainbow trout. *Food Chemistry*, 2010, **120**, P. 193–198.

[23] Zivanovic S., et al. Antimicrobial Activity of Chitosan Films Enriched with Essential Oils. *Journal of Food Science*, 2005, **70**(1).

[24] Choma C., Clavel T., Dominguez H., Razafindramboa N., Soumille H., Nguyen-the C., Schmitt P. Effect of temperature on growth characteristics of Bacillus cereus TZ415. *International Journal of Food Microbiology*, 2000, **55**, P. 73–77.

[25] Hugo W.B., Russel A.D. Types of antimicrobial agents. In Principles and Practice of Disinfection. Preservation and Sterilization; Russel A.D., Hugo W.B., Ayliffe G.A.J., Eds. Blackwell Scientific Publications: Oxford, U.K, 1992, P. 7–68.

[26] Kim C.H., Choi J.W., Chun H.J., Choi K.S. Synthesis of chitosan derivatives with quaternary ammonium salt and their antibacterial activity. *Polym. Bull*, 1997, **38**, P. 387–393.

[27] Gottenbos B., Van der Mei H.C., Klatter F., Nieuwenhuis P., Busscher H.J. In vitro and in vivo antimicrobial activity of covalently coupled quaternary ammonium silane coatings on silicone rubber. *Biomaterials*, 2002, **23**, P. 1417–1423.

[28] Kim J.Y., Lee J.K., Lee T.S., Park W.H. Synthesis of chitosan oligosaccharide derivative with quaternary ammonium group and its antimicrobial activity against Streptococcus mutans. *Int. J. Biol. Macromol.*, 2003, **32**, P. 23–27.

NANOSYSTEMS: PHYSICS, CHEMISTRY, MATHEMATICS, 2016, 7 (4), P. 675–677

Superparamagnetism in FeCo nanoparticles

P. P. Pradyumnan

Department of Physics, University of Calicut, Kerala 673 635, India

drpradyumnan@gmail.com

PACS 75.75.+a, 81.16 Be **DOI 10.17586/2220-8054-2016-7-4-675-677**

Superparamagnetism is an important physical property of a certain kinds of nanoparticles and these particles have attracted interest because of their applications in the technological world and medical fields. In this work, the author reports the synthesis of iron cobalt ($Fe_{60}Co_{40}$) and Manganese (Mn) incorporated FeCo compound nanoparticles by a simple inert atmosphere reductive decomposition method. The synthesized nanoparticles were characterized by transmission electron microscopy (TEM), X-ray diffraction technique (XRD), selected area electron diffraction (SAED), energy dispersive X-ray analysis (EDX) and Fourier transform infrared (FTIR) spectroscopic method. The magnetic properties of the particles have been studied with a magnetometer (SQUID).

Keywords: Nanoparticle, soft magnetic, $Fe_{1-x}Co_x$ compound, reductive decomposition, TEM, SQUID.

Received: 5 February 2016

Revised: 24 April 2016

1. Introduction

Nanoparticles have now turned from theoretical interest to application in the technological world. In these years nanomagnetic particles have drawn special attention because of their recording ability and use as perpendicular magnetic memory and biomedical applications such as hyperthermia, magnetic resonance contrast enhancement and drug delivery etc. [1]. The nanoparticles, which show high magnetic moment are a better candidate, as far as the applications are concerned. The FeCo nano particle has such ability, but the main task is its preparation and stability. Many investigators have prepared nanoparticles of FeCo compounds using different techniques.

They have used chemical and physical methods for the growth of nanoparticles. Most of the physical methods require substrates [2–6]. For the fabrication of perpendicular recording media, substrate is applicable, but for the biological application individual nanoparticles are more reliable.

This paper reports the preparation of multifunctional nanoparticles of $Fe_{1-x}Co_x$ and Mn-incorporated compounds by a reductive decomposition-based reflux method using suitable stabilizers and surfactants. We have prepared three compositional compounds containing iron and cobalt as well iron, cobalt and manganese. All these synthesized materials were characterized by X-ray diffraction (XRD), selective area electron diffraction (SAED), Fourier transform infrared spectroscopy (FTIR), energy dispersive X-ray (EDX) and transmission electron microscopy (TEM). The magnetic properties of the materials studied using SQUID magnetometer.

2. Synthesis

The $Fe_{1-x}Co_x$ compounds, Mn incorporated nanoparticles were prepared using a modified method reported by Sun et al. [2]. Here, we used $Fe(acac)_3$ and $Co(acac)_2$, $Mn(acac)_2$ as precursors. Reductive decomposition of these was achieved by using benzyl ether as solvent medium, 1-octadecene as reducing agent and oleic acid as surfactant and oleylamine as stabilizer. The growth temperature was fixed at 240 °C. To avoid oxidation during nanoparticle growth, the reaction chamber was blanketed with argon. Care has been taken for the collection of the nanoparticles and washing of the nanoparticles to avoid the surfactants and stabilizers. But it was found to be very difficult to completely rinse the surfactants and stabilizers from the nanoparticles.

The shape of the nanoparticles depended on the growth temperature, whereas it had nothing to do with the composition and size of the particles. But it is very difficult to control the size of all the particles in this case. In our studies, we have fixed the above temperature for obtaining the maximum product. In all the compositions, the particle size found was to be less than 10 nm.

3. Experiments

3.1. X-ray diffraction (XRD)

XRD is the most primary technique to analyze the crystalline nature of the material. A Rigaku X-ray diffractometer has been utilized for the studies. All the three compounds shows the crystal structure is body centered cubic (bcc). Since the particle size is too small, the spectral broadening is evident. The peaks at (110) and (200) peaks are visible. TEM-electron diffraction studies were also utilized to confirm the crystalline nature of the compounds.

3.2. Infrared Spectroscopy

During the preparation of the compounds, organic chemicals like oleic acid and oleylamine were utilized. Even though proper washing has been done for the particles, there is a finite possibility that these molecules can be found on the surface of the nanoparticles. The IR spectrum of all the particles shows, the absorption bands. It is very difficult to wash out all the surfactants, and there is a strong attachment between the compound particles and these molecules. Fig. 1 shows the IR spectrum for one sample of the compounds.

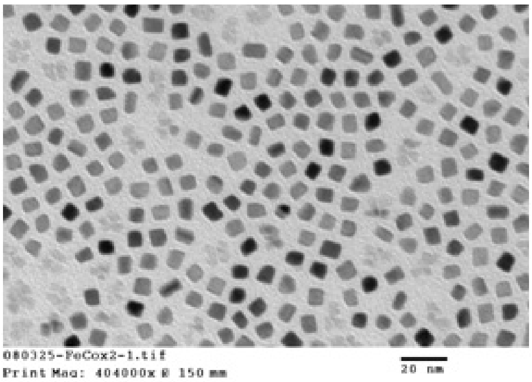

FIG. 1. TEM image of FeCo nano particles

For oleic acid, whose formula is ($CH_3(CH_2)_7CH = CH(CH_2)_7COOH$), the following pattern was observed: the vibration is assigned at C–C (either COOH- or CH_3-sided) stretching. The difference observed is probably due to C=C bonding. In the spectrum of the broad, strong band at 1161 cm^{-1} flanked by weaker bands at 1238 and 1118 cm^{-1}.

3.3. Energy Dispersive X-ray Analysis (EDX)

The percentages of the Fe and Co present in all the prepared compound nanoparticles were measured using EDX technique. During synthesis we have approximated the ratio by varying the molar ratio of the precursors. Table 1, gives the ration of the final compositions of the $Fe_{1-x}Co_x$ compounds. From these results, we observed that the Fe ion is dominant in the compound formation and the single phases will be observed during these ratios only.

TABLE 1. Ration of the expected and actual compositions for $Fe_{1-x}Co_x$ compounds

No of compound combinations	Molar ratio of the metal precursors used		Molar ratio of the metal actually present in the compounds as per EDX	
	Fe	Co	Fe	Co
1	0.60	0.40	0.65	0.35
2	0.50	0.50	0.60	0.40
3	0.40	0.60	0.55	0.45

3.4. Transmission Electron Microscopic Studies (TEM)

The TEM images of the prepared nano particles are shown in Fig. 1. The $Fe_{1-x}Co_x$ compounds ($x = 0.35$, 0.40, 0.45).

The coercivity was found to be 0. Fig. 2 shows the room temperature hysteresis loops of the $Fe_{60}Co_{40}$ compound nanoparticles. We took same weight (0.1 mg) of both compound particles for SQUID studies It is found that due to the incorporation of Mn, the magnetic behavior of the materials were drastically changed and the magnetic moment was reduced, due to the incorporation of Mn ions. Fig. 2 shows the M/Ms Vs H graph of synthesized materials.

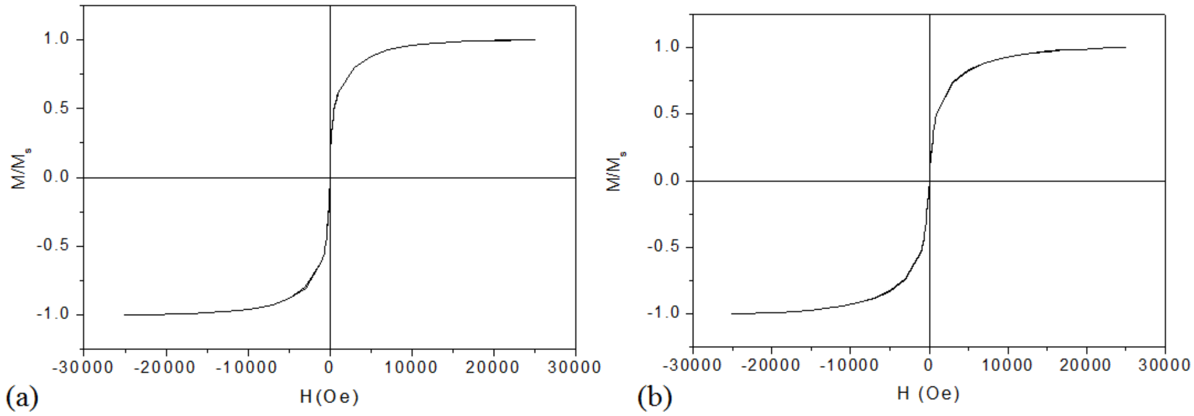

FIG. 2. Hysteresis loop of (a) $Fe_{60}Co_{40}$ and (b) $Fe_{65}Co_{30}Mn_5$ compound nanoparticle (size: 4 – 5 nm)

4. Conclusion

Well defined nanoparticles of FeCo and Mn incorporated FeCo compound were synthesized by a reductive decomposition-based reflux method. Uniformly sized nanoparticles of size 4 – 5 nm have been well characterized. The magnetic properties were attenuated due to the incorporation of Mn ion. Both the compound particles showed super paramagnetic behavior at room temperature.

Acknowledgements

Author grateful to SERB, Govt. of India for major research project funding SB/EMEQ-002/2013 and DST-FIST, Department of Physics, University of Calicut for experimental facilities.

References

[1] Reiss G., Hutten A. Magnetic nanoparticles-applications beyond data storage. *Nature materials*, 2005, **4** (10), P. 725–726.

[2] Don Keun Lee, Young Hwan Kim, et al. Preparation of monodisperse Co and Fe nanoparticle using precursor of M^{2+}-oleate$_2$ (M = Co, Fe). *Curr. Appl. Phys.*, 2006, **6**, P. 786–790.

[3] Soo Ja Shin, Young Hwan Kim, et al. Preparation of magnetic FeCo nanoparticles by coprecipitation route. *Curr. Appl. Phys.*, 2007, **7**, P. 404–408.

[4] Yun Hao Xu, Jianmin Bai, Jian-Ping Wang. High-magnetic-moment multifunctional nanoparticles for nanomedicine applications. *J. Magn. Magn. Mater.*, 2007, **311**, P. 131–134.

[5] Wen J.Z., Goldsmith F.C., et al. Detailed Kinetic Modeling of Iron Nanoparticle Synthesis from the Decomposition of $Fe(CO)_5$. *J. Phys. Chem. C*, 2007, **111**, P. 5677–5688.

[6] Shousheng Sun, Murrey C.B., et al. Monodisperse FePt Nanoparticles and Ferromagnetic FePt Nanocrystal Superlattices. *Science*, 2000, **289**, P. 1989–1992.